THE UNIVERSITY OF CALGARY

Are P- and S-wave velocities and attenuations related to permeability?: Ultrasonic seismic data for sandstone samples from the Writing-on-Stone Provincial Park in Alberta

by

Nicolas Williams Martin

A THESIS

SUBMITTED TO THE FACULTY OF GRADUATE STUDIES

IN PARTIAL FULFILMENT OF THE REQUIREMENTS FOR THE

DEGREE OF MASTER OF SCIENCE

DEPARTMENT OF GEOLOGY AND GEOPHYSICS

CALGARY, ALBERTA

DECEMBER, 1996

THE UNIVERSITY OF CALGARY

FACULTY OF GRADUATE STUDIES

The undersigned certify that they have read, and recommend to the Faculty of Graduate Studies for acceptance, a thesis entitled "Are P- and S-wave velocities and attenuations related to permeability?: Ultrasonic seismic data for sandstone samples from the Writing-on-Stone Provincial Park in Alberta" submitted by Nicolas Williams Martin in partial fulfilment of the requirements for the degree of Master of Science.

Supervisor, Dr. J.R. Brown
Department of Geology and Geophysics

Dr. G. Margrave
Department of Geology and Geophysics

Dr. F.F. Krause
Department of Geology and Geophysics

Dr. G. Milone
Department of Physics and Astronomy

December 19, 1996
Date

ABSTRACT

Some experimental results measuring P- and S-wave phase velocities and attenuation coefficients in the laboratory, under dry and water-saturated conditions at a ultrasonic frequency of 1.0 Mhz and atmospheric pressure on sandstone samples of the Milk River Formation in the Writing-on-Stone Provincial Park (WOSPP), southern Alberta, are presented and correlated with limited petrophysical data, as clay content, porosity and permeability, obtained from these sandstone samples.

The principal objective of this study is to estimate how the petrophysical properties such as clay content, porosity and permeability, affect the observed behavior of P- and S-wave phase velocities and attenuation coefficients on sandstone samples from WOSPP. Additionally, from this analysis I hope to determine whether, velocity or attenuation is more important for predicting permeability and permeability anisotropy from ultrasonic data.

These sandstone samples present an anisotropic velocity behavior like a transverse isotropy (TI) after analyzing its measured P-wave phase velocities under dry conditions, along three orthogonal axis oriented parallel and perpendicular to the layering in these samples.

In addition, these sandstone samples present different degree of permeability anisotropy, with the axis perpendicular to the layering having lower permeability than permeability measured along two axes parallel to the layering.

An analysis of the effect of polarization direction for S waves on phase velocity and attenuation is included, showing that for these sandstone samples the estimated S-wave phase velocities and attenuations are not significantly affected by the polarization direction. Also, the effect of the internal pressure on P-wave phase velocity and attenuation for a sandstone sample is analyzed. The experimental result shows a total agreement with experimental results obtained by other authors.

The most important conclusion obtained from this study is that the attenuation coefficient for P and S waves is more affected by permeability than phase velocity. For the

same permeability range the variation of the P- and S-wave attenuation coefficient is higher than the corresponding variation in phase velocity for both waves. For P waves the phase velocity tends to show no dependence on permeability above some critical permeability, but S-wave phase velocity tends to increase when permeability is increased beyond this critical permeability.

ACKNOWLEDGMENTS

FOOTPRINTS

One night a man had a dream. He dreamed he was walking along the beach with the Lord. Across the sky flashed scenes from his life. For each scene, he noticed two sets of footprints in the sand: one, belonging to him, and the other to the Lord.
When the last scene of his life flashed before him, he looked back at the footprints in the sand.
He noticed that many times along the path of his life there was only one set of footprints. He also noticed that it happened at the very lowest and saddest times in his life.
This really bothered him and he questioned the Lord about it.
"Lord, You said that once I decided to follow You, You'd walk with me all the way. But I have noticed that during the most troublesome times in my life, there is only one set of footprints. I don't understand why when I needed You most You would leave me".
The Lord replied, "My son, My precious child, I love you and would never leave you. During your times of trial and suffering, when you see only one set of footprints, it was then that I carried you".

-Author Unknown

Thanks the Lord, Maria Donati, Maggiorina de Donati, Beatriz Borges, James Brown, Federico Krause and family, Rudy Meyer, Eric Gallant, Henry Bland, Darren Foltinek, Robert Stewart, Don Lawton, Gary Margrave, John Bancroft and family, Louise Forgues, Regina Shedd, Gail Campbell, Faye Nichollson, Sharron Kaser, Marvel Nash, The Department of Geology and Geophysics , The CREWES Project, Sponsors of The CREWES Project, Intevep, S. A., Lagoven, S. A., Core Laboratories, Gene Milone, Ricardo Perez and family, and my friends at The University of Calgary, for have given me the opportunity to look back at my footprints in the sand and notice that many times there was only one set of footprints during my life in Canada. Thanks for carrying me during my lowest and saddest times !!!!

TABLE OF CONTENTS

LIST OF TABLES

List of Figures

CHAPTER 1
Introduction

1.1 Presentation of the problem

For most of this century, oilfield theory and practice considered that rocks exhibits isotropic wave velocities, that is, the measured velocities are no direction-dependent. However it is known that seismic waves travel through some rocks with different velocities in different directions due to a spatial ordering of crystals, grains, cracks, bedding planes, joints or fractures — essentially an alignment of strengths or weaknesses — on a scale smaller than the length of the wave. This phenomenon is called elastic anisotropy and is represented by the anisotropic elastic stiffness tensor (Anderson *et al.*, 1974; Crampin 1978; 1981; 1984a,b; Crampin *et al.*, 1984; Sheriff, 1984)

If there exists any elastic anisotropy caused by horizontal fine layering or fractures, it implies that, in addition to an anisotropic elastic stiffness tensor, the material will show an additional dynamic effect due to anisotropic permeability (Gelinsky and Shapiro, 1994a, b; 1995). For materials showing transverse isotropy, due to the presence of horizontal fine layering, the permeability — the ease with which fluids flow through rock — measured parallel to the layers of porous sedimentary rocks can be greater than the permeability measured vertically ($k_h > k_v$). On the other hand, for rocks that are azimuthally anisotropic due to parallel fracture planes, the permeability measured perpendicular to the fracture planes is smaller than the permeability of the rock measured parallel to the fractures ($k_h < k_v$). Both cases of anisotropic permeability are shown in Figure 1.1 (Gelinsky and Shapiro, 1994a, b; 1995).

Permeability anisotropy can affect the injection and production rates during any completion and treatment strategies, *e.g.*, the drainage pattern for an ideal horizontal well is ellipsoidal and dominated by permeability anisotropy where its semi-axes are related to the length of the horizontal section, the horizontal permeability, and the vertical permeability as shown in Figure 1.2 (Ayan *et al.*, 1994). Additionally, mapping permeability variation along the well enables optimization of completion design, such as

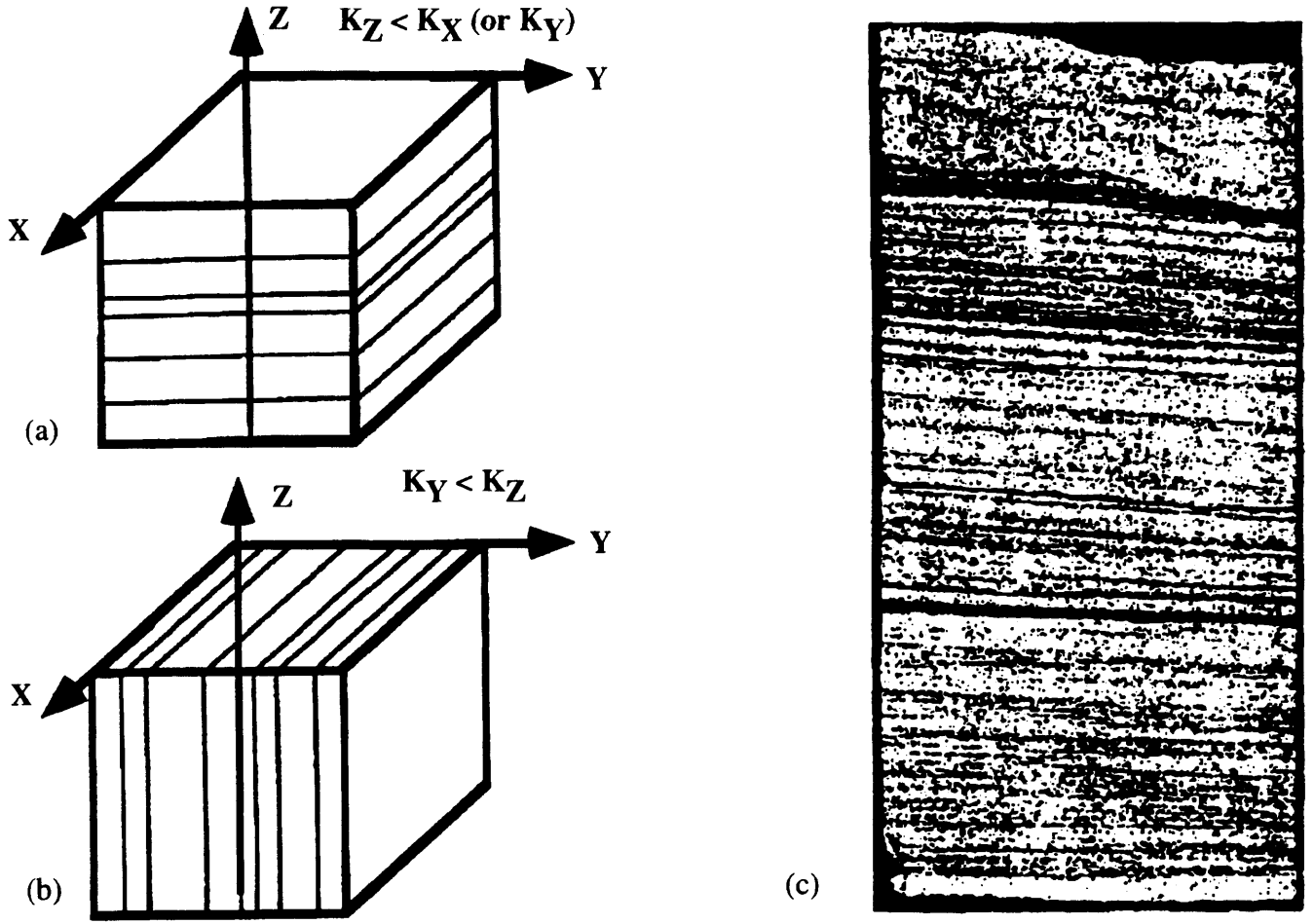

Fig. 1.1 Generalized kinds of permeability anisotropy. (a) Transverse isotropy. (b) Azimuthal anisotropy. (c) Permeability anisotropy in a sandstone. Thin layers of shale and quartz overgrowth block most of the vertical flow, making horizontal permeability much higher than the vertical permeability [(a) and (b) after Gelinsky and Shapiro, 1994; (c) after Ayan *et al.*, 1994]

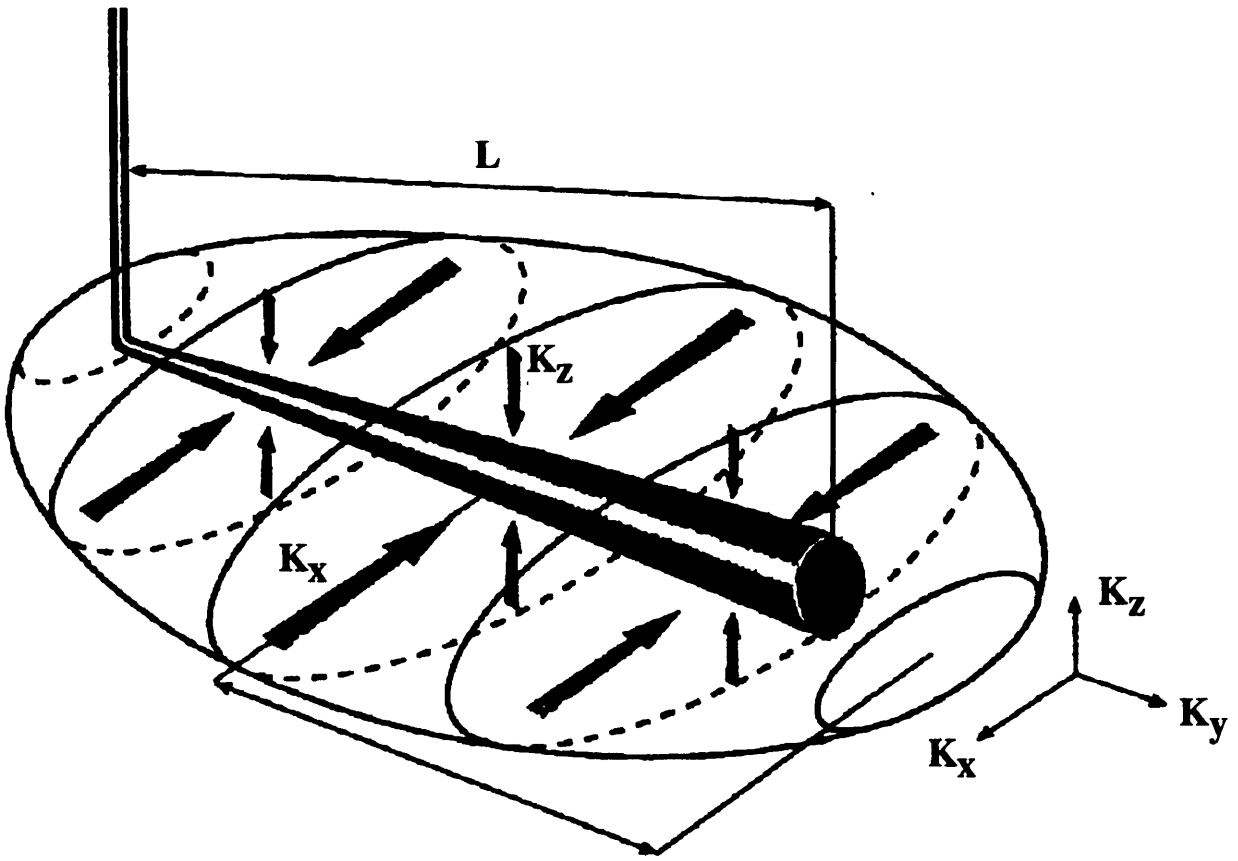

Fig. 1.2 Horizontal-well drainage pattern. The drainage pattern forms an ellipsoid whose semi-axes depend on the length of the horizontal section (L) and horizontal (K_Y) and vertical (K_Z) permeabilities (after Ehlig-Economides *et al.*, 1990).

deciding where to place isolation packers or which sections of a cased hole to perforate (Ehlig-Economides *et al.*, 1990; Ayan *et al.*, 1994).

Several approachs, principally at ultrasonic frequencies in laboratory, have been used for estimating permeability anisotropy from other rock measured properties. Gibson and Toksöz (1990) predicted how the permeability would vary with direction in fractured rocks based on seismic velocity anisotropy. But, the ultrasonic experimental data of Han (1987) and Klimentos and McCann (1990) acquired on sandstone samples show that the attenuation coefficient is more strongly related to clay content than velocity. Additionally, Klimentos and McCann (1990) show a strong systematic relationship between clay content and permeability and they conclude that the attenuation is the key factor in determining permeability from seismic data.

Gelinsky and Shapiro (1994a,b; 1995) presented a theoretical approach for modelling the wave propagation of P, SV and SH waves across a homogeneous, liquid-saturated porous medium having an isotropic poroelastic matrix and permeability anisotropy using Biot theory (Biot 1956a,b; 1962). They conclude that using this model the velocity anisotropy due to the anisotropic permeability is not significant but that the attenuation coeffficient is direction-dependent at seismic frequencies (0 - 100 Hz). For this frequency range the degree of attenuation anisotropy is equal to that of the permeability anisotropy; however, its absolute value is very small. For a frequency range between 10 - 200 kHz, the velocity anisotropy increases showing a maximum at 200 kHz whilst the attenuation anisotropy is reduced (it is totally isotropic at 200 kHz). On the other hand, at higher frequencies the degree of velocity anisotropy is again reduced and the attenuation coefficcient is again anisotropic (Figure 1.3).

These experimental and theoretical results show that it is feasible to obtain valuable information about the permeability anisotropy of the reservoir from the study of the behavior of the seismic attenuation coefficient with direction.

1.2 Thesis objective

The objective of this thesis is to study relationships among velocity, attenuation and permeability anisotropies (under dry and saturated conditions) for sandstone samples

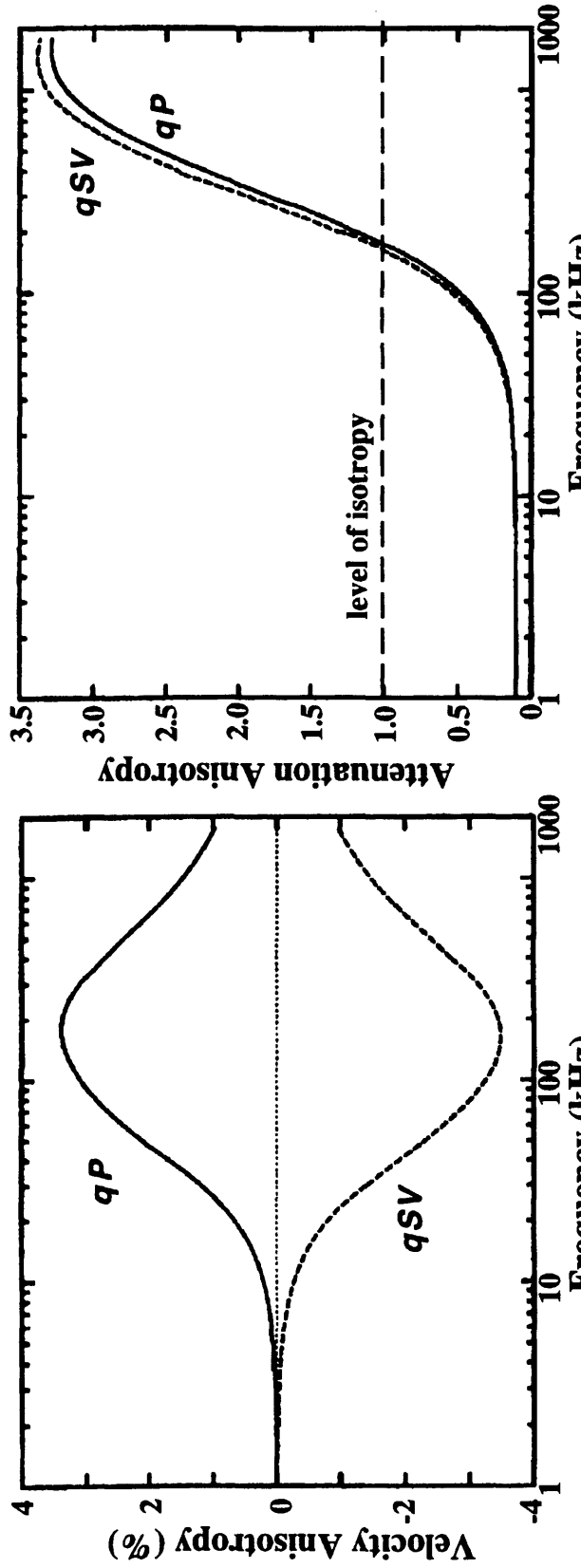

Fig. 1.3 (a) Velocity anisotropy as a function of frequency due to permeability anisotropy. Maximum velocity anisotropy is reached for a frequency near 200 kHz for both *qP* and *qSV*. (b) Attenuation anisotropy expressed as the ratio between attenuation coefficient (parallel to the symmetry axis) divided by its value measured perpendicular to this direction (after Gelinsky and Shapiro, 1995: Public document on the Internet).

at ultrasonic frequencies and separate these effects from those of other petrophysical properties. This will be done for both *P* and *S* waves using the transmission method across sandstone cores from the Milk River Formation in the area of Writing-on-Stone Provincial Park in south-central Alberta, near the Canada/USA border. These sandstone samples present different degrees of permeability anisotropy, relative low clay content, and a very limited lithologic variety. For S-waves the effect of the polarization direction on the measured phase velocities and attenuation coefficients for these kind of waves will be additionally considered.

Also, the effect of confining pressure on P-wave phase velocity and P-wave attenuation coefficient will be evaluated in order to properly simulate reservoir conditions.

1.3 Data set used and brief description of the experimental methodology

The present study will be performed on plug samples consisting of sandstones from the Milk River Formation in the Writing-on-Stone Provincial Park (Figure 1.4). The geologic framework, sedimentology and lithofacies information will be described extensively in Chapter 3. A total of 60 samples are considered and velocity and attenuation data are obtained from them using the ultrasonic transmission method at frequencies of about 1.0 MHz for P and S waves. Additionally, for *S* waves, some data have been acquired at two different orientations, 45° apart, with the goal of studying the effect of the polarization direction on S-wave velocity and S-wave attenuation. These plug samples have information about petrophysical parameters such as clay content, porosity and permeability, which normally affect both seismic velocity and attenuation. The clay content have been determined using the X-ray diffraction method. The sandstone samples were cleaned in methanol and dried in a vacuum oven at 85°C for a period of twenty-four hours. The permeability was measured using a helium permeameter at the University of Calgary. Both clay content and porosity measurements were performed by Core Laboratories in Calgary. The velocity and attenuation measurements on the sandstone samples have been performed under dry and water-saturated conditions at atmospheric confining pressure. The effect of higher confining pressures on both P-wave velocity and

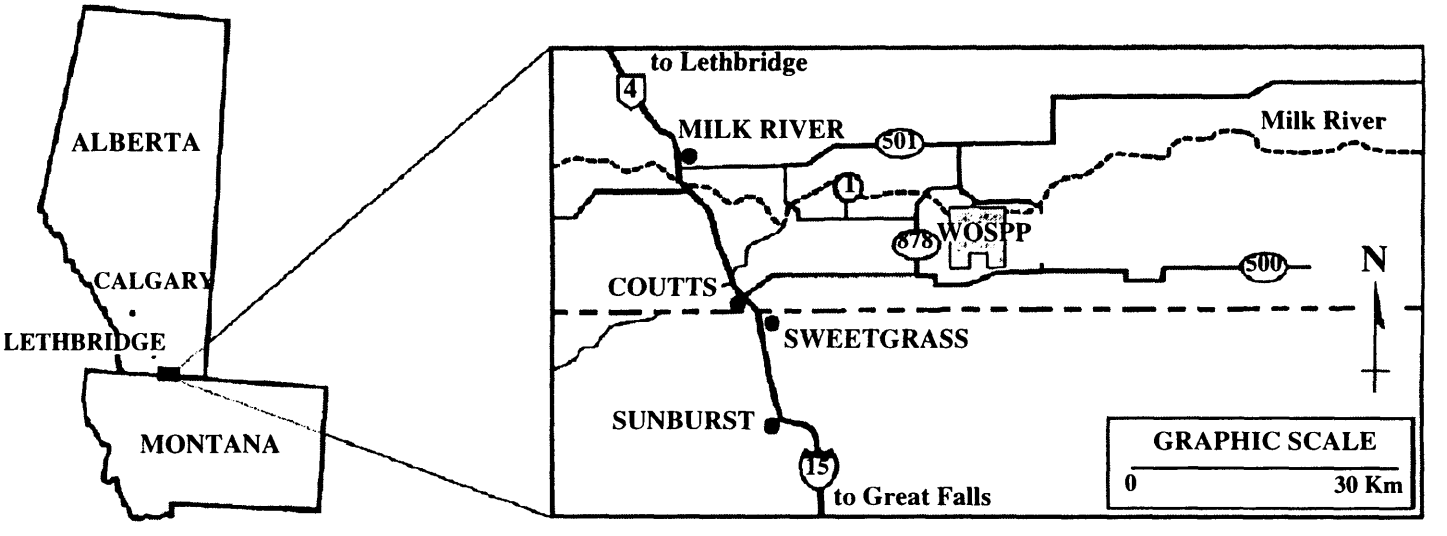

Fig 1.4 Access and location map of the study area in south-central Alberta, near the Canada/USA border. The area of Writing-on-Stone Provincial Park (WOSPP) is shown in grey (after Meyer, 1994).

attenuation is also considered. The confining pressure ranges are between 0 and 2700 psi with a constant internal pore pressure of 100 psi (Chapter 4).

A preliminary step in the experimental methodology consists in correcting the velocity and attenuation values for effects that mask the variables of interest. This involves geometric corrections to account for energy loss by beam spreading and diffraction corrections due to finite-size transducers. This is an important experimental step because the geometric effects mask the intrinsic or anelastic attenuation (the energy lost by conversion into heat due to interaction between the waves and the rocks) which gives additional information on the petrophysical properties of rocks such as permeability, degree of saturation, type of saturant, etc. The velocity after these corrections is assumed to be affected only by velocity dispersion associated with the media.

After performing these corrections, the phase velocity measurements on each sandstone sample are done by using the first-zero-crossover method (Figure 1.5). In this method, the time interval between the first zero crossovers of the transmitted and the received signals is measured. Then, the phase velocity is estimated by dividing the sample length by this time interval. This method gives a good estimate of the low-frequency phase velocity of the dominant frequency for a dispersive medium with frequency-dependent attenuation (Rathore *et al.*, 1993; 1994).

On the other hand, the attenuation coefficient, $a(w)$ (or equivalently the quality factor, Q) is determined using the spectral ratio method proposed by Toksöz *et al.* (1979) and Johnston and Toksöz (1980). This method assumes that the attenuation coefficient is a linear function of frequency. If this is the case, then a graph of of the logarithmic ratio of the spectra amplitudes recorded through a reference sample of aluminum (assumed to have a negligible attenuation coefficient) and a sandstone sample *versus* frequency, gives a direct estimation of the attenuation coefficient through the estimate of the slope of this curve (Figure 1.6).

Chapter 2 deals with the basic theoretical background concerning the permeability-porosity, permeability-velocity and permeability-attenuation relationships obtained from theoretical developments and ultrasonic experimental data, which will help in the interpretation of the results of this thesis (Chapter 5).

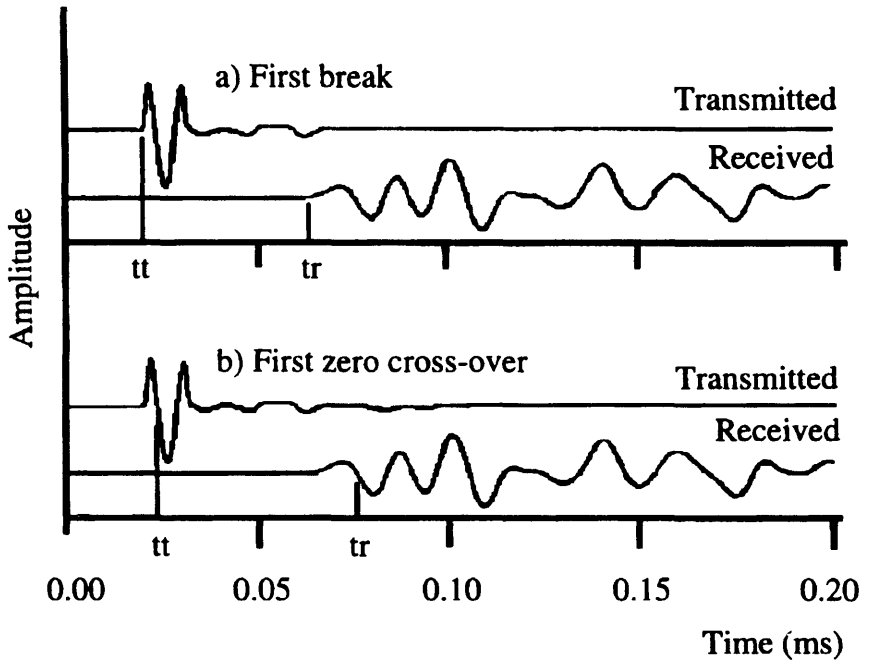

Fig. 1.5 Methods of wave velocity determination: (a) first-break method; (b) first-zero-crossover method. In both cases the velocity is calculated as $v_o=L_s/(t_r-t_t)$, where L_s is the sample length, and subscripts t and r are used for defining transmitted and received signals (after Rathore *et al.*, 1994).

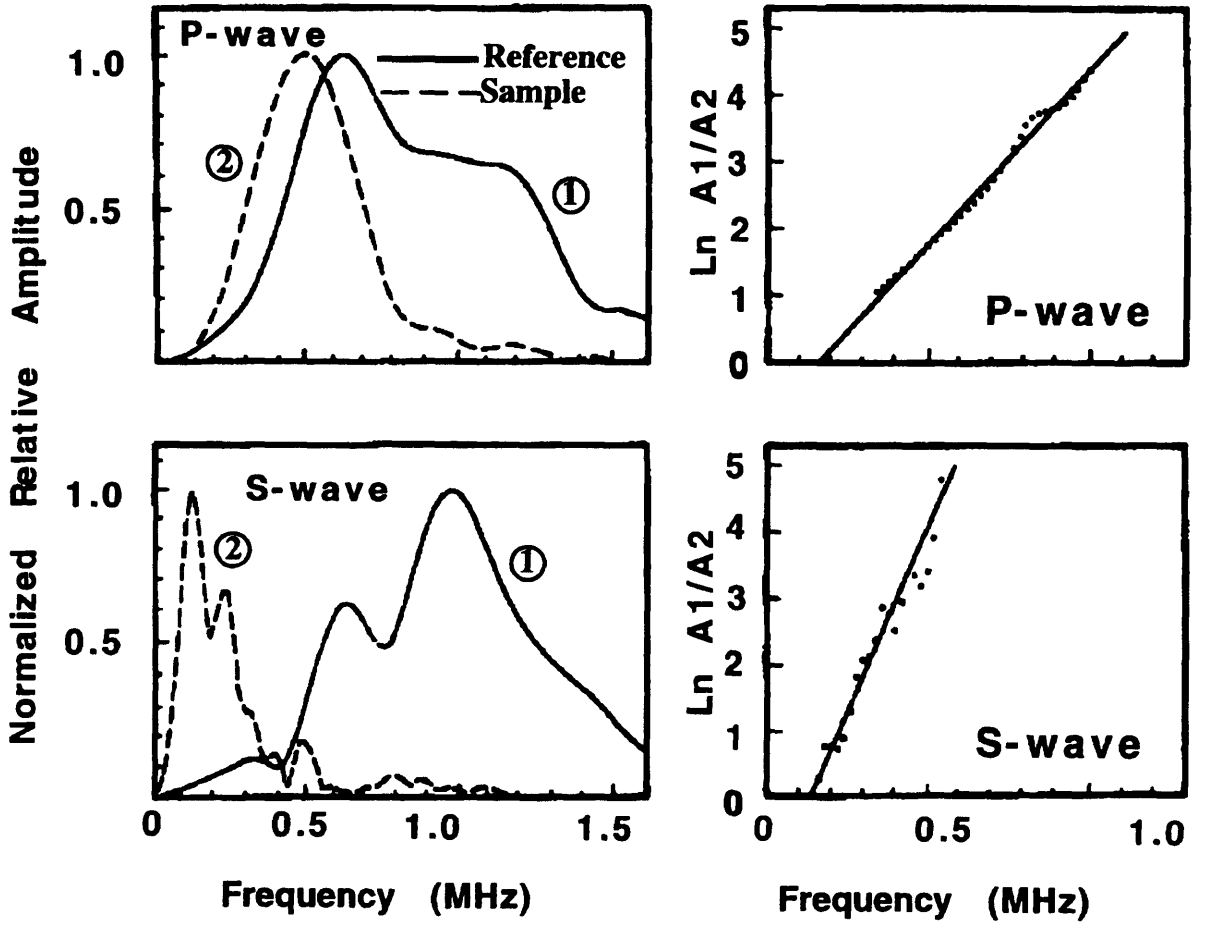

Fig. 1.6 Method used for estimating the attenuation coefficient in the laboratory. Here the numbers 1 and 2 stand for reference and sandstone samples, respectively (after Toksöz *et al.*, 1979).

1.4 Hardware and software used

Sandstone velocity and attenuation measurements at atmospheric pressure under dry and water-saturated conditions were performed using the CREWES Project acoustic modelling system at The University of Calgary, Canada. Panametrics V103 piezoelectric transducers were used for both *P*-wave sources and receivers. Panametrics V153 piezoelectric transducers were used for both S-wave sources and receivers. Amplified modeling data were recorded using a Nicolet oscilloscope connected, through an IBM-XT, which controls the experiment, to a Perkin-Elmer 3240 seismic processing system for storage. It was designed by the CREWES Project modeling laboratory and the department of Engineer in the University of Calgary, one sample device able to control pore and confining pressures at the same time, for measuring P- and S-wave phase velocities and attenuations under pressure. Equal hydrostatic confining pressure is applied to the jacketed sample by a hydraulic pump with pressure meters for adjusting continuously both pressures. Confining pressure can range from 200 psi to 2700 psi. The pressure unit has two ULTRAN transducers acting as source and receiver (P-P and S-S) and placed in contact with the jacketed sample at top and bottom. Both transducers (*P-P* and *S-S*) are connected to a Nicolet oscilloscope connected, through an IBM-XT, which controls the experiment, to a Perkin-Elmer 3240 seismic processing system for storage. One calibration measurement for *P*- and *S*-wave velocity under pressure on a representative sample was done by Core Laboratories in Calgary.

Clay content, porosity and permeability measurements on the sandstone samples were previously done by Core Laboratories and by Mr. Rudy Meyer as part of his Ph.D. thesis, for defining a 3-D geologic reservoir model of the Milk River Formation at Writing-on-Stone Provincial Park, Alberta (Canada).

Programing was undertaken mostly on a SUN workstation under a UNIX operating system. Experimental data were converted to SEGY IBM format and analysed using Promax software.

CHAPTER 2

Theoretical Background on Seismic Attenuation, Velocity and Permeability Anisotropy and their relationships

2.1 Attenuation and its consequences

2.1.1 Decay of amplitude spectrum

Frequently, when a propagating wave is introduced into the Earth from a source on the surface, it is recorded with some changes after its travel through the subsurface. The most evident of these changes is a loss or attenuation of the higher frequencies that characterized the spectrum of the waveform when it was generated by the source. In other words, the Earth introduces a reduction in the amplitude level and a change in the nature of the wavelet, which becomes broader and more asymmetric with increasing length of travel (Figure 2.1).

The attenuation phenomenon is different from other processes which make amplitude decay, such as geometrical spreading, reflection/transmission losses and diffraction. It is an intrinsic property of real materials related to internal friction or anelasticity (as opposed to perfect elasticity where waveforms travel indefinitely without changing shape because all frequencies are retained equally).

A better description of the seismic attenuation can be obtained by considering a waveform as a superposition of plane harmonic waves defined at a time t as a function of x, the distance traveled as follows:

$$u(x,t) = \frac{1}{2\pi} \int_{-\infty}^{\infty} S(\omega) \mathrm{e}^{-i\omega(t-x/v)} d\omega \qquad (2.1)$$

where $S(\omega)$ is the amplitude spectrum of the plane wave, x is the distance traveled by it from the source located at the origin, v is the velocity of phase, ω is the angular frequency ($= 2\pi f$) and $u(x,t)$ represents the waveform (Krebes and Hron, 1981; Cerveny and Frangie, 1982). Now, it is assumed that each Fourier (harmonic) component suffers attenuation.

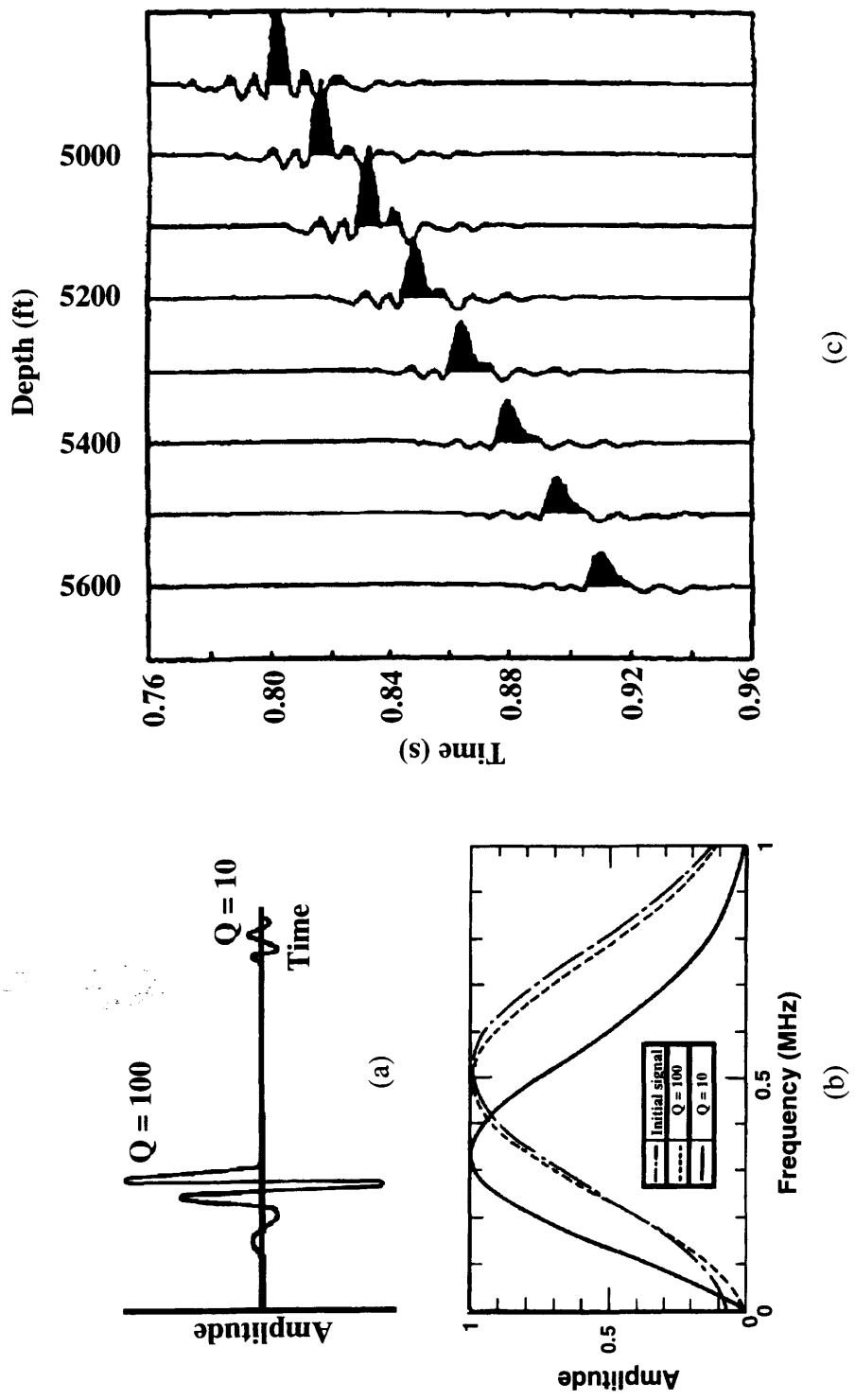

Fig. 2.1 Effect of the attenuation on the traveling signal. (a) Schematic example of a broad-band signal before and after propagation in an attenuating medium (high Q values indicate low attenuation). (b) Corresponding spectra indicating high-frequency loss. (c) Example of VSP traces from 4900 to 5600 ft showing decay in peak amplitude and asymmetry of the attenuated impulse (after Stainsby and Worthington, 1985).

This can be accounted for by introducing an attenuation coefficient, $a = a(\omega)$, which depends on frequency ω in some fashion and is a positive function (Toksöz *et al.*, 1979; Sears and Bonner, 1981; among others). Then,

$$u(x,t) = \frac{1}{2\pi}\int_{-\infty}^{\infty} S(\omega) e^{-a(\omega)x} \mathrm{e}^{-i\omega(t-x/v)} d\omega \tag{2.2}$$

or equivalently,

$$u(x,t) = \frac{1}{2\pi}\int_{-\infty}^{\infty} S(\omega) \mathrm{e}^{i(kx-\omega t)} d\omega \tag{2.3}$$

where k represents the complex wavenumber defined as $k = \omega/v + ia(\omega)$, for an anelastic medium (Borcherdt, 1973). Commonly, the attenuation is measured using the quality factor $Q = Q(\omega)$ defined as a function of the complex wavenumber k as follows (Borcherdt, 1973):

$$\frac{1}{Q(\omega)} \equiv \frac{\mathrm{Im}\left[k^2\right]}{\mathrm{Re}\left[k^2\right]} \tag{2.4}$$

where:

$$k^2 = \left(\frac{\omega^2}{v^2} - a^2\right) + i\left(\frac{2\omega a}{v}\right) \tag{2.5}$$

Substituting eq. (2.5) into eq. (2.4) gives a quadratic equation for the attenuation coefficient, $a(\omega)$, given by:

$$a^2 + \left(\frac{2\omega Q}{v}\right) a - \frac{\omega^2}{v^2} = 0 \qquad (2.6)$$

The physical solution for this quadratic equation which does $a(\omega)$ positive is represented by:

$$a(\omega) = \frac{\omega}{v} Q \left[\sqrt{1 + Q^{-2}} - 1\right] \qquad (2.7)$$

Typically when Q values are estimated for different rocks (particularly consolidated rocks) using the seismic and sonic methods (field) and the ultrasonic method (laboratory), it happens that $Q >> 1$ (or, $Q^{-1} << 1$). Then, eq. (2.7) can be approximated as follows:

$$\sqrt{1 + Q^{-2}} \cong 1 + \frac{1}{2} Q^{-2} \qquad (2.8)$$

and

$$a(\omega) = \frac{\omega}{v} Q \left[1 + \frac{1}{2} Q^{-2} - 1\right] = \frac{\omega}{2vQ} \qquad (2.9)$$

Eq. (2.9) represents a positive function linearly dependent on the angular frequency, ω. This means that the high-frequency components of the waveform (eq. 2.2) are more attenuated than the low frequencies due to the factor $e^{-a(\omega)x}$. One assumption made in obtaining the above formulae for $a(\omega)$ states that Q is constant over an entire frequency range which has been shown by certain experimental results on dry rocks (Murphy, 1982; Spencer, 1981) as indicated in Figure 2.2.

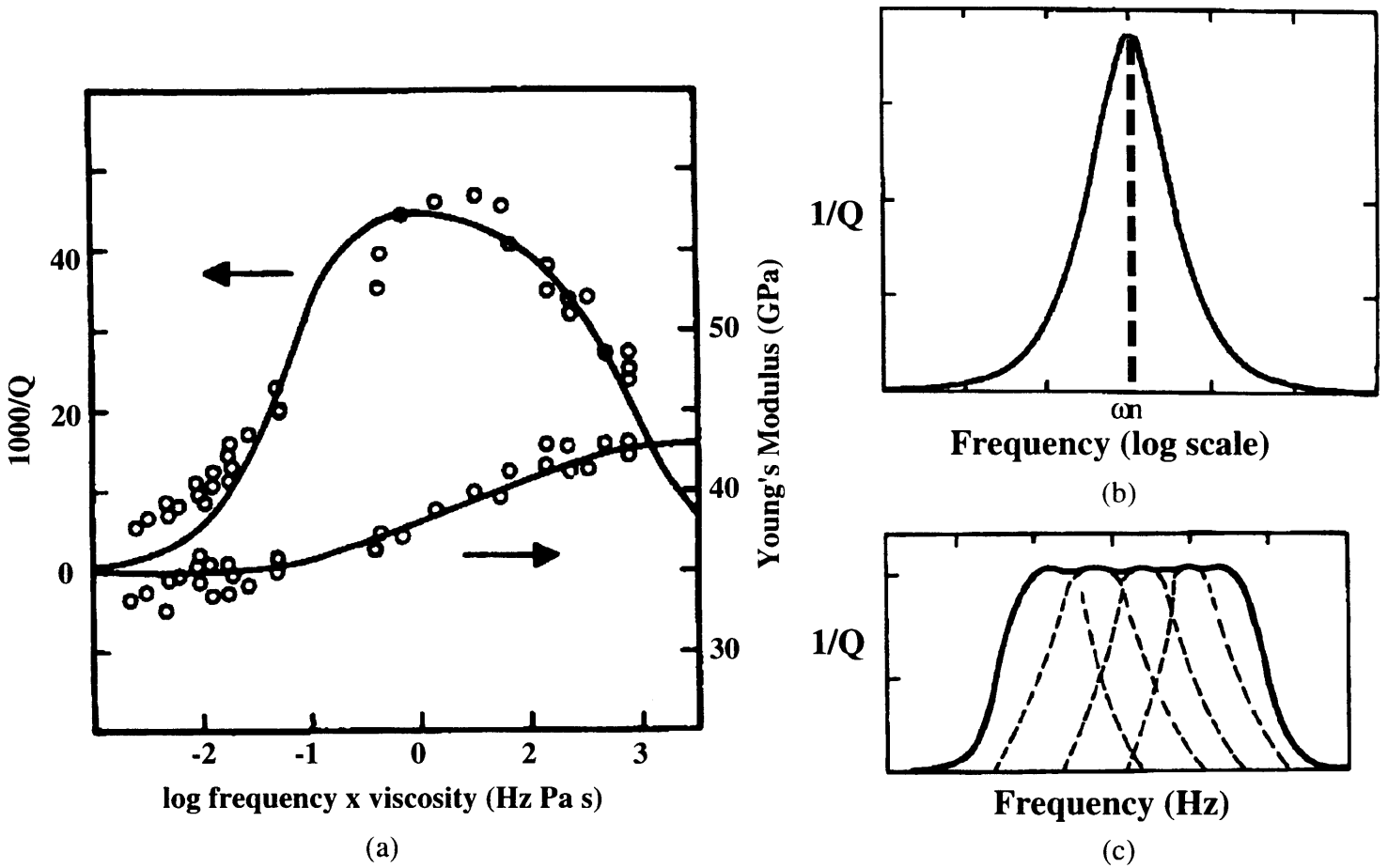

Fig. 2.2 Q measurements and models. (a) Seismic extensional attenuation and Young's modulus measured as a function of frequency times pore fluid viscosity in a Coconino SS. (After Tittmann *et al.*,1983) (b) Frequency-dependent attenuation for a SLM model. The maximum attenuation (1/Q) is obtained for the frequency w_n. (c) A superposition of different curves like (b) with different frequencies w_n produces the result that the quality factor Q remains constant over wide frequency ranges (after Liu *et al.*, 1976).

Several mathematical models have been used to represent these experimental results: *e.g.* the NCQ model (Liu *et al.*, 1976) based on direct superposition of different SLM models (Bourbie *et al.*, 1987) and the CQ model introduced by Kjartansson (1979), where Q is strictly independent of frequency.

2.1.2 Velocity dispersion

Another less evident effect of attenuation is velocity dispersion or the variation of the propagation velocity of the waveform with frequency. Theory and experimental measurements (Lomnitz, 1956, 1957) show that velocity dispersion can be expressed as:

$$v(\omega) = v(\omega_o)\left[1+\frac{1}{\pi Q}\ln\left(\frac{\omega}{\omega_o}\right)\right] \qquad (2.10)$$

where $v(\omega)$ represents the phase velocity (section 2.2.3), Q is the quality factor (assumed constant) and ω_o is named the reference frequency (Figure 2.3). Hence, for constant Q, the attenuation coefficient $\alpha(w)$ will not be exactly proportional to frequency because a constant-Q material will generally have a frequency-dependent phase velocity. Cerveny and Frangie (1982) show that the product $v(\omega)Q(\omega)$ is independent of frequency.

2.2 Velocity anisotropy

A property is anisotropic if depends on the direction in which it is measured; otherwise, the property is said to be isotropic. Considering waves propagating through some rock, if the rock exhibits anisotropy, the waves will travel through it with different velocities in different directions. This phenomenon, called elastic anisotropy, occurs in the rocks if there is a spatial ordering or preferred direction of crystals, grains, cracks, bedding planes, joints or fractures (essentially an alignment of strengths or weaknesses) on a scale significantly smaller than the length of the wave. This alignment causes waves to

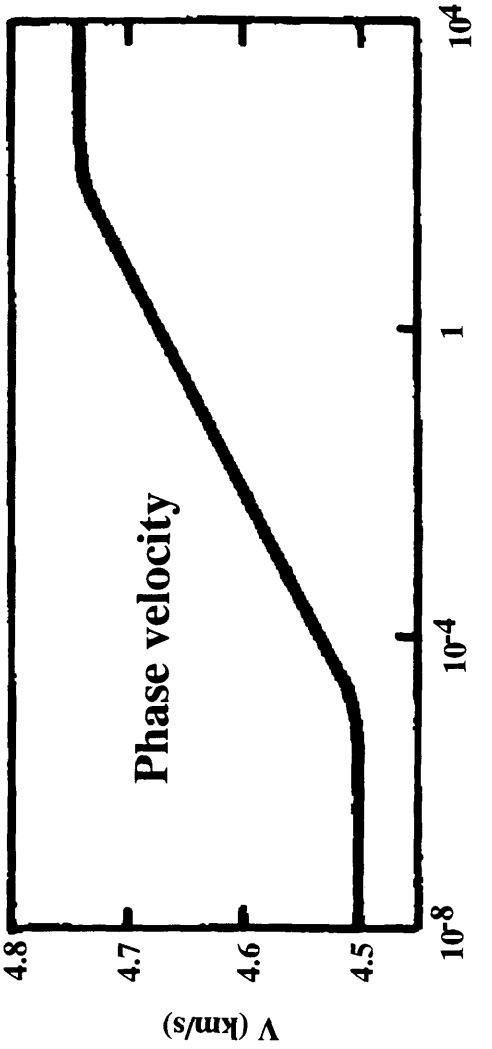

Fig. 2.3 Typical velocity dispersion curve (after Liu *et al.*, 1976).

propagate fastest in the stiffest direction (Anderson *et al.*, 1974; Crampin, 1978, 1981, 1984a,b; Crampin *et al.*, 1984; Sheriff, 1984).

Thomsen (1986), analyzing velocity anisotropy for a number of sedimentary rocks from ultrasonic velocity measurements (laboratory data) and seismic-band velocity measurements (field data), concluded that most of these rocks have anisotropy in the weak-to-moderate range (less than 20%). Then, he elaborated a number of approximate expressions for the case of weak-elastic anisotropy, which is considered the most common type of anisotropy for sedimentary rocks.

2.2.1 General classification of anisotropic materials

In seismic exploration, elastic anisotropy is often classified into two oversimplified but convenient models:

a) Transverse isotropy (or hexagonal symmetry) with a vertical axis of symmetry (TI). This model is a commonly occurring form of anisotropy and simulates the effect on the propagating wave produced by a sequence of thin (relative to a seismic wavelength), horizontal, isotropic layers (Figure 2.4a). An example of this kind of velocity anisotropy would be a clastic sequence consisting of alternating sandstones and shales.

b) Azimuthal anisotropy. This corresponds to a material with aligned vertical weaknesses such as cracks or fractures, or with unequal horizontal stresses with a non vertical axis of symmetry (Figures 1.1 and 2.4c). A dipping transversely isotropic medium could exhibit azimuthal anisotropy too; in this case, the symmetry axis is not exactly a horizontal axis (Figure 2.4b). In this thesis, the terms "TI" and "transversely isotropic" are understood to imply a vertical symmetry axis, unless otherwise specified.

Figure 2.5 shows what happens when P, SV and SH waves through TI and azimuthally anisotropic media. A seismic line direction is given so that SV-wave (in-line) and SH-wave (transverse) polarizations may be defined. P-wave, as well as both polarizations of S-wave propagation are considered in both a vertical and horizontal direction.

For TI materials P-wave propagation is generally faster horizontally, parallel to layering, than vertically, across layering (Figure 2.5a). Vertically propagating SV and SH

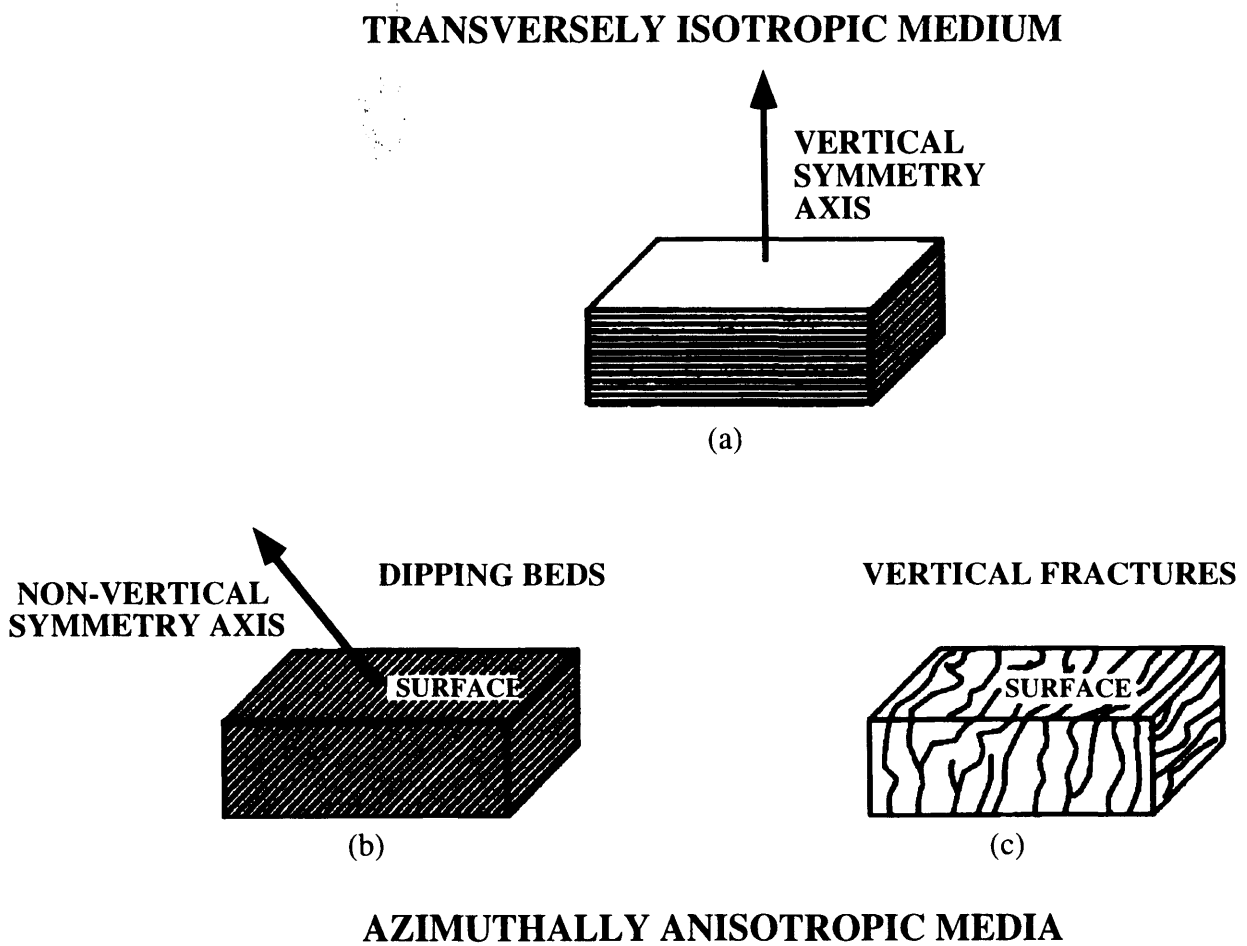

Fig. 2.4 **General classification of anisotropic materials.** (a) Transverse isotropy. (c) azimuthal anisotropy. (b) special case of (c) for dipping beds (After Tatham and McCormack, 1993).

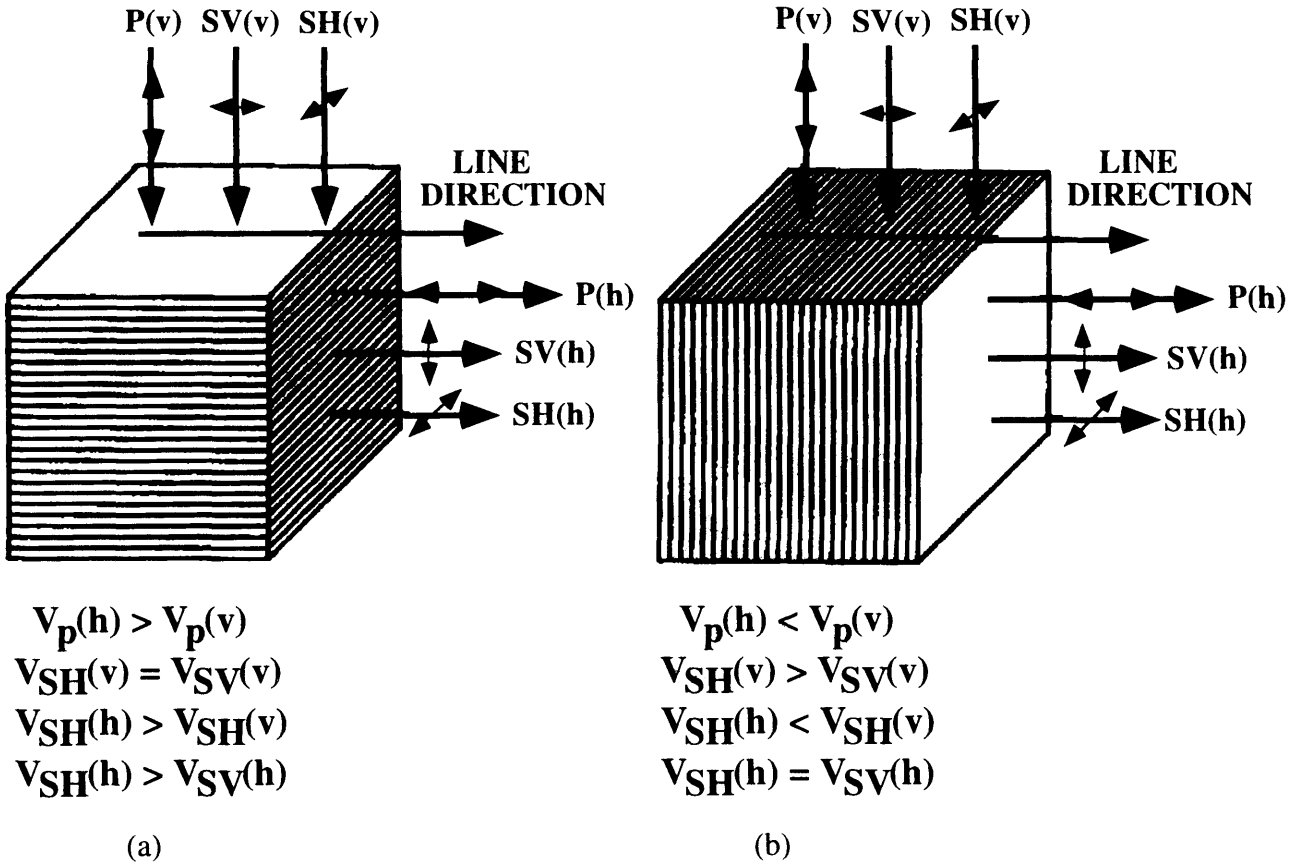

Fig. 2.5 Polarization and propagation directions for an anisotropic case of a layered medium. The polarizations are defined in terms of the indicated line direction, and both horizontal and vertical propagation directions areconsidered: (a) the case of flat layers, (b) the case of vertical layering or perhaps vertical fractures. The figures provide a means of rationalizing velocity differences with different propagation and polarization directions (after Tatham and McCormack, 1993).

waves sample identical bulk elastic properties in TI media, and thus $V^{v}_{SH} = V^{v}_{SV}$, where the superscript indicates the propagation direction. In contrast, a horizontally propagating SH-wave is faster than a horizontally propagating SV-wave, *i.e.* $V^{h}_{SH} > V^{h}_{SV}$. A similar situation like that observed for *P* waves, is obtained for an SH-wave propagating along layers with respect to an SH-wave propagating vertically, *i.e.* $V^{h}_{SH} > V^{v}_{SH}$ (Tatham and McCormack, 1993).

The same velocity analysis as done for P, SV and SH waves propagating through a TI medium can be realized for the propagation of these waves across an azimuthally anisotropic material (Figure 2.5b). The experiments on rocks presenting this kind of velocity anisotropy show that $V^{h}_{P} < V^{v}_{P}$ and $V^{h}_{SH} < V^{v}_{SH}$, in other words, both P and SH waves travel faster along the fracture direction than crossing the fractures (Tatham and McCormack, 1993).

2.2.2 Mathematical description of anisotropic materials: Stiffness tensor

The Kelvin-Christoffel equations (Musgrave, 1970; Nye, 1985; Cheadle *et. al.*, 1991) relate the phase velocity (section 2.2.3) and particle motion (or polarization) to the density and elastic constants, or stiffnesses as follows:

$$\rho v^{2} p_{i} = C_{ijkl} n_{j} n_{k} p_{l} \qquad (i,j,k,l = 1,2,3) \tag{2.12}$$

where v is phase velocity, ρ is density, p_{i} is the unit polarization vector, n_{r} is the unit slowness (or wavefront-normal) vector and C_{ijkl} is the fourth-order stiffness tensor of the medium having well known symmetries: $C_{ijkl} = C_{ijlk} = C_{jikl} = C_{klji}$, resulting that

there are only 21 independent stiffnesses, C_{ijkl}. This tensor can be also written as a second-order (6x6) symmetric matrix

$$C_{ijkl} \rightarrow C_{mn} \tag{2.13}$$

where

$$m = i \qquad if \quad i = j, \tag{2.14}$$

$$m = 9-(i+j) \qquad if \quad i \neq j \tag{2.15}$$

and *n* and *kl* are analogous to m and ij.

For an isotropic media the matrix C_{mn} assumes the simplest form given by:

$$C_{mn} = \begin{bmatrix} C_{33} & (C_{33}-2C_{44}) & (C_{33}-2C_{44}) & & & \\ & C_{33} & (C_{33}-2C_{44}) & & & \\ & & C_{33} & & & \\ & & & C_{44} & & \\ & & & & C_{44} & \\ & & & & & C_{44} \end{bmatrix} \tag{2.16}$$

Only the nonzero components in the upper triangle are shown; the lower triangle is symmetrical. These components are related to the Lame parameters λ and μ and to the bulk modulus K by:

$$C_{33} = \lambda + 2\mu = \mathrm{K} + \frac{4}{3}\mu \tag{2.17}$$

$$C_{44} = \mu \tag{2.18}$$

In the case of a transversely isotropic medium (the only case that will be considered here) we have five nonzero elastic constants because there exists a two-dimensional isotropy in the plane where all axes are equivalent (rotational symmetry around the *z*-axis), but the direction perpendicular to this plane is not equivalent to any of the axes in the plane (section 2.2.1). As result, the stiffness matrix C_{mn} for transverse isotropy is given by

$$C_{mn}^{TI} = \begin{bmatrix} C_{11} & (C_{11}-2C_{66}) & C_{13} & & & \\ & C_{11} & C_{13} & & & \\ & & C_{33} & & & \\ & & & C_{44} & & \\ & & & & C_{44} & \\ & & & & & C_{66} \end{bmatrix} \tag{2.19}$$

Here, the superscript indicates a transversely isotropic material with symmetry axis about the z-axis (vertical). A comparison of the isotropic matrix C_{mn}, equation (2.16), with the anisotropic matrix C_{mn}^{TI}, equation (2.19), shows how the former is a degenerate case of the latter, with:

$$C_{11} \rightarrow C_{33} \tag{2.20}$$

$$C_{66} \rightarrow C_{44} \tag{2.21}$$

$$C_{13} \rightarrow C_{33} - 2C_{44} \tag{2.22}$$

2.2.3 Phase and group velocities for weak anisotropy

In an anisotropic media the waves emanating from a point source are not, in general, spherical (Thomsen, 1986; Vestrum, 1994). Figure 2.6 shows a propagating wavefront generated by a point source in an anisotropic media. The wavefront is locally perpendicular to the propagation vector **k**, since **k** points in the direction of maximum rate of increase in phase. Since the wavefront is non-spherical, we have that the wavefront-normal angle θ (phase angle) is different from ϕ (group angle), the ray angle from the source point to the wavefront (Vestrum, 1994).

Additionally, if we define the group velocity, g, as the velocity at which energy travels away from the source, an observer standing at the point A could measure the time on a stopwatch between the instant that the source generated a wavefront and the instant it reached point A, naming it the group travel time. The distance between the source and point A divided by the group travel time will yield the group velocity. On the other hand, the phase velocity, v, is the velocity normal to the wavefront and is equal to the distance the wave has traveled normal to the plane wavefront between the point A and point B divided by the phase travel time needed by the wavefront to reach the point B from A (Vestrum, 1994).

The group and phase velocities are, in general, not equal in an anisotropic media. Except when, $\theta = 0°$ and $\theta = 90°$, *i.e.* vertical and horizontal propagations, respectively, does group velocity equal phase velocity. Several authors (Postma, 1955; Brown *et al.*, 1991 and Dellinger, 1991 among others) have shown that the relationship between the group velocity, **g**, and the phase velocity, **v**, can be expressed as

$$g(\phi) = \sqrt{v^2(\theta) + \left(\frac{\partial v}{\partial \theta}\right)^2} \tag{2.23}$$

where g and v represent the amplitude of the group and phase velocity vectors, respectively.

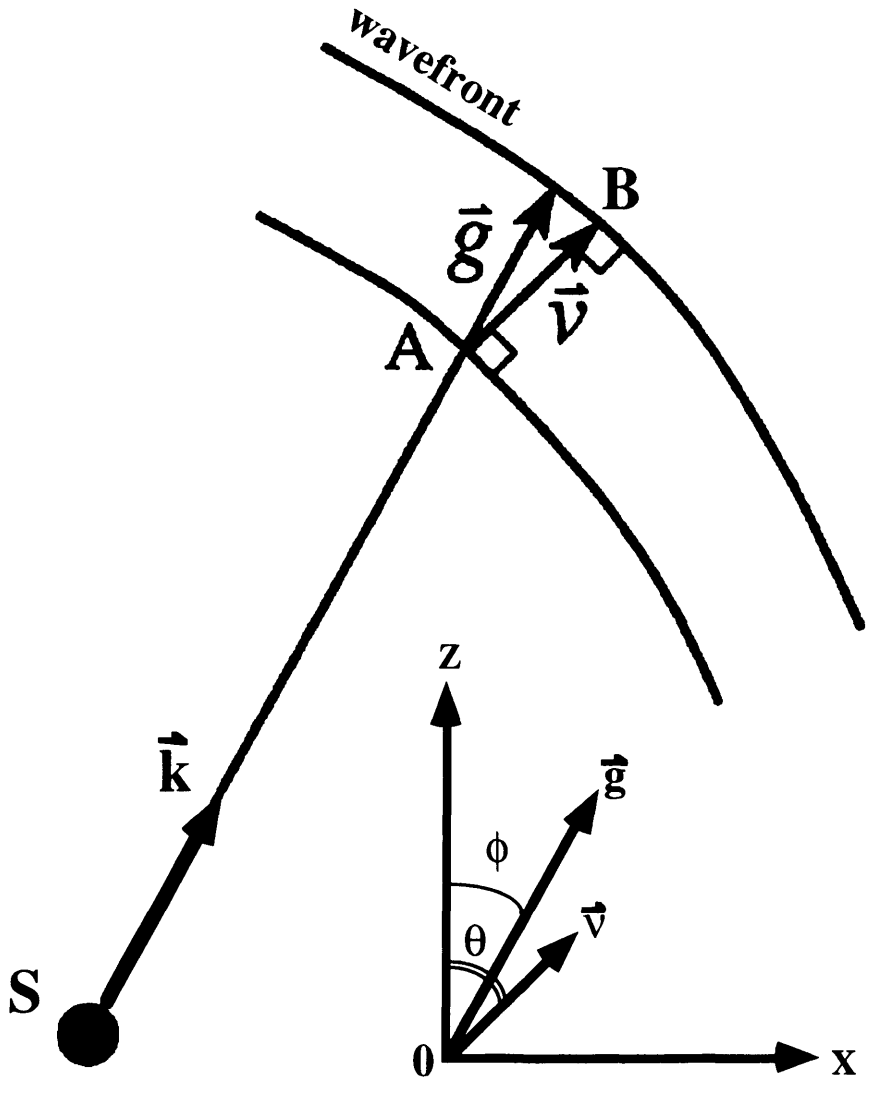

Fig. 2.6 Definitions of group and phase velocities. The phase velocity, v, is the velocity of the wave in a direction normal to the wavefront and the group velocity, g, is the velocity of energy transport away from the source. In an anisotropic media, the phase angle or wavefront-normal angle, θ, is different from the group angle, ϕ (after Vestrum, 1994).

As a result, the group velocity, g, and the group angle, ϕ, in the linear approximation (first order) for weak anisotropy (Thomsen, 1986) can be expressed as follows:

$$g = v\left[1 + \frac{1}{2v^2}\left(\frac{\partial v}{\partial \theta}\right)^2\right] \rightarrow g \cong v \tag{2.24}$$

and

$$\tan\phi = \tan\theta\left[1 + \frac{1}{\sin\theta\cos\theta}\frac{1}{v}\frac{\partial v}{\partial \theta}\right] \tag{2.25}$$

Additionally, Thomsen (1986) also showed that when the anisotropy is considered to be weak the phase velocity, v, for P, SV and SH waves can be approximated as:

$$v_P(\theta) = \alpha_0\left(1 + \delta\sin^2\theta\cos^2\theta + \varepsilon\sin^4\theta\right), \tag{2.26}$$

$$v_{SV}(\theta) = \beta_0\left[1 + \frac{\alpha_0^2}{\beta_0^2}(\varepsilon - \delta)\sin^2\theta\cos^2\theta\right], \tag{2.27}$$

$$v_{SH}(\theta) = \beta_0\left(1 + \gamma\sin^2\theta\right) \tag{2.28}$$

where $\alpha_0\left(=\sqrt{C_{33}/\rho}\right)$ and $\beta_0\left(=\sqrt{C_{44}/\rho}\right)$ represent the vertical speeds for P and S waves, respectively and ε, γ and δ are parameters that express the degree of anisotropy for a transversely isotropic media (Thomsen, 1986). These parameters are expressed as:

$$\varepsilon \equiv \frac{C_{11} - C_{33}}{2C_{33}} = \frac{v_P(\pi/2) - \alpha_0}{\alpha_0} \tag{2.29}$$

$$\gamma \equiv \frac{C_{66} - C_{44}}{2C_{44}} = \frac{v_{SH}(\pi/2) - \beta_0}{\beta_0} \tag{2.30}$$

$$\delta = 4\left[v_P(\pi/4)/\alpha_0 - 1\right] - \left[v_P(\pi/2)/\alpha_0 - 1\right] \tag{2.31}$$

where the angles are measured with respect to the z-axis (vertical) for a TI medium which represents its symmetry axis (Figure 2.4).

2.3 Anisotropic permeability

It is well known that porous media often present an additional kind of anisotropy, different from the elastic anisotropy (Gelinsky and Shapiro, 1994a,b; 1995). This is related to variation of the permeability and the formation factor with the direction of measurement. Sedimentary porous media, such as sandstones, have a layered structure and the permeability parallel to the layers is usually greater than in the perpendicular direction. The anisotropy of sandstones is generally associated with minute layering and grain orientation (Greenkorn *et al.*, 1964).

In fractured formations, horizontal permeability varies dramatically with azimuth, becoming high when the azimuth coincides with that of the fracture strike and low when it doesn't. The anisotropic permeability is intimately related to stress anisotropy, which influences fracture orientation, density and aperture, affecting well productivity (Ehlig-Economides *et al.*, 1990). Figure 2.7 shows the effect of various heterogeneities on the permeability anisotropy for sandstones.

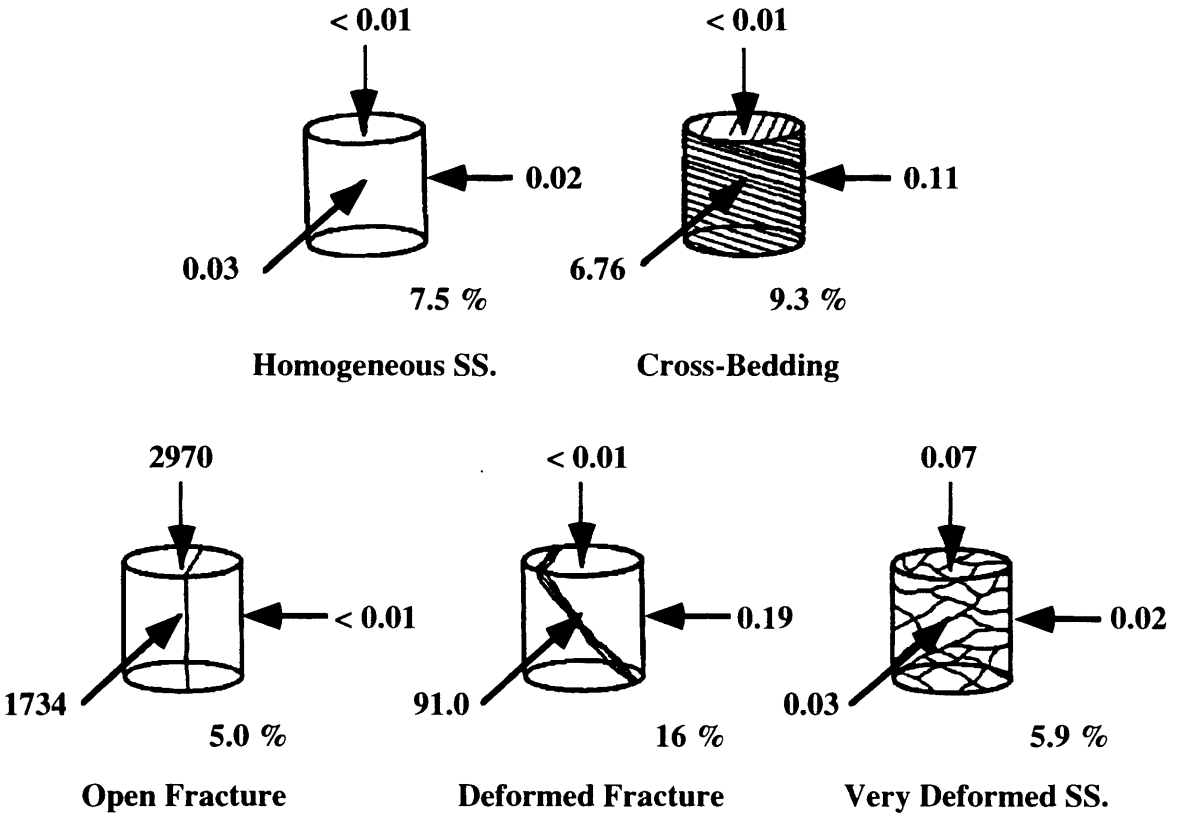

Fig. 2.7 The effect of various heterogeneities on 3-D whole-core permeability. Sample porosities are indicate in percent and permeabilities in mD (after Nelson, 1985).

2.3.1 Definition of permeability: Tensorial and directional

The permeability is a second rank tensor connecting fluxes and gradients (Dullien, 1979). The quantity of fluid transmitted in laminar flow through the effective porosity of a fluid-saturated medium is related to the driving agent (pressure gradient) by a permeability coefficient that defines the medium's ability to pass fluid (Dullien, 1979).

As a result of permeability anisotropy, at a given point in the porous medium the direction of the pressure gradient vector is, in general, different from that of the velocity vector related to the particle displacement (Figure 2.8). In this case, it is necessary to specify both the pressure gradient and the velocity vector fields in order to obtain a complete description of the anisotropic permeability (Dullien, 1979).

For a porous media displaying anisotropic permeability the presence of a pressure gradient, *e.g.* pointing in the x-coordinate direction, will result in three different flow rates in each of the x, y, and z directions, whereas in an isotropic permeable medium the flow is restricted to the x direction. Then, Darcy's law, which relates the pressure gradient, $-\nabla \mathbf{P}$, with the resultant phase velocity vector, $\mathbf{v}$, can be expressed as follows:

$$v_i = -\frac{1}{\eta}\left(k_{i1}\frac{\partial P}{\partial x_1} + k_{i2}\frac{\partial P}{\partial x_2} + k_{i3}\frac{\partial P}{\partial x_3}\right) \qquad (i = 1,2,3) \tag{2.32}$$

where k_{ij} represent the components of the symmetric permeability tensor, K^*, η is the viscosity of the fluid in the pores of the rock, and v_i are the components of the phase velocity vector (Dullien, 1979). Alternatively, in vector notation, eq.(2.32) becomes:

$$\mathbf{v} = -\left(K^*/\eta\right)\nabla \mathbf{P} \tag{2.33}$$

If the principal axes of the permeability tensor are chosen as coordinate axes, the permeability tensor becomes diagonal, which lets us more easily relate the directional

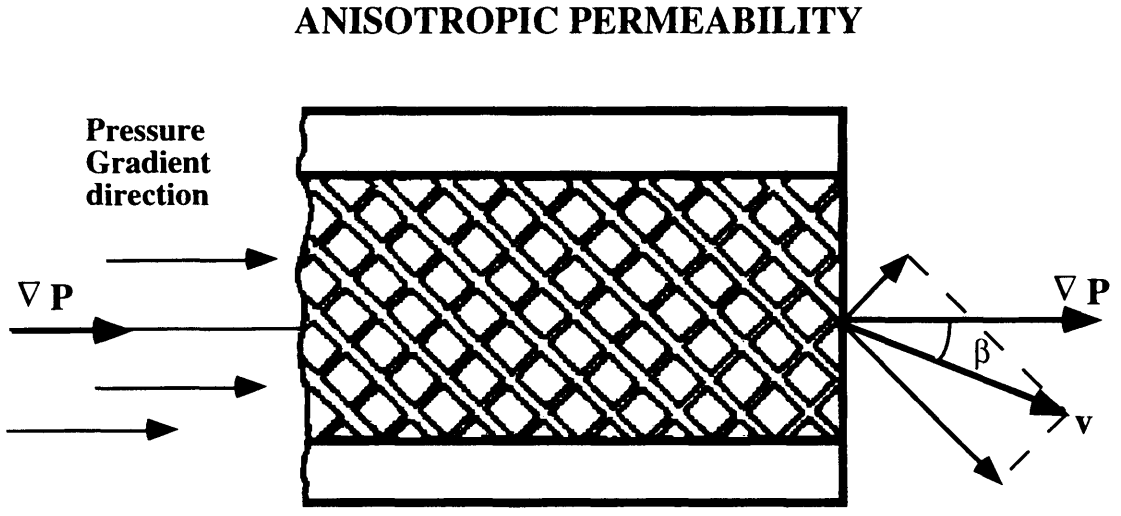

Fig. 2.8 Schematic diagram showing directions of velocity and pressure gradient vectors in an anisotropic sample. The anisotropic permeability tensor is simulated by two mutually perpendicular sets of capillaries of different diameters (after Dullien, 1979).

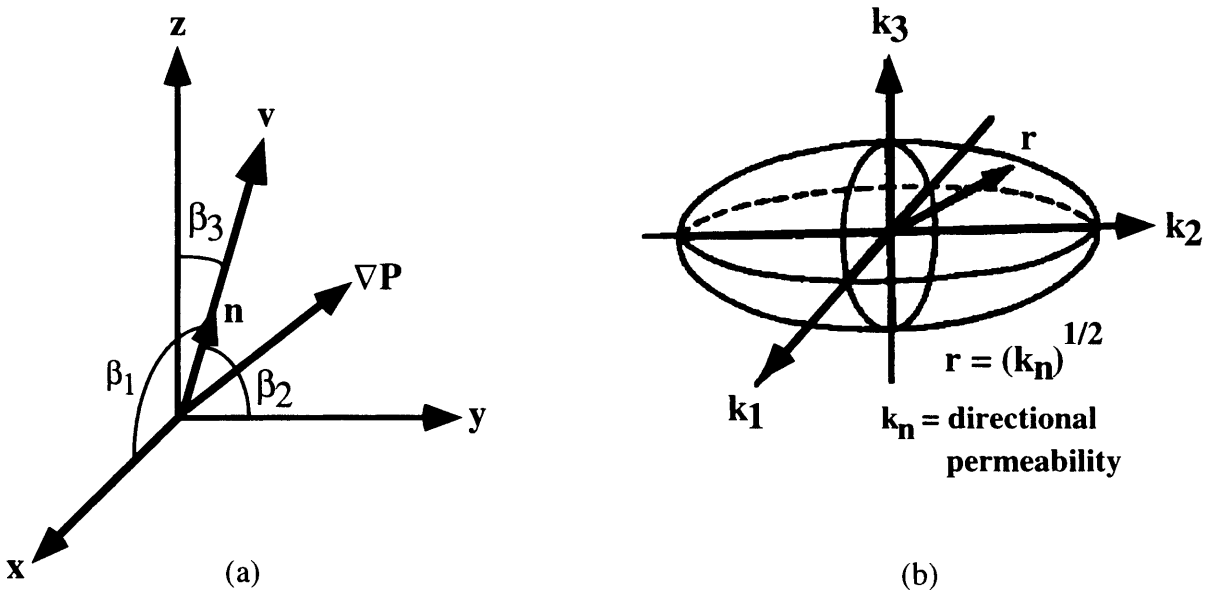

Fig. 2.9 Definition of the permeability ellipsoid: (a) orthogonal representation of the velocity and pressure gradient vectors defining the angles madeby the unit vector **n** with the principal axes; (b) three-dimensional representation of the permeability ellipsoid.

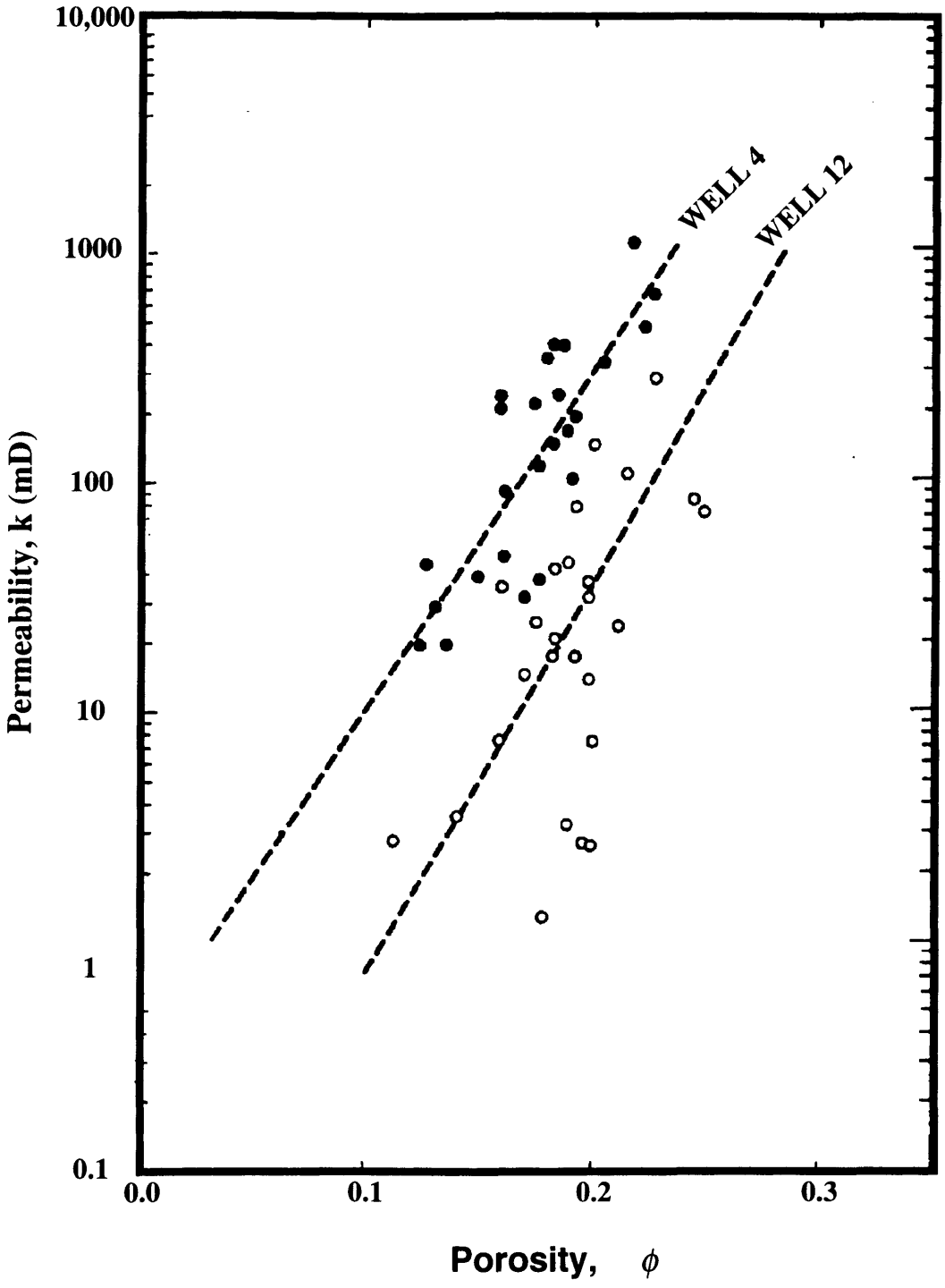

Fig. 2.10 Permeability-porosity data and regression models from the Permian Rotliegend sandstone (after Diederix, 1982).

Klimentos and McCann, 1990; Akbar *et al*, 1993; Best *et al*, 1994; Gelinsky and Shapiro, 1994a,b; 1995; among others) that there exists relationships among P and S-wave velocities and attenuations with clay content, porosity and permeability.

Han *et al.* (1986) and Han (1987) using least-squares fits to experimental velocity data from seventy-five different shaly sandstones samples with porosities ranging from 2 to 30%, volume clay content C ranging from 0 to 50%, confining pressure of 40 MPa, and pore pressure of 1MPa, found both V_P and V_S to be linearly correlated with porosity and clay content in water-saturated shaly sandstones according to:

$$V_P(km/s) = 5.59 - 0.0693\phi - 0.0218C \quad (2.36)$$

$$V_S(km/s) = 3.52 - 0.0491\phi - 0.0189C \quad (2.37)$$

with standart deviations of less than 3 % and 5 % for V_P and V_S, respectively (Figure 2.11). The principal effect of the clay content on P and S-wave velocities is to reduce their values by softening the sandstone matrix (Han *et al.*, 1986).

Other experiments on shaly sandstones (Klimentos, 1991) show that the effect of permeability alone on V_P is negligible in rocks with identical porosity, lithology, and negligible or similar clay content. Hence, the velocity-permeability relationship is controlled by the relationships between velocity and clay content and those between permeability and clay content. Klimentos (1991) using pressure conditions similar to those used by Han *et al.* (1986) shows that the relationship connecting P-wave velocity, V_P, porosity ϕ (percent), clay content C (percent) and permeability k (millidarcy) is given by:

$$V_P(km/s) = 5.66 - 0.0611\phi - 0.0353C + 0.0007k \quad (2.38)$$

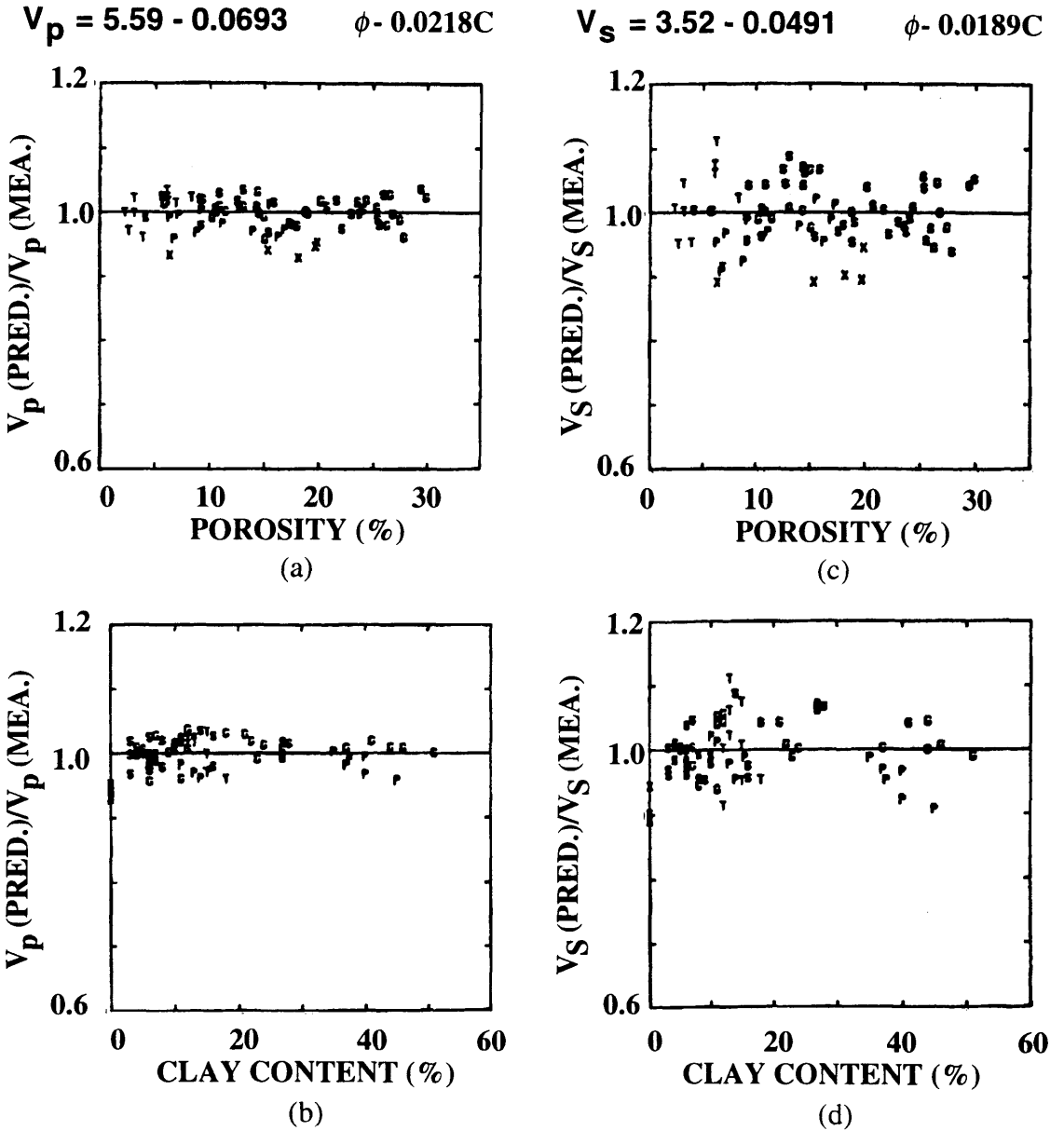

Fig. 2.11 Linear fit between velocity and porosity and clay content. The goodness of the fit is observed by plotting the predicted velocity divided by the measured velocity for P and S waves. (a) V_p relative to porosity, (b) V_p relative to clay content, (c) V_S relative to porosity, and (d) V_S relative to clay content. In all cases a confining pressure of 40 MPa and a pore pressure of 1.0 MPa have been used (after Han *et al.*, 1986).

with a correlation coefficient R^2 = 0.96 (Figure 2.12). As result, the *P*-wave velocity information only, may distinguish very tight from very permeable rocks via the velocity-clay and permeability-clay interdependencies, but it is not adequate for a precise permeability prediction (Klimentos, 1991). The fact that the velocities for P and S waves are not perfectly predicted by the relationships indicated in the eq. (2.36), eq. (2.37) and eq. (2.38), indicates that they are dependent on additional parameters such as the diagenetic history of the rock, the type and habit of the intra-pore clays, the type of inter-granular cement, the shape of the pores and the type and degree of pore-fluid saturation (Castagna *et al*, 1985).

The seismic attenuation is another rock property which is also affected by intrapore clays in sandstones. Klimentos and McCann (1990) show, after measuring the attenuation coefficients of P waves in several sandstones at confining pressures and ultrasonic frequencies, that for these samples, compressional wave attenuation (a_P, dB/cm) is related to clay content C (percent) and porosity ϕ (percent) by:

$$a_P = -0.132 + 0.0315\phi + 0.241C \qquad (2.39)$$

with a correlation coefficient R^2 = 0.88 (Figure 2.13). By comparing eq. (2.36) with eq. (2.39) we see that, unlike the P-wave velocity, the attenuation for P waves is strongly affected by clay content which determines permeability (Akbar *et* al, 1993). On the other hand, the relationship between attenuation and permeability is less well defined: those sandstone samples with permeabilities less than 50 mD have high attenuation coefficients (generally greater than 1 dB/cm) while those with permeabilities greater than 50 mD have low attenuation coefficients (generally less than 1 dB/cm) at 1 MHz at 40 MPa (Figure 2.14). Adittionally, Klimentos and McCann (1990) found that the best-fit statistical relationship, in a logarithmic plot of the *P*-wave quality factor Q_P versus clay content C calculated from the attenuation coefficient measured for these sandstone samples (Figure 2.15) is given by:

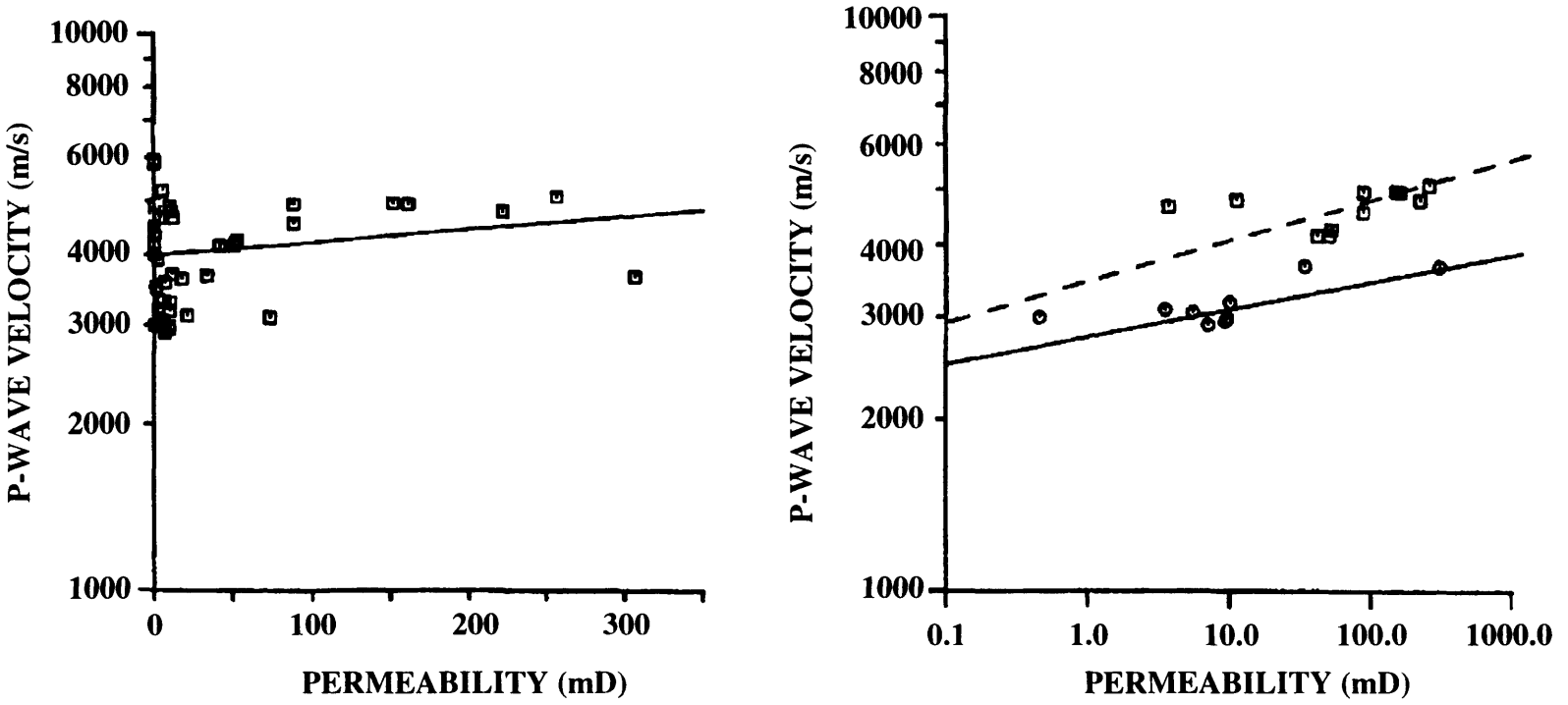

Fig. 2.12 *P*-wave velocity and permeability relationships. (a) Measured *P*-wave velocity as a function of permeability for samples with porosities 6-36 percent. (b) Log-log plot of *P*-wave velocity as a function of permeability for samples with average porosities 15± 1 percent (squares) and 28± 1 percent (circles), with linear best fits. A confining pressure of 40 MPa and a frequency of 1 MHz were considered in all cases (after Klimentos, 1991)

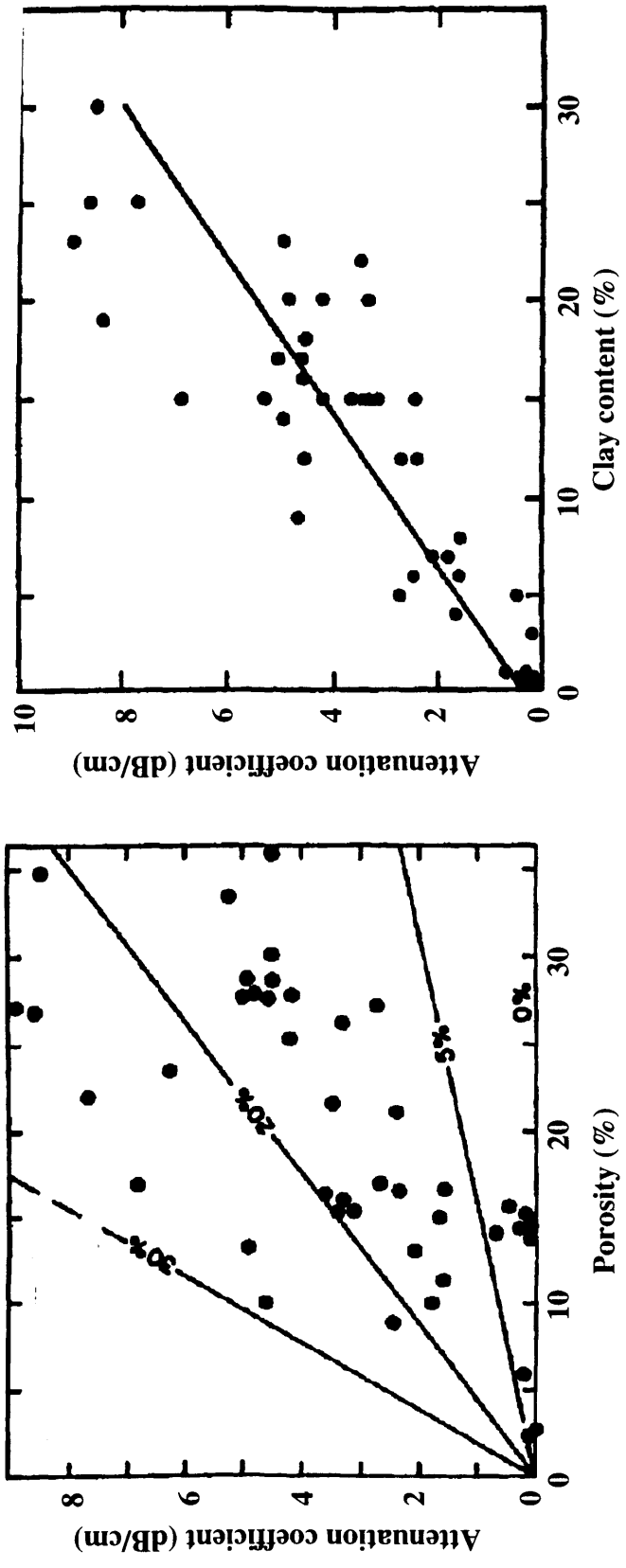

Fig 2.13 Attenuation, porosity and clay content relationships. (a) Attenuation coefficient versus porosity for sandstone samples. The solid lines separate samples of given percent clay content. The regions correspond to 0 to 5 %, 5 to 20 %, and 20 to 30 %, respectively. (b) Attenuation coefficient versus clay content for the same samples. A confining pressure of 40 MPa and a frequency of 1MHz were considered in all the measurements (after Klimentos and McCann, 1990).

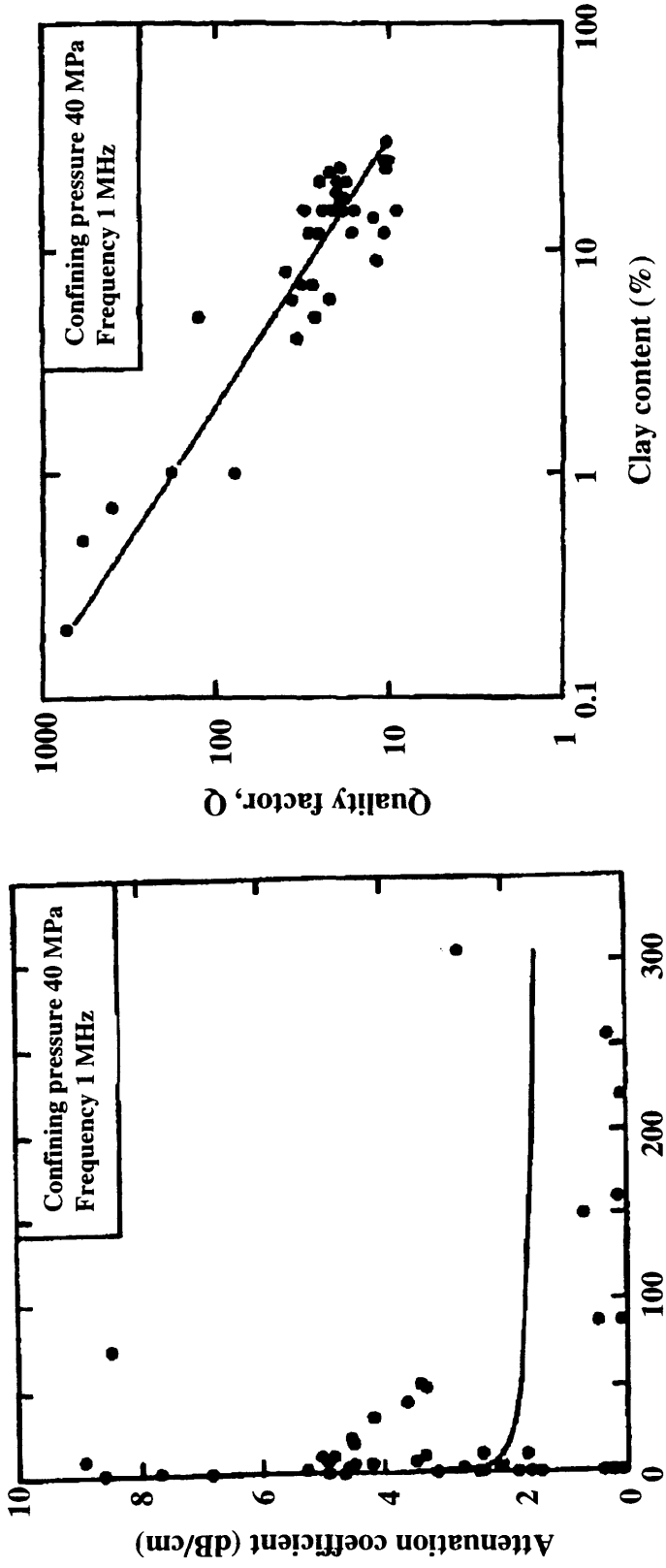

Fig. 2.14 Attenuation coefficient versus permeability for sandstone samples (after Klimentos and McCann, 1990)

Fig. 2.15 Quality factor versus clay content for sandstones samples of porosities 6 to 36 %. Logarithmic plot. (after Klimentos and McCann, 1990).

$$Q_P = 179C^{-0.843} \tag{2.40}$$

where there is a strong systematic relationship between clay content and permeability.

Akbar *et al.* (1993) show that the attenuation, rather than the velocity, is strongly correlated with permeability by examining a three-dimensional theoretical model of a cylindrical pore filled with viscous fluid and embedded in an infinite isotropic elastic medium. Also, Akbar *et al.* (1993) find that, when a P-wave propagates perpendicular to the preferred pore orientation, attenuation is always higher than when a wave propagates parallel to this orientation. Furthermore, the ratio of these two attenuation values increases with the increase of the pore's radius and the decrease of frequency and saturation, while the permeability-attenuation relation is characterized by a peak which shifts toward higher permeabilities as frequency increases (Figure 2.16).

Best *et al.* (1994) confirm the results obtained by Klimentos and McCann (1990) that the *P*-wave quality factor, Q_P, is strongly correlated with the volume content of intra-pore clay. They demonstrate that this relationship is also true for the S-wave quality factor, Q_S, and the dependence of both Q_P and Q_S on porosity is weak as indicated by the following relationships:

$$Q_P = 86.0 - 0.703\phi - 1.27T \tag{2.41}$$

$$Q_S = 59.4 - 0.917\phi - 0.673T \tag{2.42}$$

where T represents the sum of the volume percentages of all pore-filling minerals found within these sandstones (total pore fill as clays, micritic calcite and sparry calcite).

Their results verify that P- and S-wave velocities are independent of permeability (Figure 2.17a) as shown by Klimentos (1991), while all high permeability rocks (100 -

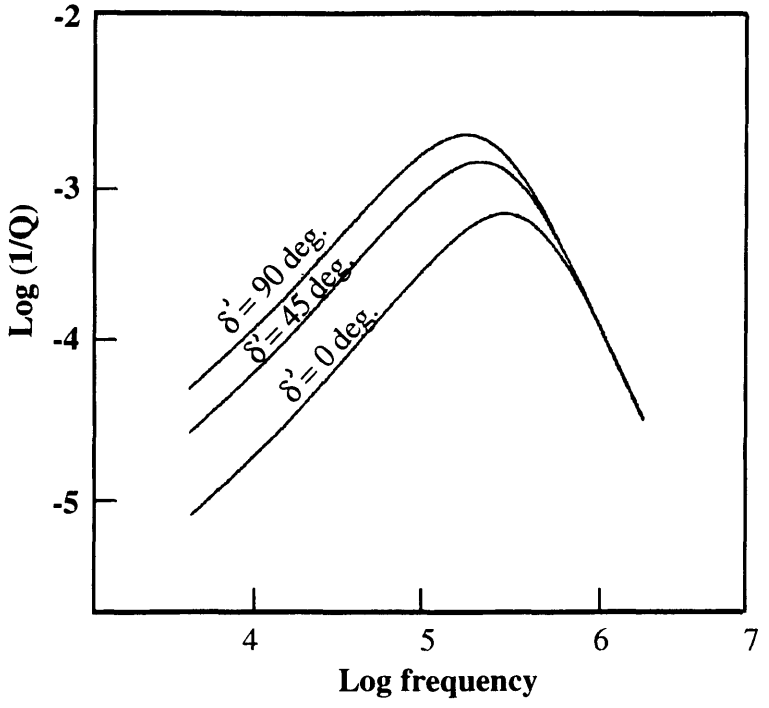

(a)

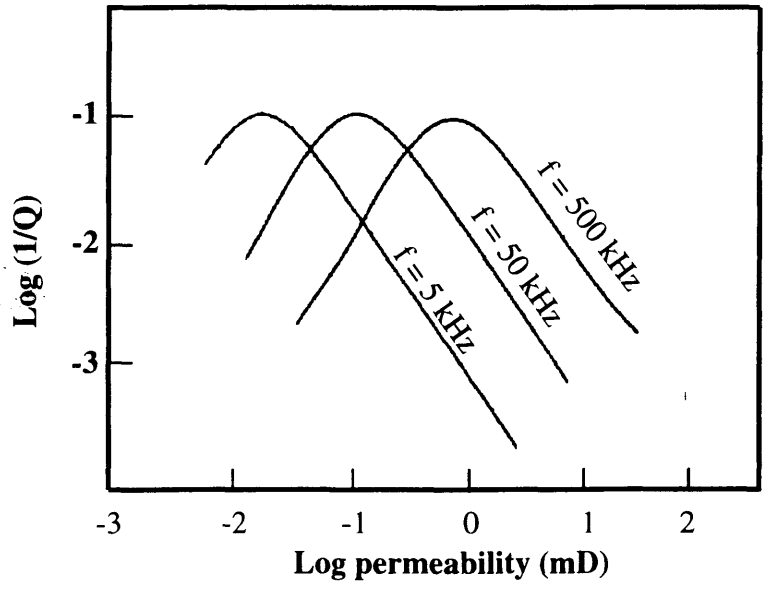

(b)

Fig. 2.16 (a) The plot of log Q^{-1} *vs* log f for different incident angles.
(b) Log Q^{-1} vs log k for different frequencies (after Akbar *et al.*, 1993).

300 mD) have relative high quality factors as shown in Figure 2.17b (Best *et al.*, 1994).

Figure 2.18 shows a graph of *P*-wave quality factor, Q_P versus P-wave velocity for sandstones and shales, obtained from Hauge (1981) from VSP data, Klimentos and McCann (1990) and Best *et al.* (1994). The rocks whose velocities and quality factors plot in the shaded region have an average permeability of 100 ± 30 mD, while those which plot outside this region have an average permeability of 10 ± 7 mD. Given the dominant effect of the pore-filling material on both quality factor and permeability (Klimentos, 1991), high-permeability sandstones plot in the high-quality-factor region and *vice-versa* (McCann, 1994).

Gelinsky and Shapiro (1994a, b; 1995) developed a theoretical approach for representing the influence of anisotropic permeability on seismic velocity and attenuation for low- and high-frequency ranges. They modeled the wave propagation through a homogeneous, isotropic, liquid-saturated porous media having permeability anisotropy using Biot-theory (Biot, 1956a, b; 1962). They assumed that the fractures or layers contribute to the permeability anisotropy and the anisotropy of wave propagation is then a dynamic effect, caused only by the anisotropic permeability.

By using this approach Gelinsky and Shapiro (1994a, b; 1995) derive some analytical formulaes describing the P-, S- and SH-phase velocities and seismic attenuations in the low frequency range (seismic frequency range). The expressions for their phase velocities are:

$$v_P = \alpha_0 \left[1 + \frac{1}{2} \left(\frac{\omega}{\omega_{c\perp}} \right)^2 f_P(\theta) \right] \tag{2.43}$$

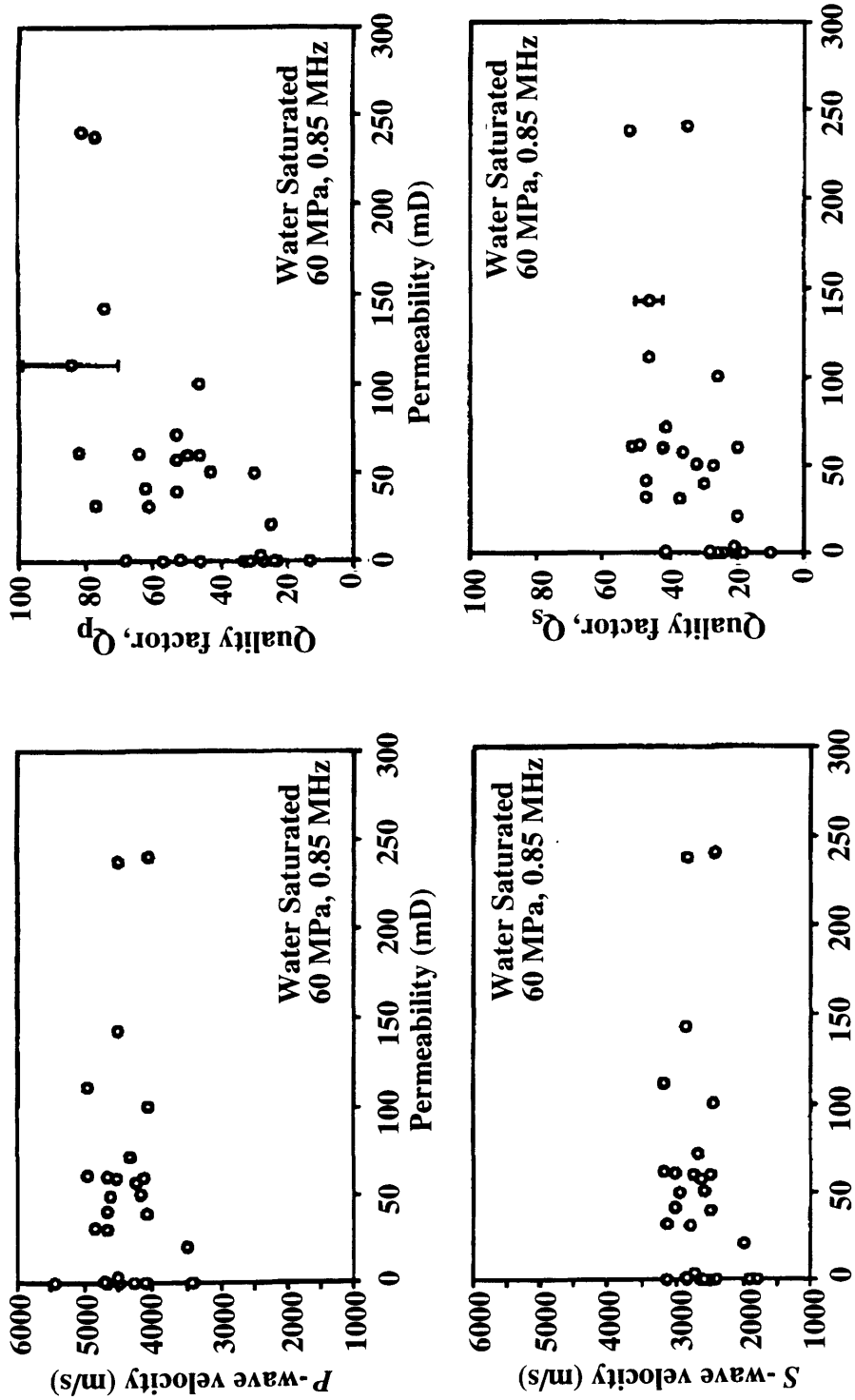

Fig. 2.17 *P*- and *S*-wave velocities, attenuations and permeability relationships. (a) Scatter diagrams of the ultrasonic V_p and V_s velocities of 29 water-saturated rock samples against permeability at 60 MPa. (b) Scatter diagrams for Q_p and Q_s as function of the permeability (after Best *et al.*, 1994).

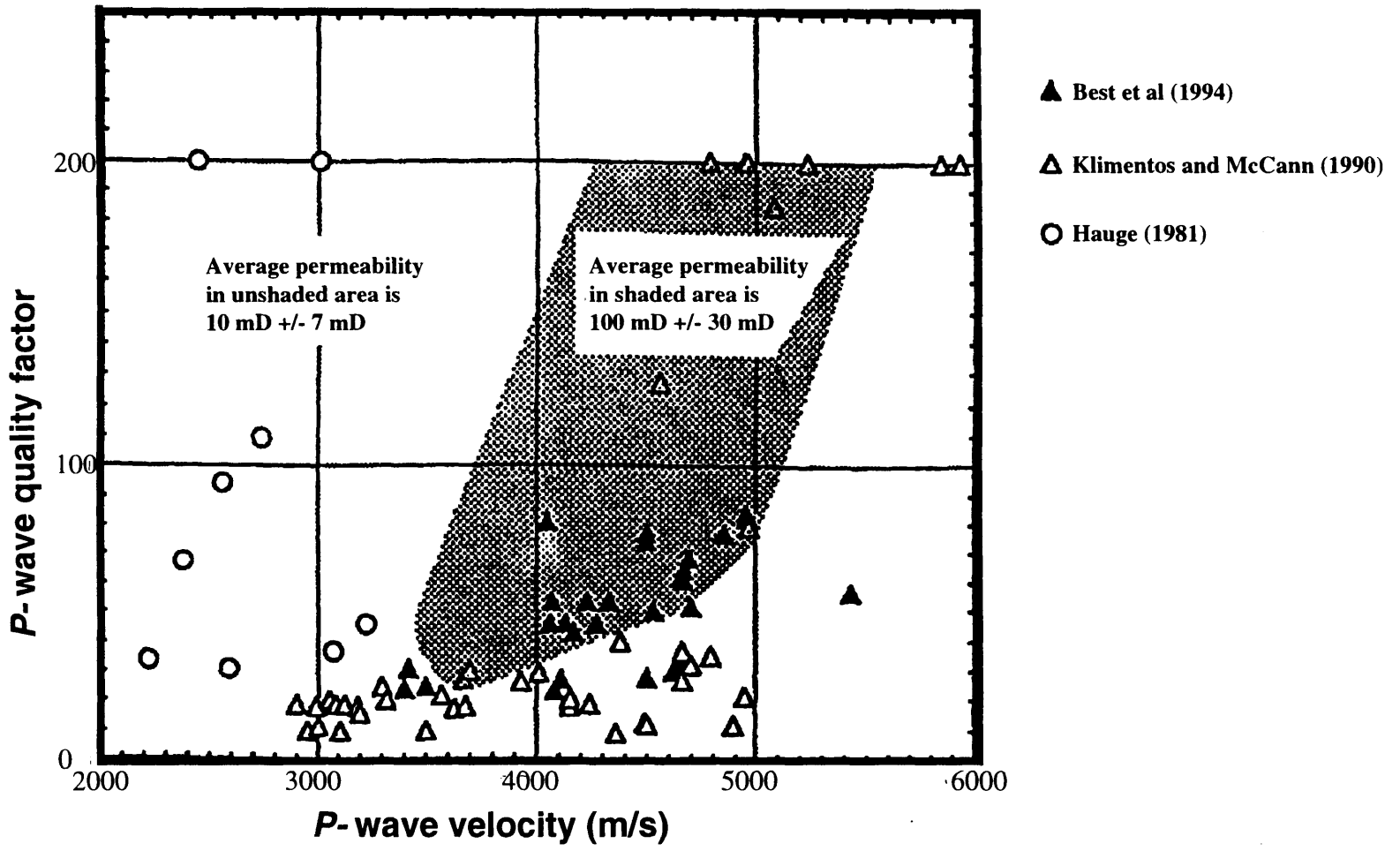

Fig. 2.18 Quality factor *vs.* velocity of *P*-wave for sandstones and shales. Seismic data categorise according to sample permeability (after McCann, 1994).

$$v_{SV} = \beta_0 \left[1 + \frac{1}{2} \left(\frac{\omega}{\omega_{c\perp}} \right)^2 f_{SV}(\theta) \right] \tag{2.44}$$

$$v_{SH} = \beta_0 \left[1 + \frac{1}{8} \left(\frac{\omega}{\omega_{c\perp}} \right)^2 \gamma_f^3 \left(4\frac{\tau}{\phi} - \gamma_f \right) \right] \tag{2.45}$$

On the other hand, the corresponding expressions for their seismic attenuations are given by:

$$a_P = \frac{1}{2\alpha_0} \left(\gamma_f - \sigma_K \right)^2 \frac{\omega^2}{\omega_{c\perp}} \left(\sin^2\theta + \frac{\omega_{c\perp}}{\omega_{c\parallel}} \cos^2\theta \right) \tag{2.46}$$

$$a_{SV} = \frac{1}{2\beta_0} \gamma_f^2 \frac{\omega^2}{\omega_{c\perp}} \left(\cos^2\theta + \frac{\omega_{c\perp}}{\omega_{c\parallel}} \sin^2\theta \right) \tag{2.47}$$

$$a_{SH} = \frac{1}{2\beta_0} \gamma_f^2 \frac{\omega^2}{\omega_{c\perp}} \tag{2.48}$$

where f_P and f_{SV} are variables that depend on the propagation direction, θ with respect to the symmetry axis ($\theta = 0^\circ$ if the propagation is along vertical axis for a TI medium and $\theta = 90^\circ$ if perpendicular to this axis), petrophysical parameters and permeability anisotropy; ω is the angular frequency; τ is the tortuosity (scalar); ϕ is the porosity (fraction); γ_f is the ratio between fluid and total densities ($=\rho_f/\rho$); σ_K is a dimensionless rock modulus (Geertsma and Smit, 1961), and α_0, β_0 represent the vertical phase velocities for P and S waves (section 2.2.3). The anisotropic permeability appears in

critical frequencies $\omega_{c\parallel}$ and $\omega_{c\perp}$, which are proportional to the inverse permeabilities measured parallel and in a plane perpendicular to the symmetry axis, respectively. Then:

$$\omega_{c\parallel} = \frac{\eta}{k_{\parallel}\rho} \tag{2.49a}$$

$$\omega_{c\perp} = \frac{\eta}{k_{\perp}\rho} \tag{2.49b}$$

where $k_{\parallel}$ is the measured permeability parallel to the symmetry axis, $k_{\perp}$ is the measured permeability perpendicular to the symmetry axis and η is the viscosity of the fluid.

Also, Gelinsky and Shapiro (1994a, b; 1995) conclude that even without any poroelastic matrix anisotropy both velocity and attenuation are affected by an anisotropic permeability. In a low frequency range (0 - 10 kHz) the permeability anisotropy does not affect the seismic phase velocities for P and SV waves, but it strongly affects the corresponding attenuations which become directional (Figure 1.3). For P and SV waves and frequencies around of 200 kHz, the phase velocities show maximum anisotropy while the attenuation anisotropy is reduced and no longer directional (isotropic). At ultrasonic frequencies, higher than 200 kHz, the degree of velocity anisotropy is reduced and the attenuation anisotropy is increased again (Gelinsky and Shapiro, 1994a, b; 1995).

2.6 Effects on velocity and attenuation due to effective pressure and saturation

Another important parameter which affects the velocity and attenuation measurements on sandstones is the effective pressure. The effective pressure, P_{eff}, is defined as the difference between the confining pressure P_c (pressure to which the sample is subjected) and the pore pressure P_p (pressure of the fluid inside the pores), resulting in: $P_{eff} = P_c - P_p$ (Nur and Byerlee, 1971). Best (1994) shows that the P-wave velocity

measured at 0.8 MHz increases with increasing effective pressure for water-saturated sandstones by an order of magnitude, while water-saturated limestones show a negligible pressure dependence (Figure 2.19). Additionally, the clean sandstone has a relatively high Q_P when the effective pressure is increased compared to the corresponding value at the lowest pressure. There is only a slight increase in the quality factors of the other sediments. Best (1994) explains the observed behavior by the presence of non-aligned microcracks occurring at grain contacts in sandstones at shallow depths (or low effective pressures) which are closed at high confining pressures.

Figure 2.20 gives a number of examples of variations of P and S velocities vs. effective pressure for dry and saturated samples at ultrasonic frequencies. In every case, an increase in velocity occurs with increasing effective pressure, but this increase depends on the lithology of each sample (Brulin and Hsieh, 1981). Additional examples of the effect of the effective pressure on the seismic velocity for elastically anisotropic samples is given in Figure 2.21 for different anisotropic materials (Jones, 1983 and Tosaya, 1982). In this case the effective pressure generates an additional induced velocity anisotropy because the application of a uniaxial stress partly closes the cracks (those perpendicular to the stress direction) and the velocity rises substantially.

As in the case of velocities, the attenuation is affected by the effective pressure as observed in Figure 2.22. A decrease in attenuation is normally observed with increasing pressure for P and S waves (Johnston and Töksoz, 1980). Also, as for velocity, the behavior of attenuation as a function of pressure depends greatly on the presence of microcracks, as shown in Figure 2.23 for two Fontainebleau sandstones at different water saturations (Bourbié and Zinszner, 1985). The sandstone without grain contacts (PAV) is unaffected by the uniaxial stress, and its attenuation is very slight. In contrast, the sandstone with grain contacts and very high attenuation (Z 220) is very sensitive to the uniaxial stress (Bourbié and Zinszner, 1985).

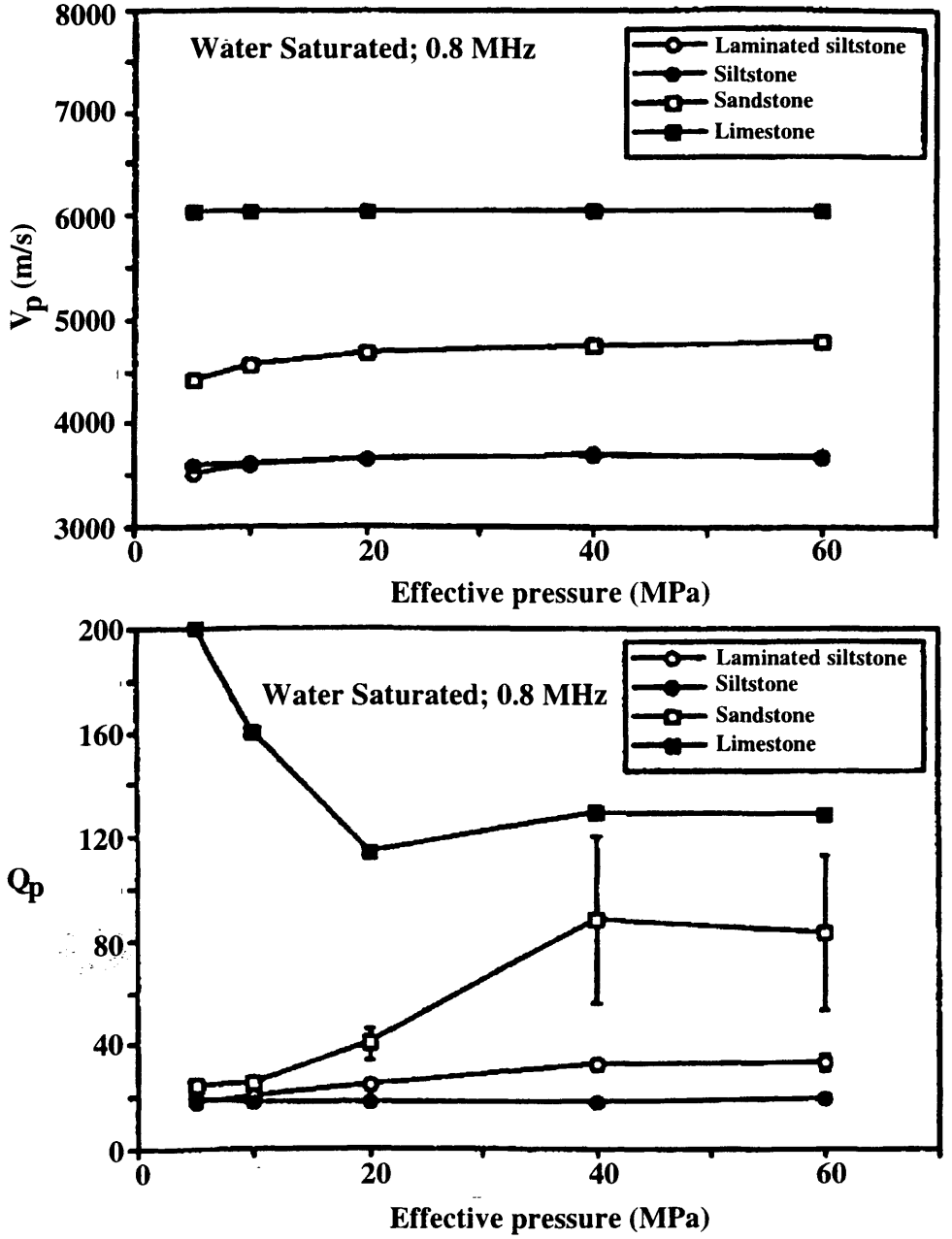

Fig. 2.19 The effect of pressure on seismic velocity and attenuation for P waves considering different lithologies (after Best, 1994).

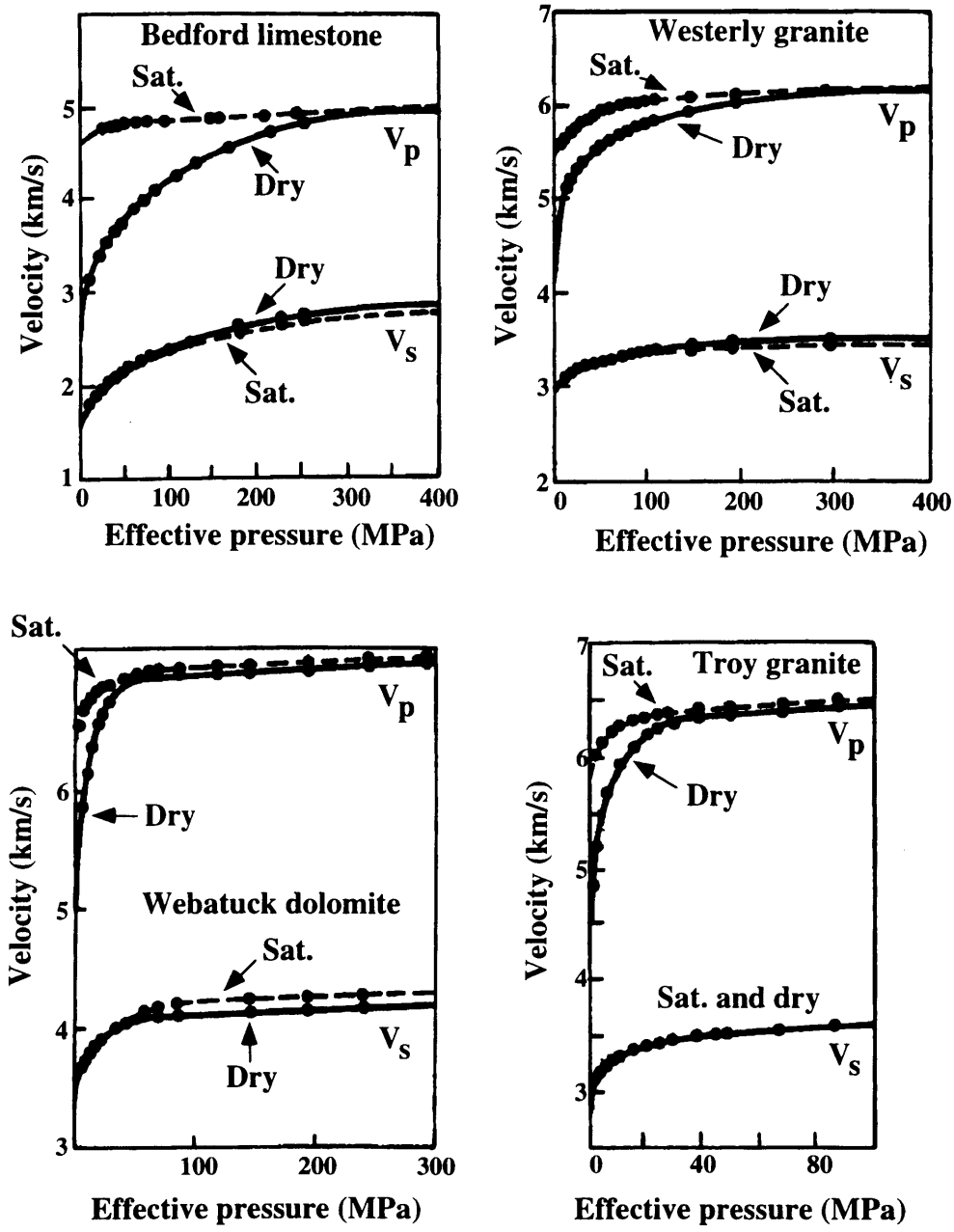

Fig. 2.20 Influence of effective pressure on microcracked rocks using ultrasonic measurements (edited by Brulin and Hsieh, 1981).

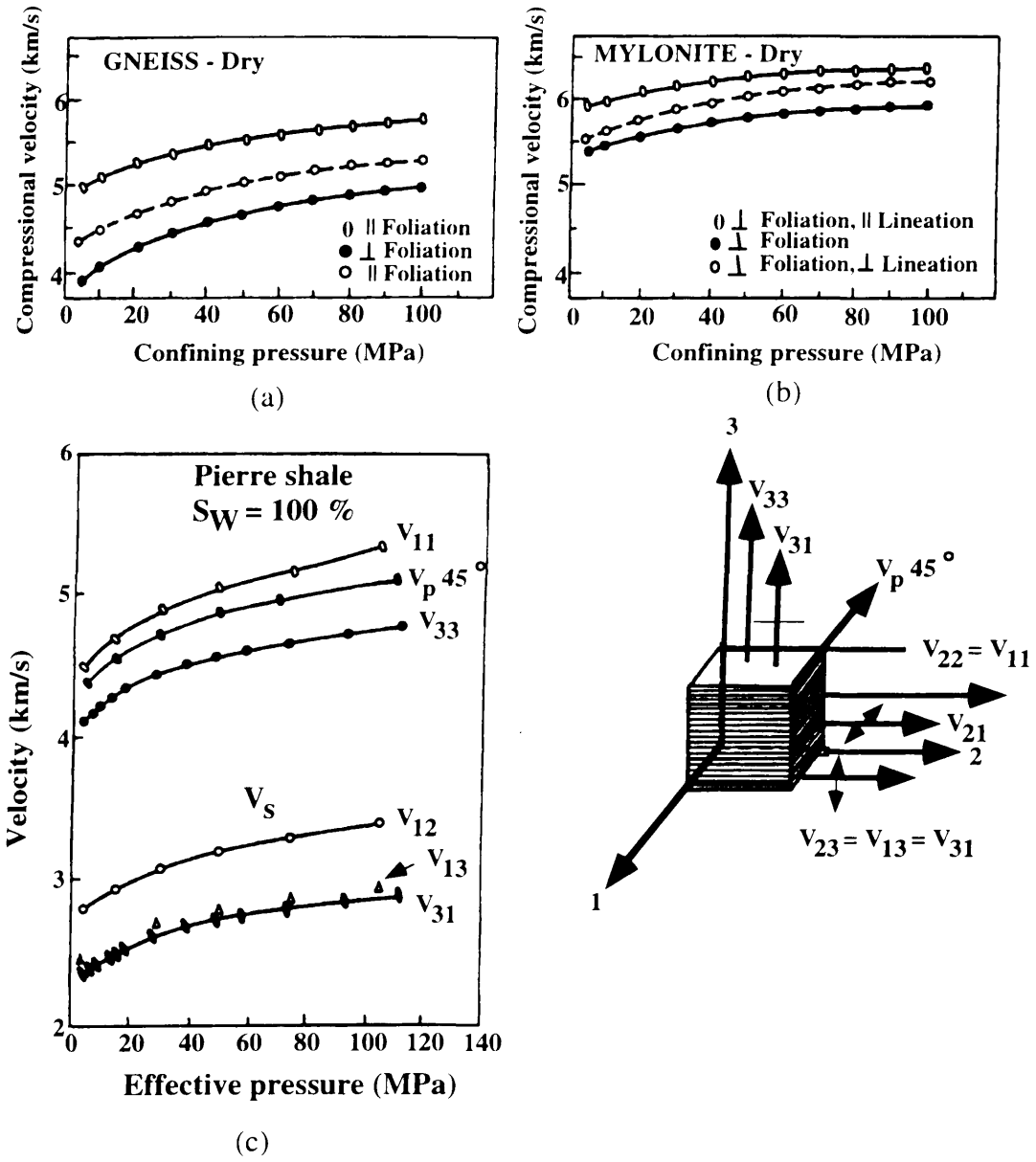

Fig. 2.21 Effect of effective pressure on different anisotropic materials (after Jones, 1983 and Tosaya, 1982).

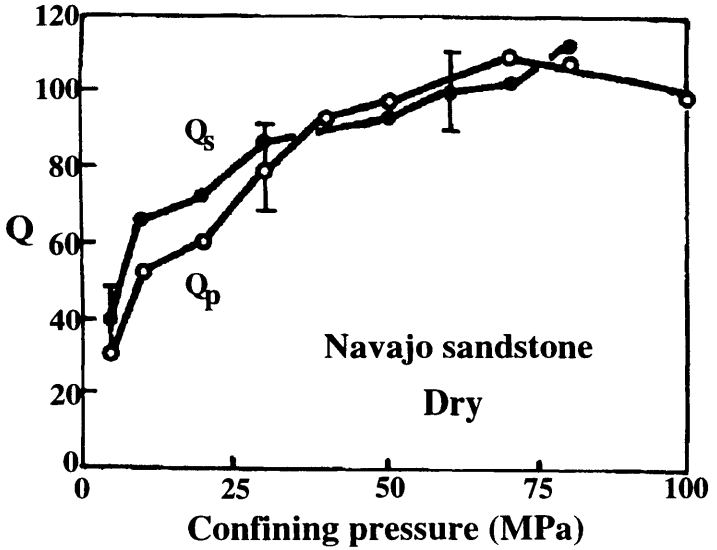

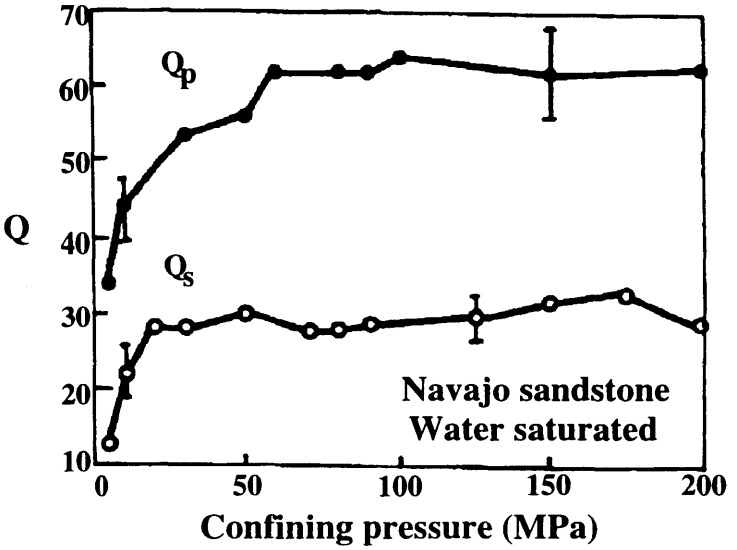

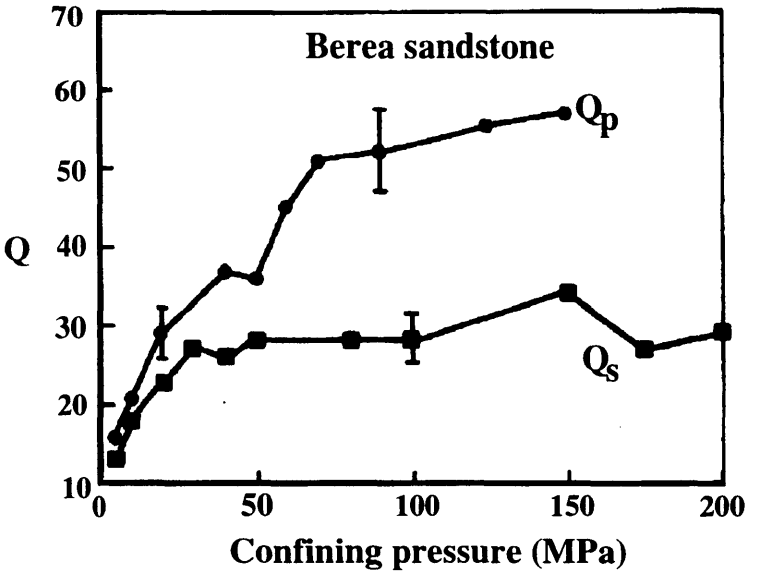

Fig. 2.22 Influence of confining pressure on quality factor. (a) and (b) Ultrasonic measurements from Navajo sandstone. (c) Ultrasonic measurements from Berea sandstone (after Johnston and Töksoz, 1980).

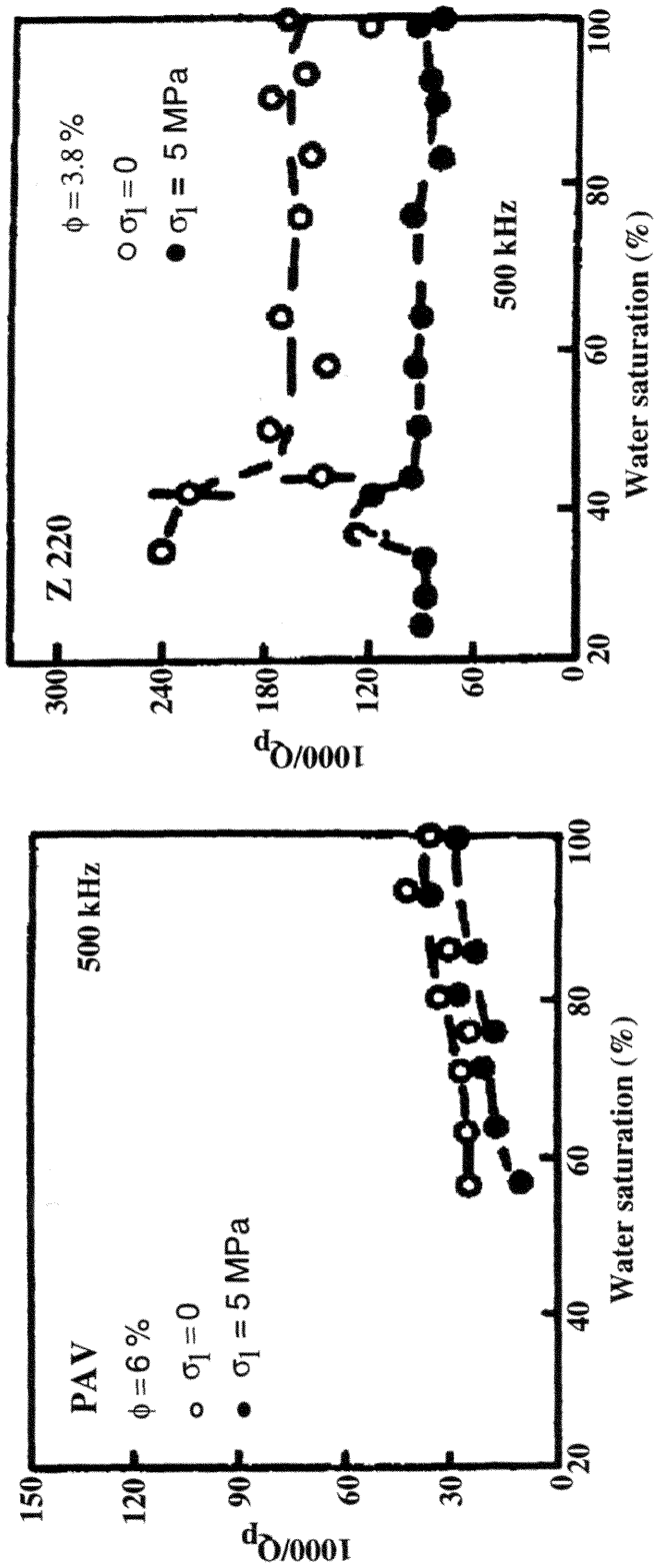

Fig. 2.23 Influence of microcracks on attenuation in Fontainebleau sandstone (after Bourbie and Zinszner, 1985)

The effect of the water saturation on the P- and S-wave velocities is indicated in Figure 2.24. For P waves at partial saturation, the velocity is lower than the "dry" velocity and also lower than the velocity at 100 % saturation. In contrast, for S waves, changes in the velocity behavior between partial and fully saturated cases are not observed (Nur *et al.*, 1980). The only effect due to the introduction of water into the sample is a density increment leading to a decrement in P-wave velocity. By contrast, when complete saturation is reached, the pores become more difficult to compress, increasing the P-wave velocity. For S waves, the effect observed on S-wave velocity is exclusively a density effect which not depends on the degree of saturation (Nur *et al.*, 1980).

Mavko and Mukerji (1992) show that P and S velocities and its corresponding velocity anisotropies may or may not change between dry and saturated conditions for anisotropic rocks (in velocity) with cracks. They conclude that the fluid saturation sometimes increases anisotropy and sometimes decreases it, depending on the rock, the stress state, and the frequency; additionally, saturation effects are sensitive to the distribution of crack orientations and velocities and velocity anisotropy can change dramatically with frequency (Mavko and Mukerji, 1992).

The attenuation of P and S waves is slight for dry rocks, high for partially saturated rocks and intermediate in saturated rocks (Winkler and Nur, 1979). The quality factor Q_S appears always to be lower than Q_P at 100 % saturation for the Massillon sandstone (Figure 2.25).

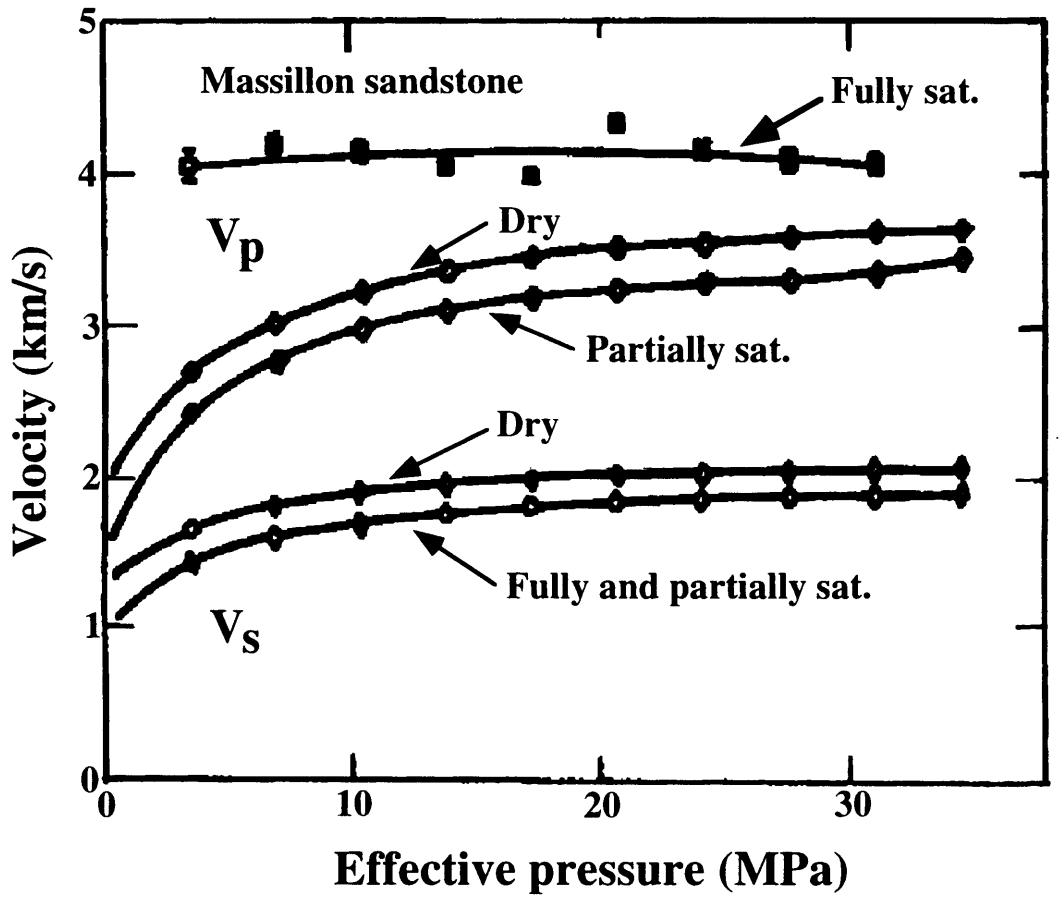

Fig. 2.24 Effect of the water saturation on the *P* - and *S* -wave velocities. Velocity-water saturation relationship in Massillon sandstone versus confining pressure (resonant bar) (after Nur *et al.*, 1980).

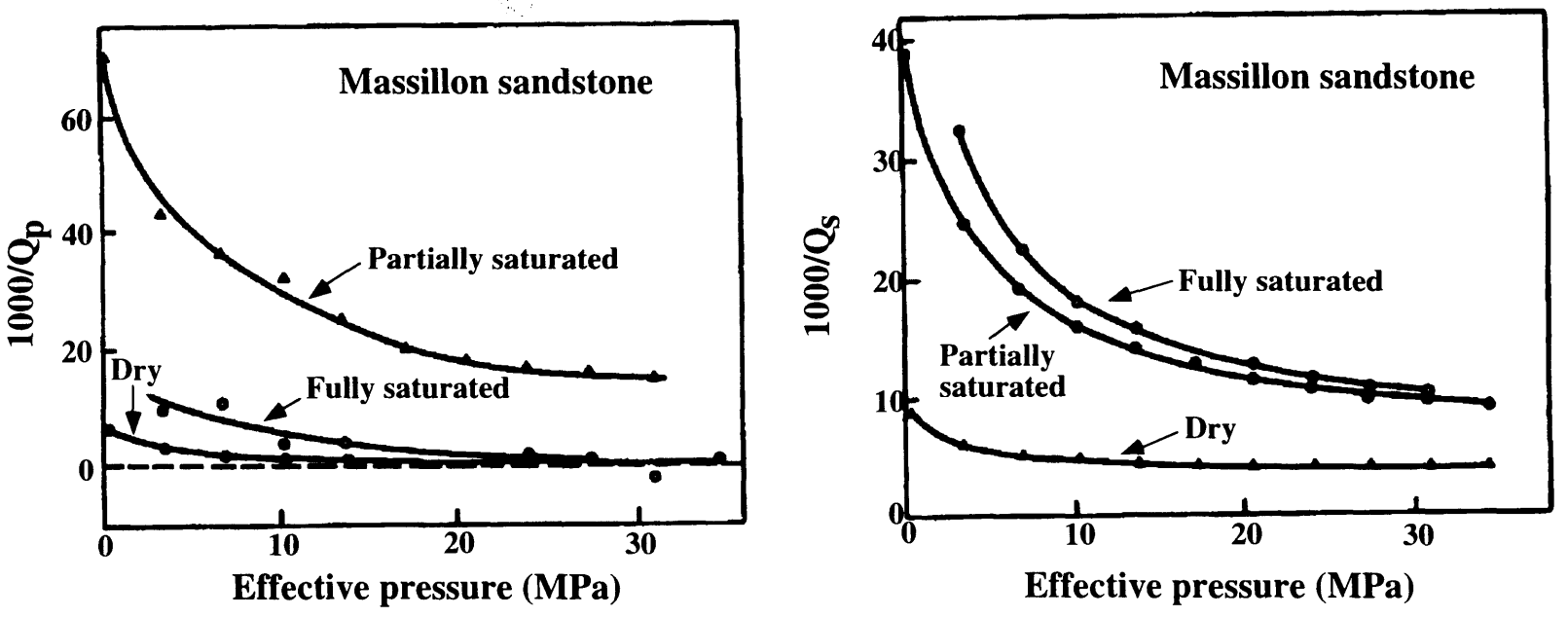

Fig. 2.25 Influence of saturation on attenuation. *P* - and *S* -wave attenuation-water saturation relationship as a function of effective pressure. Ultrasonic measurements on Massillon sandstone (resonant bar) (after Winkler and Nur, 1979).

CHAPTER 3

Regional Geologic Framework

3.1 Location of the study area

The study area is located in the Writing-on-Stone Provincial Park (WOSPP), southern Alberta, about 9 km north of the international border between Canada and the United States of America, Sections 23, 25-26, 35-36, Twp1-Rge 13-W4 and the adjacent area east of the Park, Section 31, Twp1-Rge 12-W4 (topographic sheet No. 72 E/4) as indicated in Figure 1.4.

3.2 Motivation of this study

The rocks that are the subject of this study are sandstones from The Milk River Formation, of commercial importance as a gas-producing interval at shallow depths about 150 - 200 km north of the study area in the subsurface of southeastern Alberta (Myhr and Meijer-Drees, 1976). The reservoir rocks of the "Southern Alberta Milk River Gas Pool" or Medicine Hat Field are estimated by the Energy Resources Conservation Board (ERCB, 1992) to contain 224.29 billion m^3 (7961 Bcf) of gas in place and an undiscovered potential of 57.98 billion m^3 (2058 Bcf). In north-central Montana, several gas fields produce from the equivalent Eagle (sandstone) Formation in the area of the Bearpaw Mountains (Rice, 1980).

The freshwater-saturated sandstones of this formation, south and updip from the gas pool, have long ago been recognized as one of the most important aquifers in Alberta (Dowling, 1916; Meyboom, 1960). Additionally, the Milk River valley and its tributaries in the study area are considered to be the type area for the Milk River Formation even though the lower boundary of the Formation is not exposed there (Tovell, 1956; Meijer-Drees and Myhr, 1981).

The plugs used in this study for measuring P- and S-wave ultrasonic velocity and attenuation values, in dry and water-saturated conditions at atmospheric and high pressure, were selected in such way to have a wide permeability range. These plugs are

sandstones collected to define a large-scale framework for a reservoir-type model in the study area (Meyer, 1994). To derive such a model, extensive permeability analyses have been done on these plugs obtained from the outcrops and the cores recovered in four wells drilled in the immediate vicinity of the north margin of the Milk River valley in WOSPP (Meyer, 1994). The possibility of relating velocity and attenuation measurements of P- and S-waves on these plug samples with the corresponding values of permeability, represents the most important motivation for the present study. In addition, available values of porosity and petrographic information for the selected plug samples can be compared with the measured seismic properties and the relationships interpreted from these comparisons.

The results obtained from the present study are also expected to yield useful information which, when integrated with the permeability distribution model, petrographic analysis, and capillary pressure data being analyzed by Meyer (1994), will permit us to obtain a useful analog for the analysis of actual subsurface reservoirs.

3.3 Geologic background

The study area is located on the western margin of the Alberta Foreland Basin, in itself a sub-basin that was part of the western interior sea extending across to the Canadian Shield during most of the Late Cretaceous (William and Stelck, 1974). The regional sedimentation patterns during this time were strongly influenced by the rising Canadian Cordillera to the west, subsiding and filling the basin as displaced or allochthonous terrains were thrust onto the margin of the North American craton (Price, 1973; Eisbacher *et al*, 1974; Monger and Price, 1979; Beaumont, 1981; Cant and Stockmal, 1989; Meyer, 1994).

The stratigraphic nomenclature applicable in the study area (WOSPP) is shown in Figure 3.1 (after Meijer-Drees and Myhr, 1981). The Milk River Formation is formally subdivided into three members (Tovell, 1956; Meijer-Drees and Myhr, 1981; Meijer-Drees, 1990) as follows:

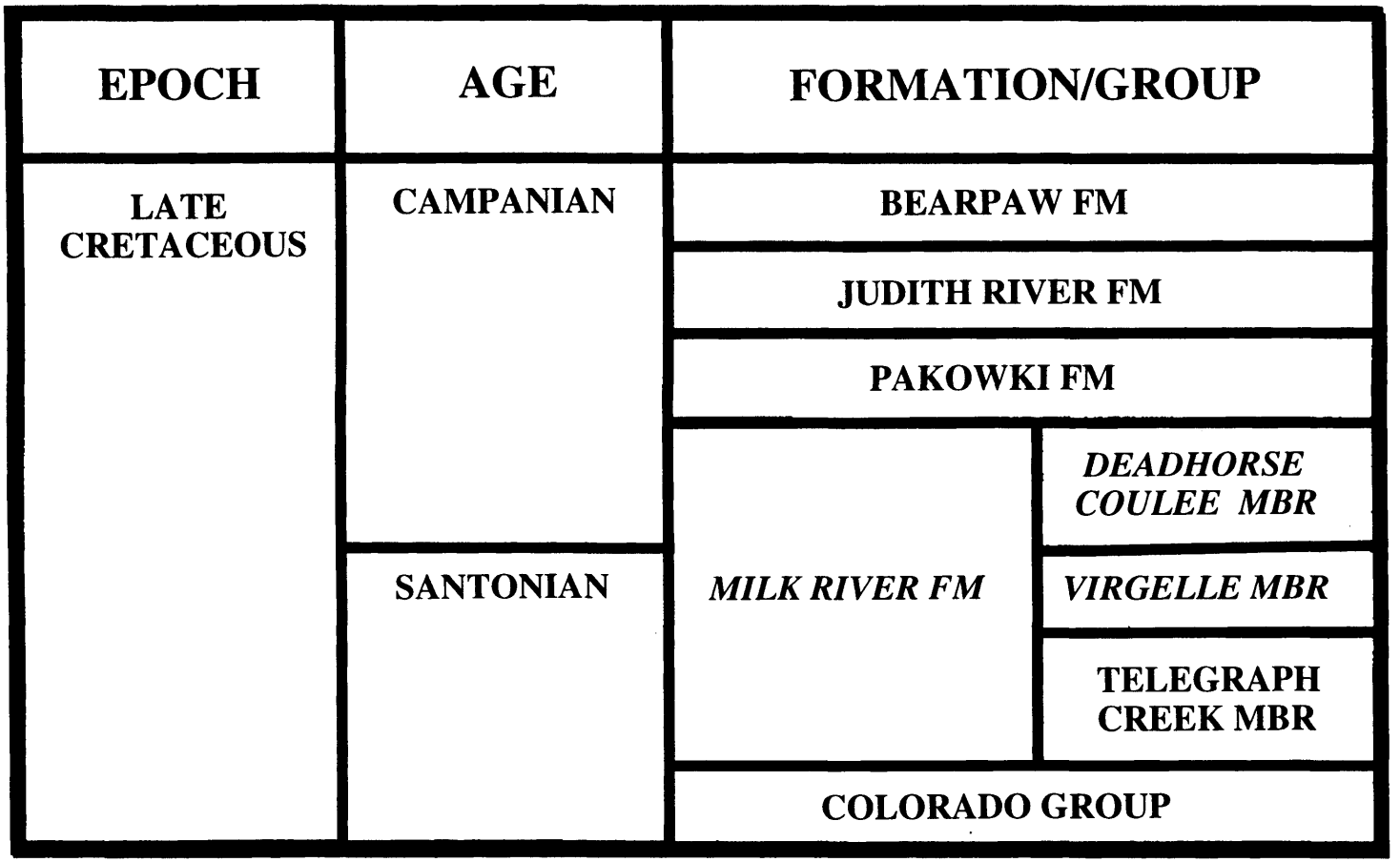

Fig. 3.1 Stratigraphic nomenclature applicable in the area of Writing-on-Stone Provincial Park (WOSPP) (modified after Meijer-Drees and Mhyr, 1981).

(1) the basal Telegraph Creek Member, consisting of interbedded buff or grey shale and sandstone in transitional contact with the underlying dark grey shale of the Colorado Group;

(2) the Virgelle Member, described as a light-coloured, fine- to medium-grained sandstone, conformably overlying the Telegraph Creek Member and, equivalent to- and in mappable continuity with the Virgelle Member at the base of the Eagle (sandstone) Formation of the Montana Group in Montana (Bowen, 1915);

(3) the upper Deadhorse Coulee Member, which appears as a unit of interbedded grey-brown-purple mudstones and light-brown, fine-grained sandstones, unconformably overlying the uppermost, massively weathered Virgelle sandstone ledges. The top is marked by a thin, sideritic sandstone bed containing abundant grey-black polished chert pebbles, in sharp contact with the dark mudstones of the overlying Pakowki Formation (Dowling, 1916).

Figure 3.2 shows a regional isopach map of the Milk River Formation with a maximum thickness of nearly 150 m (500 ft) decreasing to a low of about 90 m (300 ft) toward the north end of the map area (after Tovell, 1956). Just north and west of WOSPP the overall NW-trending contours are modified by a prominent NE-trending high of around 8 m (25 ft). The NNW-trending limit of the non-marine Deadhorse Coulee Member postulated by Tovell (1956) corresponds to the depositional limit of Virgelle Member sandstone defined as a facies change to sandy shale by Meijer-Drees and Myhr (1981); this trend has also been interpreted as parallelling the orientation of the paleoshoreline during accumulation of the Milk River Formation (Leckie and Rosenthal, 1986; Cheel and Leckie, 1990).

3.4 Sedimentology and depositional models

Myhr and Meijer-Drees (1976) and Meijer-Drees and Mhyr (1981) subdivide the Virgelle Member into: a lower unit, a prominent rusty-brown well-sorted, fine- to medium-grained, parallel-laminated or cross-bedded sandstone; and an upper unit of light-grey, friable (and therefore more recessively weathered), cross-bedded sandstone,

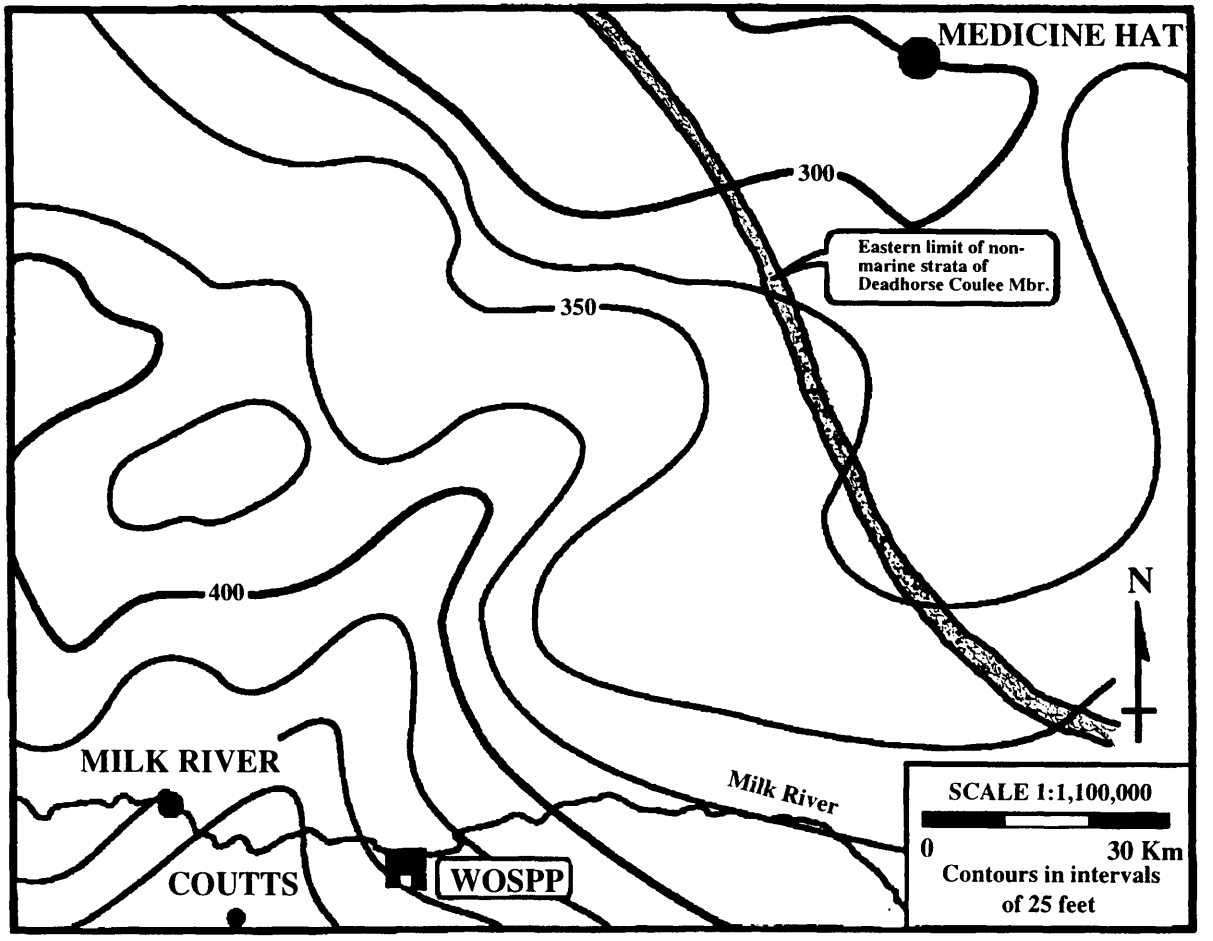

Fig. 3.2 Regional isopach map of the Milk River Formation covering the area between the outcrops at WOSPP and the southern limit of the Southern Alberta Gas Pool near Medicine Hat (after Tovell, 1956; also Meyer, 1994).

commonly containing siderite pebbles and mudstone clasts, overlying the former with an erosional contact.

Leckie and Rosenthal (1986) and Cheel and Leckie (1990) interpreted the depositional environment at WOSPP as a tidal-inlet complex, flood-, ebb- or mixed-flow-dominated with various associated sedimentary structures thought to arise from tidal processes (shale/sandstone couplets and tidal bundles, flood ramps, reactivation surfaces). The apparent lack of lagoonal muds and other back-barrier deposits is ascribed to a rapid rate of lateral migration of the paleo-inlet relative to progradation of the shoreline.

Meyer (1994) proposes a tentative depositional model for the interval between the Virgelle and basal Deadhorse Coulee Members. Overall, the depositional system is clearly progradational as evidenced by a regionally significant sequence from marine offshore through the entire shoreface, topped by thick intervals of terrestrial, supratidal, muddy paleosols (Figure 3.3).

The lower and middle shoreface intervals of this depositional system are clearly storm-dominated but the "classic", marine upper shoreface-foreshore succession is hardly present. It is replaced instead by a regional, bathymetrically equivalent, subtidal to intertidal flat, characterized by a bidirectional, east-west oriented current pattern. This pattern and the southward thickening of the tidal flat succession (sand flats of a broad, tide-dominated estuary) are interpreted to indicate that the study area of WOSPP is not precisely in the center of the estuary, but along and edge, possibly closer to the northern margin (Meyer, 1994).

3.5 Lithofacies

The lithofacies corresponding to the sixty sandstone samples used in the present study is based primarily on physical and biogenic sedimentary structures due to the very limited lithologic variety present in the interval. The detailed description of these lithofacies is given as follows by Meyer (1994):

(1) 2HCS: Medium to thickly bedded (≅ 37-90 cm), laminated (≅ 0.5-3 cm), very fine (lower) to fine (upper) grained, light brown-reddish and brown-tan-grey

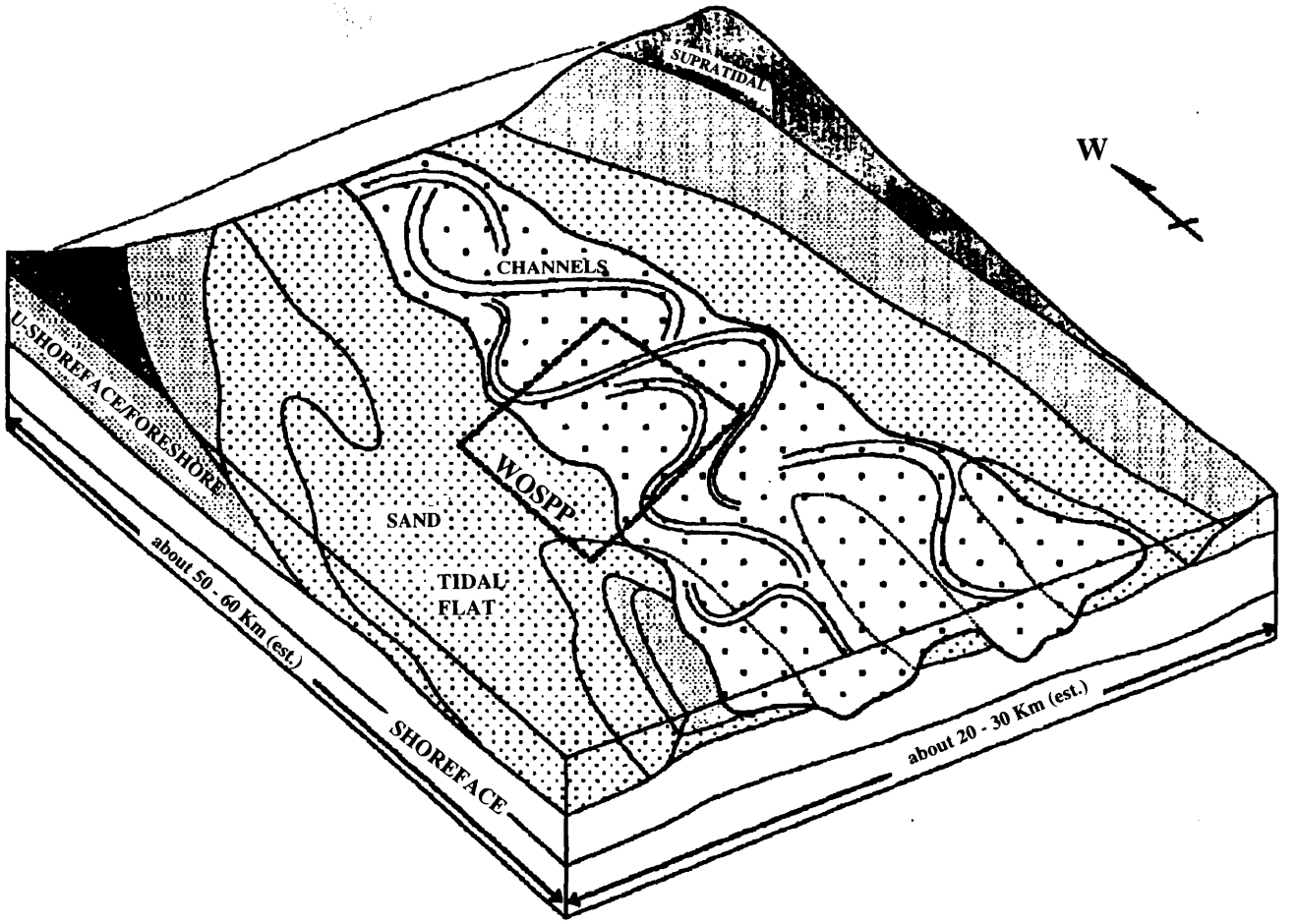

Fig. 3.3 Schematic block diagram of proposed depositional model at WOSPP by Meyer (1994). The scale of the model is only approximate, relative to WOSPP, at the boundaries of the system are outside of the field area (after Meyer, 1994).

sandstones with occasionally slightly asymmetric, hummocky (HCS) and swaley (SCS) cross-bedding and very rare, thin (≤ 3 cm) mudstone interbeds. The lithology and grain size of the facies appears extremely homogeneous over the entire study area. The facies characterizes the lower Virgelle Member and is interpreted as a storm-dominated lower-to-middle shoreface (Meyer, 1994);

(2) 3CBS: White-light grey-tan sandstones forming cross-bedded sets of 10 to 150 cm in thickness. Cross-bedding dips are 15-25 degrees and often marked by alternating carbonaceous-muddy (1-3 mm) and quartzose (5-30 mm) laminae; the former are commonly sideritized. This facies presents three subfacies: tabular (2D) and trough (3D) both associated with channels, and planar/subhorizontal-bound (PL) cross-bedding for tidal and flat. All these lithofacies are represented in Figure 3.4.

LITHOFACIES

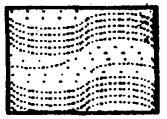

= hummocky and swaley cross-bedded sandstone (2HCS).

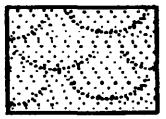

= 3D cross-bedded sandstone (troughs); 3CBS_3D.

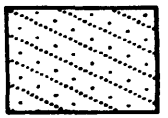

= 2D cross-bedded sandstone (tabular laminae); 3CBS_2D.

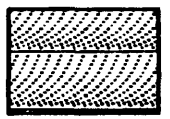

= Planar-bound, herringbone cross-bedded sandstone (3CBS_PL).

Fig. 3.4 Description of lithofacies for sandstones from WOSPP (after Meyer, 1994).

CHAPTER 4

Experimental Methodology and Measurement of phase velocity and attenuation for compressional and shear waves

4.1 Description of the sandstone samples

Sixty cylindrical sandstone samples 3.79 cm in diameter and 2.8 cm to 7.4 cm in length were analyzed in this study. Sample lengths were more than 100 times the average grain size which was estimated around 220-280 μm (personal conversation with Meyer). The top and base of these samples were carefully polished to within an uncertainty of ± 0.05 cm. These samples come from well cores and outcrops in the Writing-on-Stone Provincial Park (WOSPP), Alberta, (Canada).

The petrophysical analysis on these sandstones, including clay content and porosity, were performed by Core Laboratories in Calgary (Canada). The clay content analysis was only done for eight sandstone samples defined as control samples, representing the different lithofacies observed in the area, indicating that these samples present clay content values by volume fraction between 6% and 13%. The porosity values of these sandstone samples are between 20.6% and 32%. The sandstone samples with clay contents between 6% and 13% come from the lower unit of the Milk River Formation in WOSSP and those presenting clay contents between 10% and 13% come from the upper unit of the same formation. The sandstones from the lower and upper units of the Milk River Formation will be named LU and UU sandstones, respectively.

The sandstone samples were oriented along three orthogonal directions named X, Y and Z (Figure 1.1). Both X and Y directions, 90° apart, define the plane parallel to the layering of the samples while the Z direction is perpendicular to this plane. Each X, Y and Z directions has associated twenty sandstone samples (Table 1).

In general, the P-wave phase velocity and permeability values associated with the Z direction are lower than the P-wave phase velocity and permeability values corresponding to both X and Y directions indicating a symmetry like TI as shown in

Figures 1.1 and 2.5. The permeability values for these samples were measured at the University of Calgary by Meyer (Ph.D. thesis in preparation) and are shown in Table 1. In general, LU sandstones show lower permeabilities than UU sandstones show (Table 1).

The degree of permeability anisotropy for both LU and UU sandstones are between 0.2 and 1.16. Here, the degree of permeability anisotropy is defined as the ratio between the measured permeability parallel to the vertical direction, divided by the permeability measured perpendicular to this direction (Ehlig-Economides *et al.*, 1990). A medium presenting isotropic permeability is represented by a ratio of 1.0 using this definition of degree of permeability anisotropy.

4.2 Experimental relationships between clay content, permeability and porosity

4.2.1 Permeability-porosity relationship

Figure 4.1a shows the permeability-porosity relationship for the sandstone samples oriented along the Z direction. Although the range of porosities is very limited which could create a misleading conclusion, it is evident that two different trends exist: for LU sandstones the permeability-porosity relationship is linear on a semilog plot as expected from statistical analysis of well log information (Allen, 1979; Wendt *et al.*, 1986); in contrast, for UU sandstones permeability apparently does not shows a significant dependence on porosity within the porosity range considered.

A linear least-squares fit was applied to the permeability-porosity values for LU sandstones gives a correlation factor of 0.83 (Figure 4.1a). Similar permeability-porosity relationships were observed for LU and UU sandstones along both X and Y directions (Figures 4.1b,c). In the case of the LU sandstones the corresponding linear least-squares fits on its measured permeability-porosity values along X and Y directions show correlation factors of 0.94 and 0.93, respectively.

4.2.2 Porosity-clay content relationship

Figure 4.2 shows the porosity-clay content relationship for both LU and UU sandstones corresponding to the eight control sandstone samples (section 4.1). It is

TABLE 1

Petrophysical parameters for sandstone samples from WOSPP

SAMPLE	No.	ϕ (%)	k (mD)	C (%)	D (%)	Unit	Facies	length (cm) (**)
W7-13V	1Z1	26.2	525± 21	6 (*)	4 (*)	UU	3CBS-2D/PL	6.48
W7-25HPE	2X1	27.0	915± 62	-	-	UU	" "	4.49
W7-26HPA	3Y1	27.7	1094± 76	-	-	UU	" "	3.72
W7-4V	4Z2	30.8	1579± 97	-	-	UU	3CBS-3D/2D	6.35
W7-9HPE	5Y2	29.7	1354± 98	-	-	UU	" "	4.14
W7-8HPA	6X2	30.8	1544±140	-	-	UU	" "	3.65
W7-63V	7Z3	27.9	86± 3	-	-	LU	2HCS-BUR	6.58
W7-125HPE	8Y3	29.3	159± 5	-	-	LU	" "	3.88
W7-124HPA	9X3	29.6	218± 8	-	-	LU	" "	3.29
W7-91V	10Z4	25.5	20± 1	-	-	LU	2HCS	5.92
W7-178HPA	11X4	25.1	83± 3	-	-	LU	" "	3.63
W7-179HPE	12Y4	25.7	78± 3	-	-	LU	" "	3.93
W7-68V	13Z5	29.3	125± 4	13 (*)	8 (*)	LU	2HCS-BUR	5.94
W7-134HPA	14X5	29.5	202± 7	-	-	LU	" "	3.51
W7-135HPE	15Y5	29.1	194± 7	-	-	LU	" "	3.95
W7-22V	16Z6	27.8	676± 30	10 (*)	21 (*)	LU	2HCS	6.51
W7-51HPE	17Y6	28.5	765± 38	-	-	LU	" "	4.44
W7-50HPA	18X6	27.6	721± 39	-	-	LU	" "	3.59
W7-28V	19Z7	28.2	832± 37	-	-	LU	2HCS	6.56
W7-62HPA	20X7	27.9	784± 44	-	-	LU	" "	3.83
W7-63HPE	21Y7	28.9	868± 48	-	-	LU	" "	4.18
W7-7V	22Z8	28.8	960± 59	-	-	UU	3CBS-2D/PL	6.64
W7-15HPE	23Y8	29.0	1322± 93	-	-	UU	" "	4.44
W7-16HPA	24X8	29.2	1180± 85	12 (*)	1 (*)	UU	" "	3.70
W7-87V	25Z9	25.8	82± 3	-	-	LU	2HCS	6.87
W7-172HPA	26X9	26.8	103± 4	-	-	LU	" "	4.00
W7-171HPE	27Y9	26.3	98± 3	-	-	LU	" "	4.34
263V	28Z10	30.4	335± 11	11 (*)	15 (*)	LU	2HCS-LAM	7.51
263HPA	29X10	30.0	502± 19	-	-	LU	" "	7.51
263HPE	30Y10	30.2	471± 18	-	-	LU	" "	7.35
275V	31Z11	20.1	12± 0.7	7 (*)	8 (*)	LU	2HCS-BIOT. SID./CEM.	6.03
275HPA	32X11	20.4	20± 1	-	-	LU	" "	7.44
275HPE	33Y11	20.7	17± 1	-	-	LU	" "	6.70
285V	34Z12	28.8	451± 21	-	-	UU	3CBS-2D LAM.	3.21

(**) This lenght must be multiplied by a factor of 100 for obtaining the scaled velocity.

285HPA	35X12	30.7	1105± 59	-	-	UU	" "	5.86
285HPE	36Y12	30.1	980± 55	-	-	UU	" "	4.84
286V	37Z13	31.1	1481± 127	-	-	UU	3CBS-2D CARB-LAM	3.67
286HPA	38X13	31.7	2242± 203	-	-	UU	" "	5.47
286HPE	39Y13	32.0	2497± 206	-	-	UU	" "	7.33
297V	40Z14	29.8	551± 24	-	-	UU	3CBS-2D CARB-LAM	4.57
297HPA	41X14	31.0	1423± 74	-	-	UU	" "	7.17
297HPE	42Y14	31.1	1117± 57	11 (*)	0 (*)	UU	" "	7.36
W9-201V	43Z15	29.0	1211± 78	-	-	UU	3CBS-2D/3D	4.75
W9-136HPE	44Y15	29.5	1456± 153	-	-	UU	" "	2.75
W9-2HPA	45X15	29.0	1435± 108	-	-	UU	" "	3.45
W9A-112V	46Z16	25.6	1362± 92	-	-	UU	3CBS-2D/3D	4.70
W9A-22HPA	47X17	25.4	1932± 221	-	-	UU	" "	3.40
W9A-64HPE	48Y17	25.1	1396± 137	-	-	UU	" "	2.80
W9A-114V	49Z18	28.6	1557± 120	-	-	UU	3CBS-2D/3D	4.50
W9A-29HPA	50X18	28.6	1817± 194	13 (*)	14 (*)	UU	" "	3.20
W9A-67HPE	51Y18	28.7	1438± 139	-	-	UU	" "	3.05
1206V	52Z19	28.1	1487± 93	-	-	UU	3CBS-PL	5.45
1206HPA	53X19	28.1	1636± 87	-	-	UU	" "	7.40
1206HPE	54Y19	28.1	1403± 81	-	-	UU	" "	5.00
W7-89V	55Z20	26.6	64± 2	-	-	LU	2HCS	5.85
W7-174HPA	56X20	26.4	107± 4	-	-	LU	" "	3.75
W7-173HPE	57Y20	26.4	97± 3	-	-	LU	" "	4.65
W9-294V	58Z21	28.3	93± 3	-	-	LU	2HCS	6.95
W9-177HPE	59Y21	28.2	121± 4	-	-	LU	" "	3.55
W9-104HPA	60X21	28.2	131± 5	-	-	LU	" "	3.75

(*) Control sandstone samples.

The symbol "C" represents the clay content value and the symbol "D" indicates the dolomite content value. Both parameters are measured in percent by weight. The porosity value, ϕ is measured in percent and the permeability, k is measured in millidarcies. The porosity error is 0.5%.

NOMENCLATURE

LU = Sandstone sample from the lower unit of the Virgelle Member (Milk River Formation).
UU = Sandstone sample from the upper unit of the Virgelle Member (Milk River Formation).

The first column shows the label of the sample in the field as defined by Meyer (1994). The second column shows the label used in the laboratory. The first digit is the position of the sample in the sequence, the letter (X, Y or Z) is the orientation of the sample, and the last digit is the group to which the sample belongs (same number indicates that it belongs to the same group).

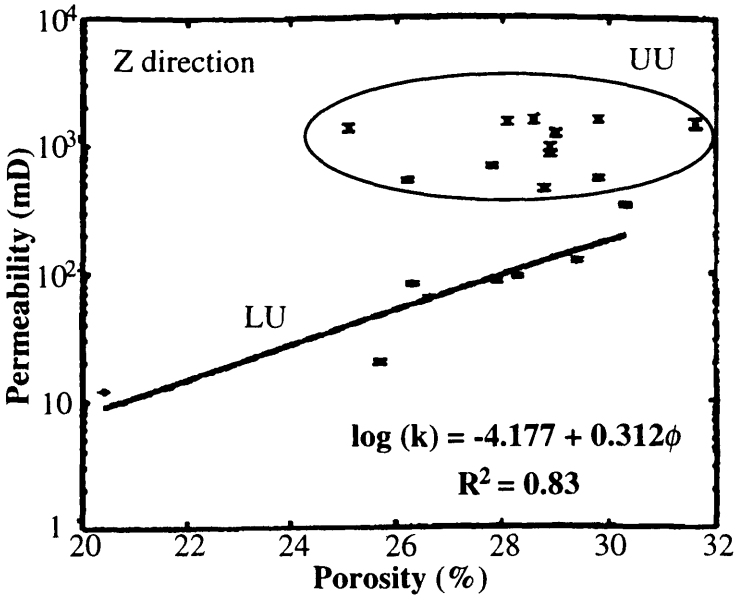

(a)

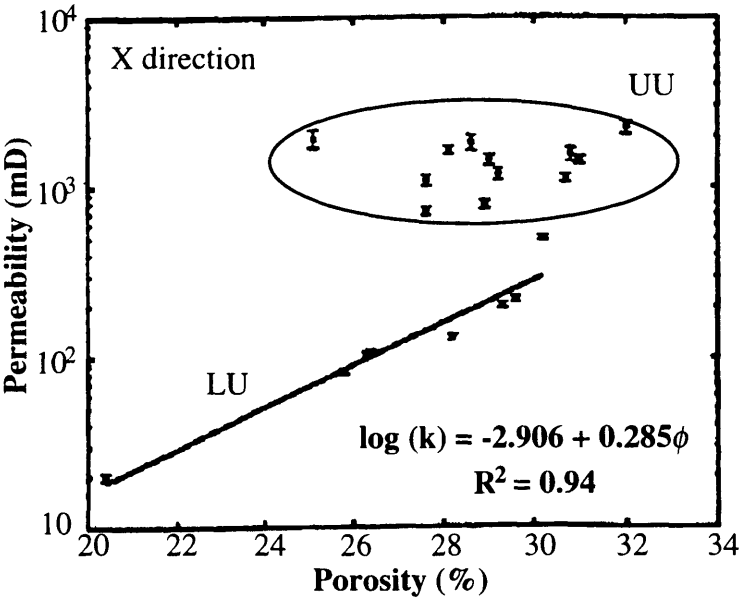

(b)

Fig. 4.1 Permeability-porosity relationship for LU and UU sandstones: (a) along Z direction (perpendicular to the layering); (b) along X direction (parallel to the layering). A linear least-squares fit of the permeability-porosity values for LU sandstones is presented. The symbol R^2 represents the correlation factor. The error bars for permeability are indicated. All the measurements under water-saturated conditions.

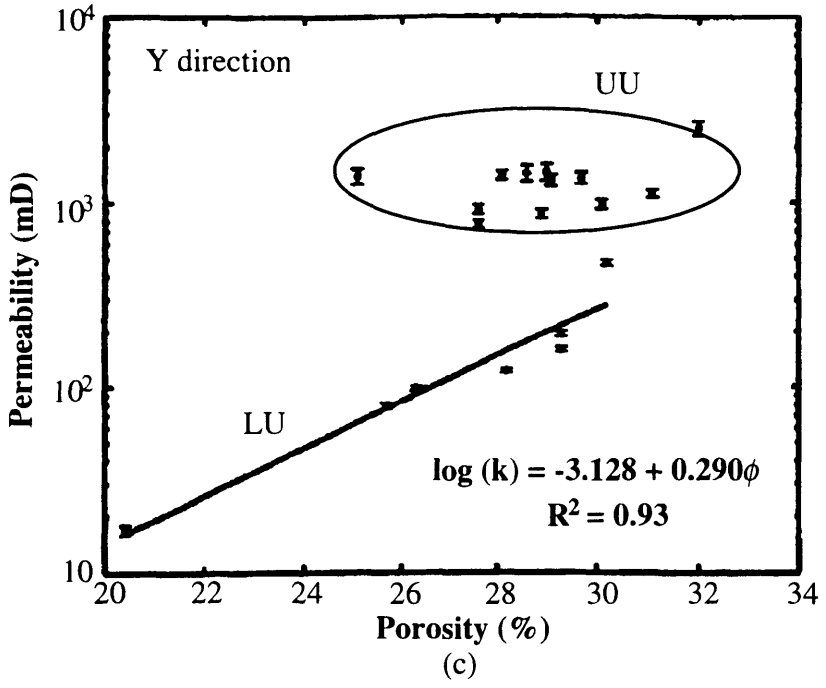

(c)

Fig. 4.1 (c) Permeability-porosity relationship for LU and UU sandstones along Ydirection (parallel to the layering). A linear least-squares fit of the permeability-porosity values for LU sandstones is presented. The symbol R^2 represents the correlation factor. The error bars for permeability are indicated. All the measurements under water-saturated conditions.

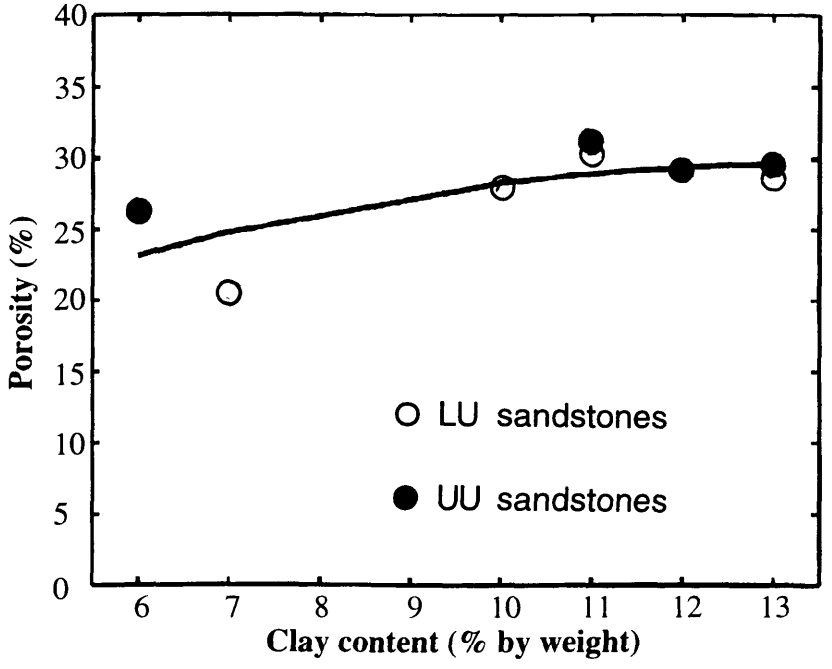

Fig. 4.2 Porosity-clay content relationship observed in the eigth control sandstone samples from WOSPP.

evident that higher clay content values are associated with higher porosity values. The experimental results obtained by Yin and Nur (1994) on unconsolidated synthetic sediments show that the behavior of porosity is strongly affected by the clay content (Figure 4.3b).

Yin and Nur (1994) show that from sand to shaly-sand (Figure 4.3a), clay particles fill the sand pore space and act to stiffen the matrix. As a result, porosity decreases with increasing clay content between 0-20%. In contrast, from sandy-shale to shale, sand grains are suspended in the clay matrix producing a porosity increment with increasing clay content (Figure 4.3a). Additionally, this behavior of porosity as function of clay content is kept at a range of pressures between 0 to 50MPa. The transition of petrophysical properties from shaly-sand to sandy-shale is clearly indicated by the critical clay-content value as indicated in Figure 4.3a (Yin and Nur, 1994).

The relationship shown in Figure 4.2 indicate a porosity decrement for clay content values between 6% and 7% followed by a porosity increment with increasing clay content beyond 10%. Although the data indicated in Figure 4.2 is very limited to do a definitive conclusion, this behavior of porosity as a function of clay content resembles the results indicated in Figure 4.3b. The porosity was estimated with an error of 0.5%.

4.2.3 Permeability-clay content relationship

Yin and Nur (1994) based on their experiments on unconsolidated synthetic sediments show that below the critical clay-content value, permeability logarithmically decreases with increasing clay content, but above the critical clay-content value, permeability changes little with increasing clay content although still varies with confining pressure (Figure 4.4).

The dependence of permeability on clay content for the eight control sandstone samples is shown in Figure 4.5a. The analysis of this limited data indicates that no well-defined relation is observed between permeability and clay content. In fact, the permeability measured along the Z direction show a poorly defined tendency to decrease

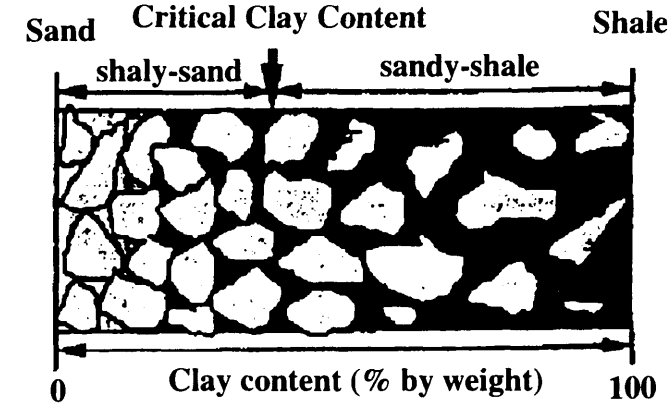

(a)

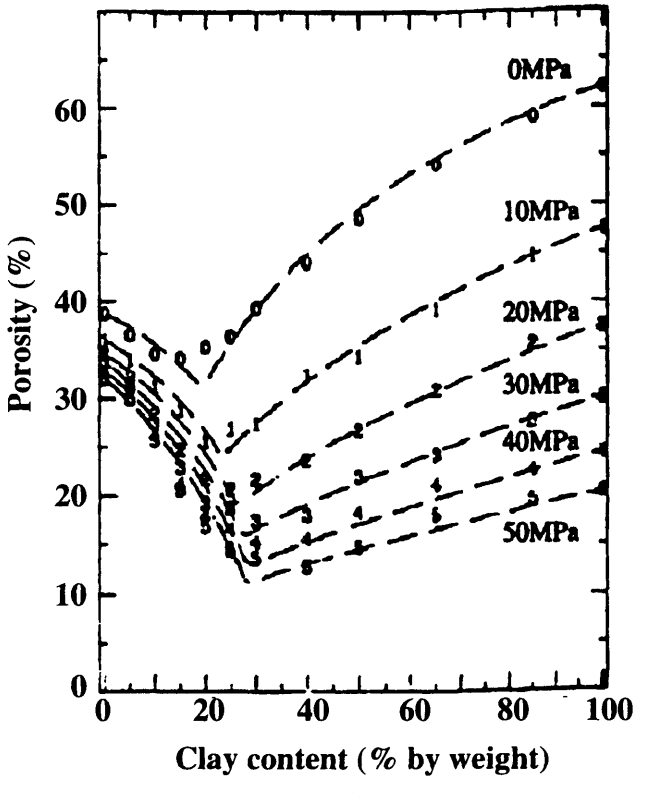

(b)

Fig. 4.3 (a) An illustration of three cases of clay content classification and critical clay content. (b) Porosity as a function of clay content at different confining pressures (after Yin and Nur, 1994).

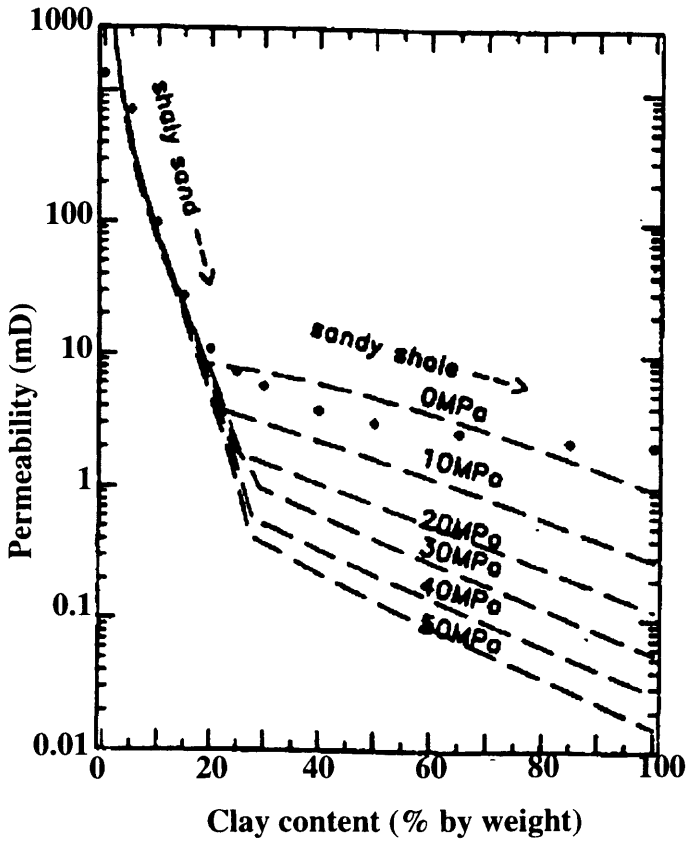

Fig. 4.4 Measured and modeled permeability versus clay content. The measured data are considered to represent zero confining pressure (after Yin and Nur, 1994).

with increasing clay content, but the permeability observed along both X and Y directions increases with increasing clay content (Figure 4.5a). In other words, the experimental permeability-clay content relationship shown in Figure 4.5a does not follow the general behavior described by Yin and Nur (1994).

The behavior of permeability *versus* clay content, indicated by Yin and Nur (1994) for clay contents between 0-20% (Figure 4.4), is better observed in the permeability-dolomite content relationship for control samples (Figure 4.5b). In fact, the permeability decreases with increasing dolomite content between 0% and 10%, but at higher dolomite content values permeability increases indicating that other factor could be controlling the permeability-dolomite relationship at higher dolomite content values.

4.3 Description of the laboratory methodology for estimating phase velocity and attenuation

4.3.1 Identification of P and S waves

The first step before calculating the phase velocities and the attenuation coefficients of the P and S waves is to identify both type of waves in the recorded trace. In physical modeling when piezoelectric transducers are used for generating P and S waves, pure P and S waves are generally not recorded because each P- or S-wave source transducer generates a small amount of energy in both types of waves. Therefore a seismic trace generated and recorded by using P-wave source and P-wave receiver transducers will contain both P and S waves. The same conclusion is valid for a seismic trace obtained using S-wave source and S-wave receiver transducers. As a result, it is necessary to isolate both type of waves from the recorded trace before calculating the phase velocities and the attenuation coefficients of the P and S waves.

The method used in the present study for identifying P and S waves in a recorded trace exploits the fact that each P or S wave is recorded better when both source and receiver transducers have the same polarization as the type of wave of interest. In other words, the recorded P waves are well-defined and present higher amplitudes when they are generated by a P-wave source transducer and when are recorded by a P-wave receiver transducer. The same principle is applied to S waves, but it is necessary to use S-wave

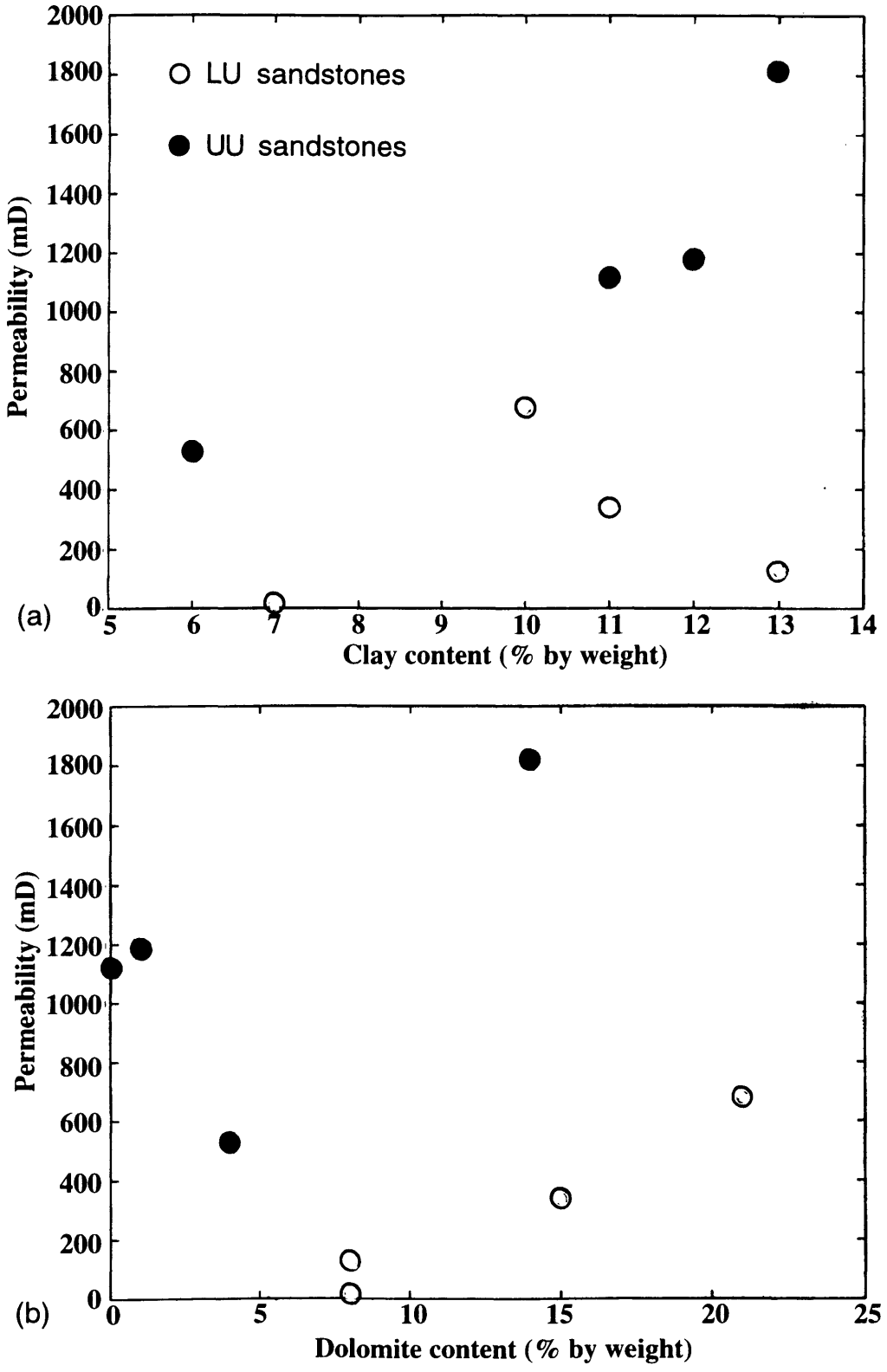

Fig. 4.5 Relationship between permeability and (a) clay content and (b) dolomite content for the eight control sandstone samples.

transducers as source and receiver. A comparison between the recorded trace generated using both P-wave source and receiver transducers and the recorded trace generate using both S-wave source and receiver transducers will help to identify those signals which are enhanced or diminished. The polarization associated with the recorded trace where some signal is enhanced will define the polarization of this particular signal.

This method is valid only for pure P and S waves which excludes converted waves from P to S modes. Additionally, this method is limited by extra arrival interferences, *e.g.*, multiples and back- and side-reflections from the bottom or walls of the sample. This method was applied on recorded traces from sandstone samples under dry and water-saturated conditions.

Figures 4.6 and 4.7 show the application of the above method for identifying P and S waves for two sandstone samples from WOSPP under dry and water-saturated conditions, respectively. It is evident that the P wave presents a low amplitude but the S wave shows a higher amplitude in the S-S data, which allowed me to identify both kind of waves.

4.3.2 Phase velocity estimation

Dellinger (1992) showed that for propagation down symmetry directions group and phase velocity are the same and there is no ambiguity for rock samples, but along non-symmetry directions there is no guarantee that the energy radiated from the source will travel straight up the axis of the shale core to the receiver (Fig. 4.8). Vestrum (1994) reached a similar conclusion working on Phenolic CE which was assumed to have orthorhombic symmetry.

In all the experiments done on the sandstone samples from WOSPP it will be assumed that the measured velocity represents the phase velocity because each sample was oriented parallel and perpendicular to the layering observed on outcrops. Additionally, the measured phase velocity anisotropy reveals a TI symmetry for these samples which indicates that these directions of the samples are very close to the symmetry directions.

Rathore *et al.* (1994) proposed the first-zero-crossover method for estimating the phase velocity for a dispersive and anisotropic medium (Figure 1.5b). These authors based

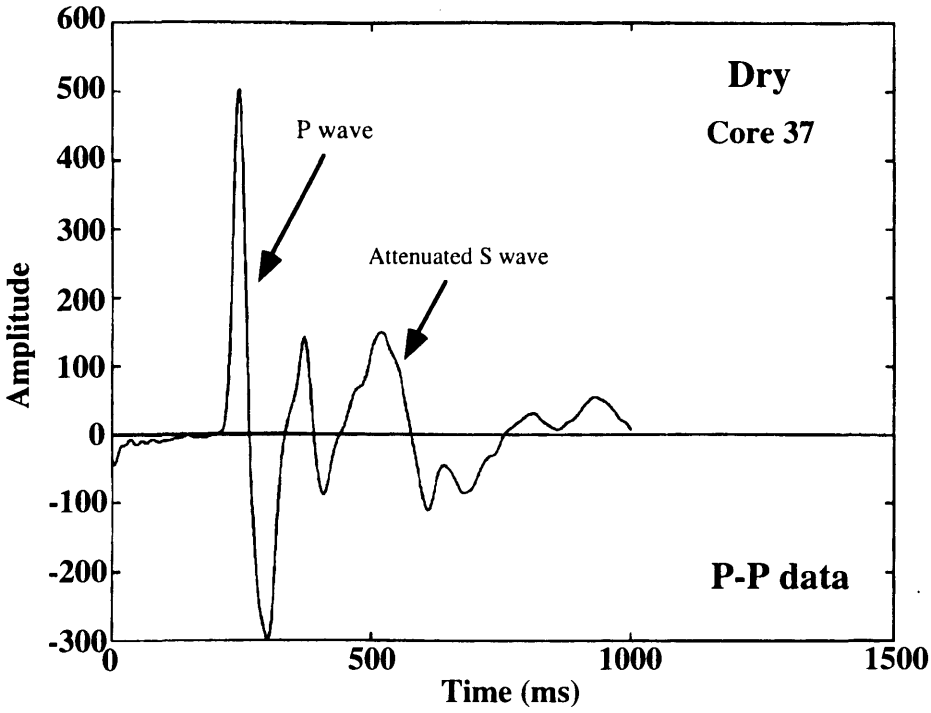

(a)

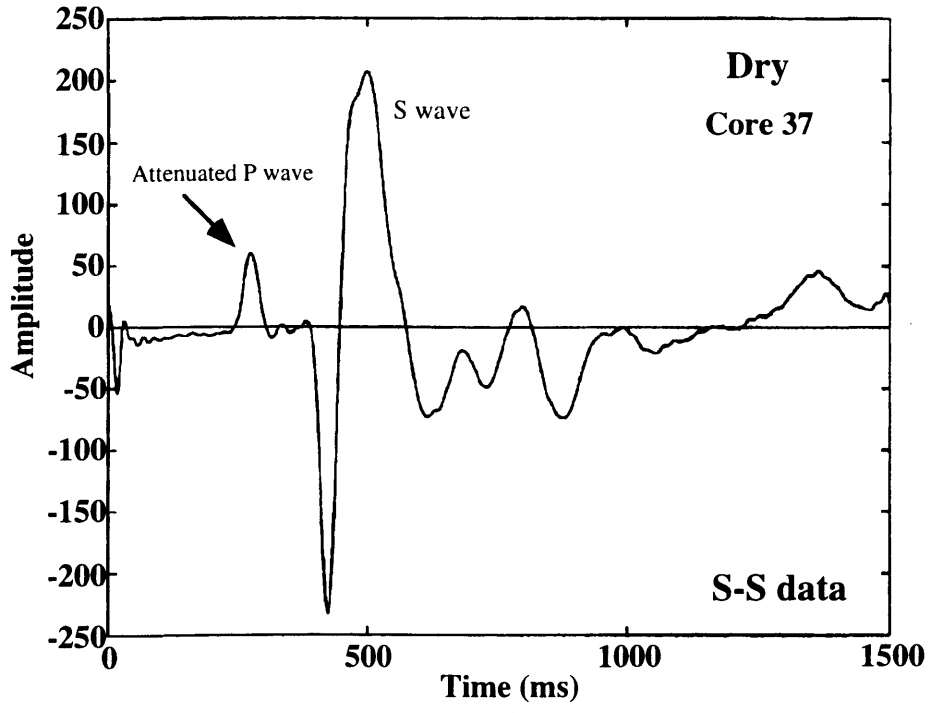

(b)

Fig. 4.6 (a) Recorded trace using P-wave source transducer and P-wave receiver transducer. (b) Recorded trace using S-wave source transducer and S-wave receiver transducer. For S-S data both transducers are polarized in the same direction. Both traces were recorded under dry conditions.

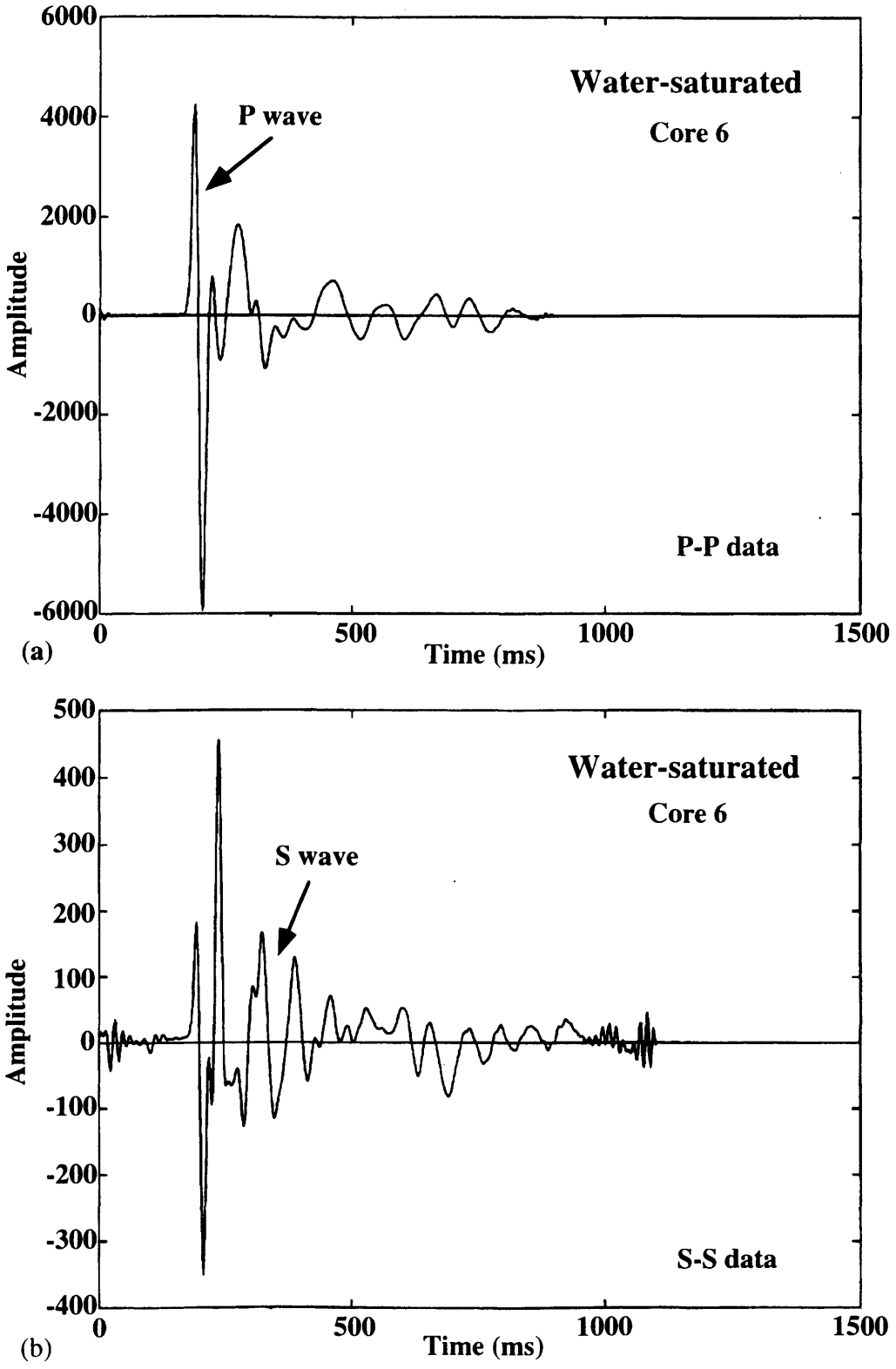

Fig. 4.7 (a) Recorded trace using P-wave source and receiver transducers. (b) Recorded trace using S-wave source and receiver transducers. For S-S data both source and receiver transducers are polarized in the same direction. Both traces recorded under water-saturated conditions.

their approach on the fact that in the traditional first-break method, in which the phase velocity is estimated by calculating the time difference between the first-break traveltimes, where the wave energy is seen to arrive, for the transmitted and the received signals (Figure 1.5a), the phase velocity is related to the high-frequency components of the signal which can be significantly different from the dominant lower-frequency phase velocity for a dispersive and anisotropic medium, in which the high frequencies are lost (Rathore *et al.*, 1993; 1994).

The phase velocities for P and S waves were calculated using the measured plug sample length and picked crossover traveltimes as follows:

$$V_{P,S} = \frac{l}{t_{c,r} - t_{c,t}} \tag{4.1}$$

where l is the length of the sample and $t_{c,r}$ and $t_{c,t}$ are the picked zero-crossover traveltimes of the received and transmitted signals, respectively.

For picking the P- and S-wave zero-crossover travel times, a datum time was defined which represents the minimum time, measured on the recorded trace, whose value defines the arrival of some particular P or S wave. This datum time is not necessarily equal to the first-break travel time. The first zero-crossover travel time measured from this datum time represents the most probable P- or S-wave zero-crossover travel time. The method used for defining this datum time is called phase skip method (Figure 4.12) and it will be discussed in detail in subsection 4.3.4, in order to reduce unwanted interferences. The travel time associated with the picked skip, will determine the datum time because the time position of this skip defines the start travel time when a P or S wave is being received without contamination. The travel time between two consecutives skips defines the length of the P or S wave identified using the principle established in the subsection 4.3.1.

The transmitted signal was obtained by placing the source and receiver transducers face-to-face without any material between them. The corresponding signal represents the best approach to the signal generated by the source-transducer (Figure 4.9). Panametrics V103 piezoelectric transducers were used as both P-wave sources and receivers, while Panametrics V153 piezoelectric were used for S-wave sources and receivers. Both broad-

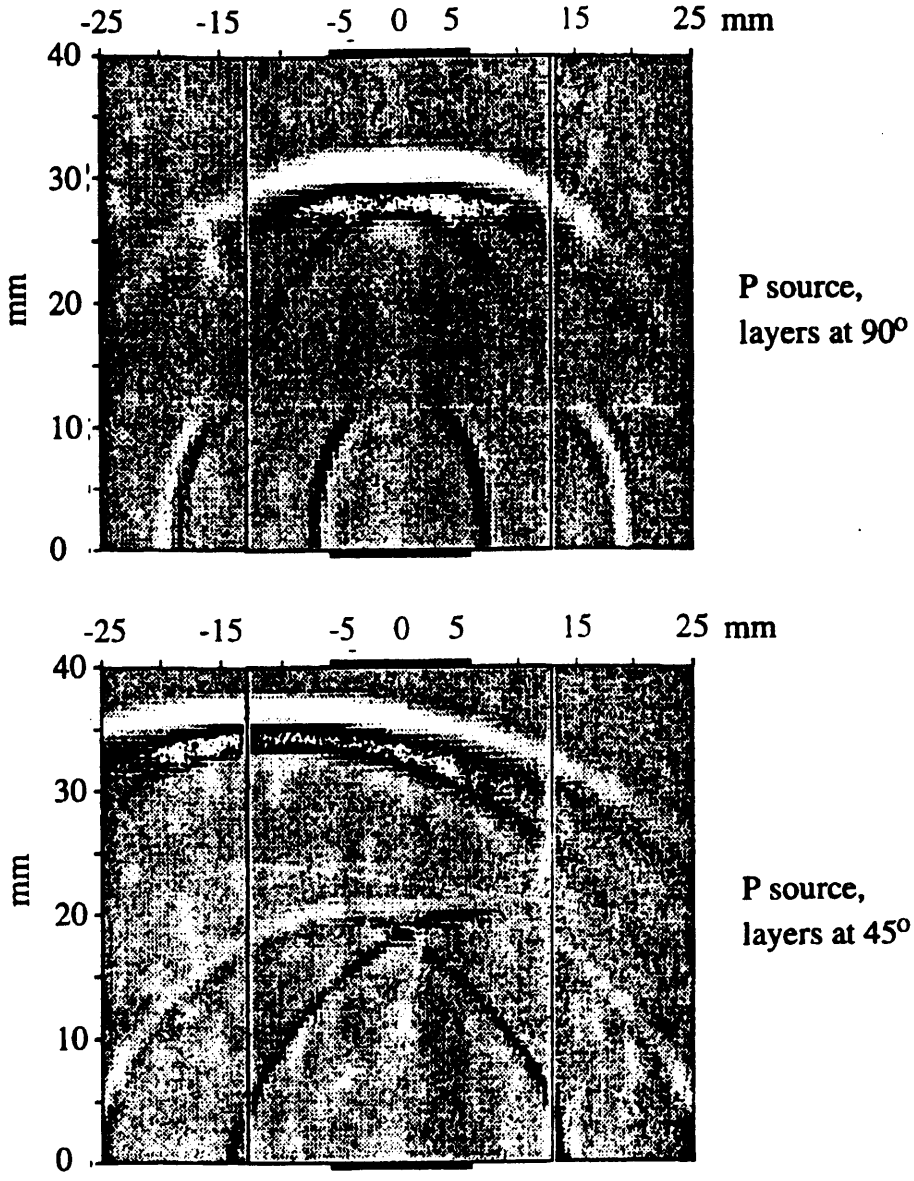

Fig. 4.8 Snapshots showing the simulation of the behavior of qP waves through shale cores cut at 90° and 45°. The top snapshot shows the situation at 7.5 ms, the bottom at 10.0 ms. The vertical bars show the relative width of the cores of Vernik and Nur (1992), while the thick solid lines at the bottom and top show the size and positions of the P-wave source and receiver transducers. Note in the 45°case how the leading part of the wavefront is aiming to miss its intended target, hitting the top of the core somewhat to the left of the receiver (after Dellinger, 1992).

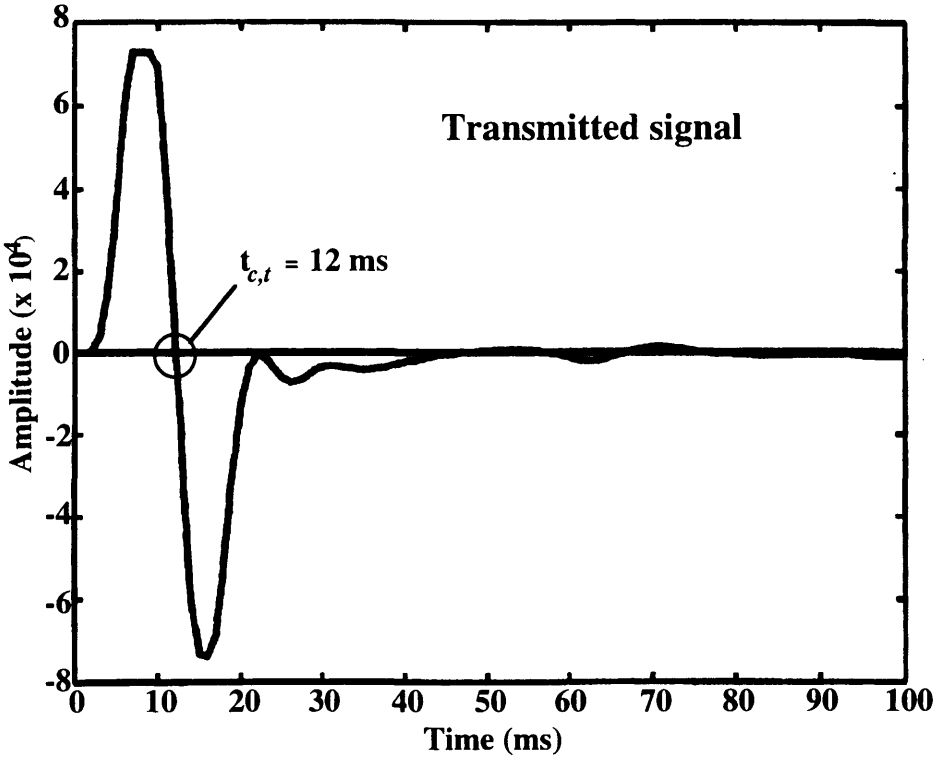

Fig. 4.9 Example of transmitted signal obtained by placing face-to-face the source and receiver transducers. The picked zero-crossover travel time is about of 12 ms.

band transducers have a diameter of 1.51 cm and generate an energy spectra in the range 0.1 to 1.0 MHz.

In the tables 2 and 3 the P- and S-wave phase velocities are indicated for the sixty sandstone samples used in this study under dry and water-saturated conditions. Both phase velocities were estimated at 1.0 MHz using the first-zero-crossing method described by Rathore *et al.*(1993; 1994). The values of the zero-crossing travel times for P and S waves were estimated manually using Promax 2D and the calculated relative velocity error is given by:

$$\frac{\Delta V}{V} = \left(\frac{\Delta l}{l} - \frac{\Delta t}{t}\right) \tag{4.2}$$

where l is the length of the sample in centimeters, t is the measured zero-crossing travel time in milliseconds, Δl is the uncertainty in length, Δt is the uncertainty in travel time and $\Delta V/V$ is the relative velocity error in percent. Here, the uncertainties in length and travel time are 0.1 cm and 1.0 msec, respectively, which gives a maximum relative velocity error of 5% for P and S waves.

To obtain P- and S-wave phase velocity measurements under water-saturated conditions, the sandstone samples were put into a recipient with water and vacuum evacuated at constant pressure from a pump machine connected to the recipient during two or three consecutive days. The qualitative criterion used for considering all the sandstone samples fully saturated was the elimination of air bubbles from the samples. Additionally, the increment of P-wave velocity after water saturation with respect to the observed P-wave velocity under dry condition indicates that all the sandstone samples were fully saturated as indicated in Figure 2.24.

Figure 4.10 shows the schematic diagram of the experimental apparatus used in the transmission technique at atmospheric pressure. A P or S transducer, located at the top of the sample, sent a pulse through a sandstone sample which was received by a similar transducer at the base of the sample. The transmitted pulse was then displayed on the screen of a Nicole oscilloscope connected, through an IBM-XT, which controls the

TABLE 2

P- and S-wave phase velocities measured under dry conditions

SAMPLE	No.	V_P^{dry} (m/s)	$V_{P,c}^{dry}$ (m/s)	V_S^{dry} (m/s)	$V_{S,c}^{dry}$ (m/s)	$t_{P,c}^{dry}$ (ms)	$t_{S,c}^{dry}$ (ms)
W7-13V	1	1602	1597	1276	1275	418	520
W7-25HPE	2	1765	1758	1256	1255	267	370
W7-26HPA	3	1737	1730	1141	1138	227	339
W7-4V	4	1074	1072	821	820	604	786
W7-9HPE	5	1324	1319	963	962	326	442
W7-8HPE	6	1339	1333	862	861	286	436
W7-63V	7	1561	1556	1199	1198	435	317
W7-125HPE	8	1781	1771	1270	1268	231	318
W7-124HPA	9	1780	1767	1228	1226	198	280
W7-91V	10	1910	1902	1454	1452	323	420
W7-178HPA	11	2331	2316	1592	1588	169	241
W7-179HPE	12	2382	2367	1535	1532	178	269
W7-68V	13	1625	1619	1189	1188	379	512
W7-134HPA	14	1684	1676	1182	1181	221	309
W7-135HPE	15	1761	1753	1212	1211	237	338
W7-22V	16	1619	1614	1201	1200	415	554
W7-51HPE	17	1706	1700	1211	1210	273	379
W7-50HPA	18	1728	1720	1212	1210	221	309
W7-28V	19	1550	1545	1120	1097	437	610
W7-62HPA	20	1635	1628	1168	1167	247	340
W7-63HPE	21	1665	1658	1202	1201	264	360
W7-7V	22	1252	1249	1005	1004	544	673
W7-15HPE	23	1397	1393	1042	1041	331	439
W7-16HPA	24	1539	1533	1091	1090	253	351
W7-87V	25	2069	2059	1514	1512	346	466
W7-172HPA	26	2317	2303	1649	1647	186	255
W7-171HPE	27	2356	2341	1601	1600	197	283
263V	28	976	975	696	694	781	1094
263HPA	29	1114	1112	725	724	686	1049
263HPE	30	1159	1157	673	671	646	1107
275V	31	2050	2037	1329	1321	306	468
275HPA	32	1739	1731	1138	1133	440	669
275HPE	33	1484	1479	1093	1089	463	627
285V	34	760	759	503	502	434	651

285HPA	35	930	928	505	504	642	1175
285HPE	36	732	731	345	344	673	1419
286V	37	1152	1149	665	664	331	565
286HPA	38	1151	1148	788	786	487	708
286HPE	39	1157	1155	737	736	646	1008
297V	40	863	862	622	621	542	748
297HPA	41	1023	1021	645	644	713	1125
297HPE	42	1031	1029	597	596	726	1247
W9-201V	43	1110	1108	842	840	440	577
W9-136HPE	44	1268	1264	879	876	229	326
W9-2HPA	45	1229	1225	846	843	293	421
W9A-112V	46	1100	1098	806	804	439	597
W9A-22HPA	47	1227	1223	790	788	289	443
W9A-64HPE	48	1331	1326	928	925	222	315
W9A-114V	49	905	904	690	689	509	665
W9A-29HPA	50	1014	1012	626	625	328	524
W9A-67HPE	51	1134	1131	757	755	281	416
1206V	52	770	769	563	562	720	982
1206HPA	53	981	980	639	638	766	961
1206HPE	54	941	939	541	540	543	938
W7-89V	55	1848	1838	1376	1368	329	440
W7-174HPA	56	2199	2184	1520	1509	183	261
W7-173HPE	57	2193	2177	1490	1479	224	326
W9-294V	58	1766	1758	1275	1268	406	560
W9-177HPE	59	1961	1950	1365	1357	193	274
W9-104HPA	60	1977	1966	1357	1348	202	290

NOMENCLATURE

V_P^{dry} and V_S^{dry} represent P- and S-wave phase velocities under dry conditions, respectively.

$V_{P,c}^{dry}$ and $V_{S,c}^{dry}$ represent P- and S-wave phase velocities under dry conditions after correcting for diffraction effects due to the finite-size of the transducers, respectively.

$t_{P,c}^{dry}$ and $t_{S,c}^{dry}$ represent P- and S-wave picked zero-crossover travel times under dry conditions after correcting for diffraction effects due to the finite-size of the transducers, respectively.

In Table 2 and in the successive tables, it only will be indicated the first digit of the label of the sample (indicating the position of the sample in the sequence) in the second column. The full label associated with the sample is given in Table 1 as reference.

TABLE 3

P- and S-wave phase velocities measured under water-saturated conditions

SAMPLE	No.	V_P^{sat} (m/s)	$V_{P,c}^{sat}$ (m/s)	V_S^{sat} (m/s)	$V_{S,c}^{sat}$ (m/s)	$t_{P,c}^{sat}$ (ms)	$t_{S,c}^{sat}$ (ms)
W7-13V	1	2281	2264	815	814	296	808
W7-25HPE	2	2192	2176	813	812	217	565
W7-26HPA	3	2306	2288	537	536	173	706
W7-4V	4	1979	1967	-	-	333	-
W7-9HPE	5	2044	2032	-	-	215	-
W7-8HPE	6	2017	2005	-	-	193	-
W7-63V	7	2041	2028	-	-	334	-
W7-125HPE	8	2047	2035	-	-	202	-
W7-124HPA	9	2189	2174	-	-	162	-
W7-91V	10	2129	2115	792	791	290	760
W7-178HPA	11	2300	2282	967	966	170	388
W7-179HPE	12	2145	2131	1009	1008	195	402
W7-68V	13	1939	1928	-	-	318	-
W7-134HPA	14	1910	1900	557	556	196	643
W7-135HPE	15	1981	1970	593	592	211	679
W7-22V	16	2186	2171	719	719	310	919
W7-51HPE	17	2196	2180	805	804	214	564
W7-50HPA	18	2185	2170	858	857	176	431
W7-28V	19	2113	2099	-	-	322	-
W7-62HPA	20	2141	2127	781	779	191	504
W7-63HPE	21	2135	2121	805	804	208	532
W7-7V	22	2065	2052	878	877	333	769
W7-15HPE	23	2077	2064	825	824	226	-
W7-16HPA	24	2096	2083	724	723	189	524
W7-87V	25	2357	2338	969	968	303	722
W7-172HPA	26	2284	2266	1084	1083	187	381
W7-171HPE	27	2307	2289	-	-	200	-
263V	28	1933	1922	-	-	369	-
263HPA	29	1812	1803	-	-	426	-
263HPE	30	1900	1890	-	-	394	-
275V	31	2497	2474	600	599	253	1019
275HPA	32	2293	2276	-	-	336	-
275HPE	33	2242	2226	-	-	311	-
285V	34	1883	1873	-	-	134	-
285HPA	35	1881	1871	-	-	288	-
285HPE	36	1881	1871	-	-	209	-
286V	37	1893	1883	-	-	165	-
286HPA	38	1879	1869	-	-	249	-

286HPE	39	1866	1856	-	-	371	-
297V	40	1913	1903	-	-	226	-
297HPA	41	1913	1903	-	-	378	-
297HPE	42	1928	1917	-	-	373	-
W9-201V	43	1964	1955	-	-	254	-
W9-136HPE	44	1920	1909	-	-	155	-
W9-2HPA	45	1961	1952	-	-	188	-
W9A-112V	46	2023	2013	-	-	244	-
W9A-22HPA	47	1973	1963	-	-	184	-
W9A-64HPE	48	2022	2010	-	-	150	-
W9A-114V	49	1940	1931	-	-	244	-
W9A-29HPA	50	1920	1910	-	-	179	-
W9A-67HPE	51	1958	1947	-	-	168	-
1206V	52	1902	1893	-	-	299	-
1206HPA	53	1930	1921	-	-	395	-
1206HPE	54	1968	1959	-	-	266	-
W7-89V	55	2280	2265	1031	1030	269	580
W7-174HPA	56	2465	2447	1157	1156	164	336
W7-173HPE	57	2454	2435	1128	1127	201	425
W9-294V	58	2050	2035	702	701	351	1003
W9-177HPE	59	2001	1991	794	793	189	460
W9-104HPA	60	2103	2092	836	835	190	461

NOMENCLATURE

V_P^{sat} and V_S^{sat} represent P- and S-wave phase velocities under water-saturated conditions, respectively.

$V_{P,c}^{sat}$ and $V_{S,c}^{sat}$ represent P- and S-wave phase velocities under water-saturated conditions after correcting for diffraction effects due to the finite-size of the transducers, respectively.

$t_{P,c}^{sat}$ and $t_{S,c}^{sat}$ represent P- and S-wave picked zero-crossover travel times under water-saturated conditions after correcting for diffraction effects, respectively.

The missing values in the 4th, 6th and 8th columns are associated with those S waves which have been so strongly attenuated. As a result, the estimation of their zero-crossover travel times and phase velocities was impossible.

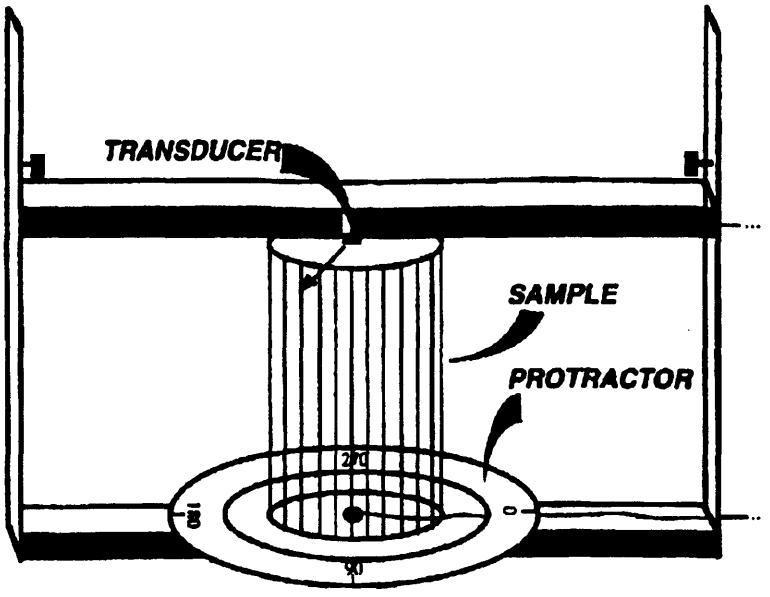

Fig. 4.10 Schematic diagram of apparatus used for phase-velocity and attenuation measurements of P and S waves under dry and water-saturated conditions. The apparatus clamps the sample between two P- or S-wave transducers (source and receiver) of parallel and orthogonal polarization, respectively. For measuring the effect of the S-wave polarization on the experimental measurements, a circular protractor scale was added for determining the azimuth of the rotation (after Sun, 1994).

experiment, to a Perkin-Elmer 3240 seismic processing system for storage and subsequent data processing.

The signal was sampled at 100 ns for reducing the aliasing effect, which represents an equivalent sampling rate in the field of 1.0 ms.

4.3.3 Seismic attenuation estimation

There are different methods proposed for estimating the coefficient of attenuation (or, equivalently, quality factor Q) from samples and cores in the laboratory and the field (Ward and Toksöz, 1971; Elsey *et al.*, 1977; Toksöz *et al.*, 1979; Jannsen *et al.*, 1985; Tonn, 1991). But the spectral ratio technique has been the most popular in the laboratory. In fact, for all transmission methods, one of the most reliable techniques for obtaining the attenuation from the recorded signals consists in comparing the spectral amplitudes at different frequencies (Ward and Toksöz, 1971; Toksöz *et al.*, 1979). Because attenuation implies a preferential loss of the high frequencies, a change in the total spectrum will therefore occur (Figure 1.6).

Using the spectral ratio technique, it is possible to isolate experimental variables which affect the measured attenuation values, *e.g.* the effects on the absolute amplitudes produced by the measurement system and the frequency response of the transducers, considering that experimental conditions (geometry, coupling conditions, transducers) remain unchanged during the experiment (Toksöz *et al.*, 1979).

The spectral ratio method considers that the amplitudes for the reference and the sample can be expressed as follows (Toksöz *et al.*, 1979):

$$A_r(f) = G_r(f,l)e^{-la_r(f)} \qquad \text{(reference)} \tag{4.3}$$

$$A_s(f) = G_s(f,l)e^{-la_s(f)} \qquad \text{(sample)} \tag{4.4}$$

where f is the frequency, l is the length of the sample, v is the phase velocity, ω (= $2\pi f$) is the angular frequency, and $G(f,l)$ is the geometrical factor which includes the reflections, refractions and diffractions, $a(f)$ is the frequency-dependent attenuation coefficient and the subscripts r and s refer to the reference and the sample, respectively. Therefore, the amplitude ratio is given by:

$$\ln\ (A_r / A_s) = \ln\ (G_r / G_s) + (a_s - a_r)l \tag{4.5}$$

By assuming $a(f)$ is a linear function of the frequency (Toksöz *et al.*, 1979; Sears and Bonner, 1981; Knopoff, 1969) such that:

$$a(f) = \gamma f \tag{4.6}$$

then, eq. (4.4) is reduced to:

$$\ln\ (A_r / A_s) = \ln\ (G_r / G_s) + (\gamma_s - \gamma_r)lf \tag{4.7}$$

Keeping the same geometry for both the reference and the sample, the G_r / G_s ratio is a frequency-independent scale factor.

If the spectral ratio $\ln (A_r / A_s)$ is plotted against frequency, f, then $(\gamma_s - \gamma_r)$ can be found from the slope of the linear relation by least-squares regression (Figure 1.6). In the laboratory aluminum is normally used as the reference material, with an associated quality factor value of about 150,000, then $\gamma_r \cong 0$, and γ_s or a_s of the sandstone sample can be determined directly from the slope indicated in eq. (4.7). The attenuation coefficient a_s is evaluated in either nepers per meter (Np/m) or decibels per meter (dB/m), using the following relation (Ristic, 1980):

$$a\ [dB/m] = 8.686a\ [Np/m] \tag{4.8}$$

The above spectral ratio technique was applied on the sixty sandstone samples for measuring their corresponding attenuation coefficients and quality factors under dry and water-saturated conditions. But, it was adapted to account for the variations in length of the sandstone samples, which made it impossible to use a single reference sample (aluminum). This signal through the aluminum sample was replaced by the signal acquired placing the transducers face-to-face. The recorded signal is assumed to be a free-attenuation signal ($\gamma_s = 0$).

A fast Fourier transform (FFT) subroutine was used for calculating a 1024-point transform (for P-waves) and a 2048-point transform (for S-waves) returning the real and imaginary parts of the Fourier transform representing their amplitude spectra. Additionally, a Fortran program reads the corresponding amplitude spectra of the signal recorded with the transducers face-to-face and sandstone sample, giving the spectral ratio values as a function of the frequency. The slope of the linear trend, observed after plotting the spectral ratio values versus frequency, was determined using least-squares fit method.

The application of the spectral ratio technique on two sandstone samples from WOSPP for estimating their attenuation coefficients is shown in Figure 4.11. The tables 4 and 5 show the measured attenuation coefficients under dry and water-saturated conditions for the sixty sandstone samples used in this study.

4.3.4 Time truncation of recorded P and S signals

Because P and S signals may be contaminated by extra arrivals, *e.g.*, multiples, normally both signals are truncated to get rid of these extra arrivals. But truncation usually affects the spectra especially when a portion of the signal is removed because of the truncation. Therefore, if later parts of both P and S signals are mixed with extra arrivals, truncated or not, their spectra will be affected to a certain extent and their estimated attenuations using the spectral ratio method will be affected too (Tang *et. al.*, 1992).

For reducing the effects of extra arrivals on spectra of P and S waves during all the attenuation coefficient measurements the phase skip criterion was used. The method is based on studying the phase behavior of the signal. The phase skip criterion can be formulated as follows: "The instantaneous phase in an undisturbed signal increases or

TABLE 4

P- and S-wave attenuation coefficients measured under dry conditions

SAMPLE	No.	a_P^{dry} (dB / cm)	$a_{P,c}^{dry}$ (dB / cm)	a_S^{dry} (dB / cm)	$a_{S,c}^{dry}$ (dB / cm)	$Q_{P,c}^{dry}$	$Q_{S,c}^{dry}$
W7-13V	1	19.03	18.28	17.87	17.26	9.35	12.40
W7-25HPE	2	24.26	23.41	20.90	20.27	6.63	10.73
W7-26HPA	3	24.46	23.61	27.13	26.53	6.68	9.04
W7-4V	4	26.80	26.27	67.67	67.25	9.69	4.95
W7-9HPE	5	26.94	26.27	60.00	59.49	7.88	4.77
W7-8HPE	6	44.26	43.57	55.32	54.85	4.70	5.78
W7-63V	7	18.53	17.79	16.80	16.22	9.86	14.04
W7-125HPE	8	13.04	12.17	21.61	20.96	12.66	10.27
W7-124HPA	9	55.17	54.28	20.20	19.55	2.85	11.38
W7-91V	10	4.19	3.29	6.19	5.49	43.56	34.25
W7-178HPA	11	3.72	2.60	19.77	18.97	45.28	9.06
W7-179HPE	12	3.21	2.08	16.24	15.47	55.56	11.51
W7-68V	13	8.10	7.33	14.73	14.15	22.99	16.24
W7-134HPA	14	15.24	14.40	23.76	23.14	11.31	9.99
W7-135HPE	15	11.09	10.23	18.61	17.98	15.22	12.53
W7-22V	16	14.61	13.84	15.93	15.35	12.21	14.82
W7-51HPE	17	16.18	15.35	17.87	17.25	10.46	13.07
W7-50HPA	18	15.77	14.91	18.97	18.33	10.64	12.30
W7-28V	19	13.88	13.15	14.78	14.24	13.43	17.47
W7-62HPA	20	15.45	14.64	20.46	19.85	11.45	11.78
W7-63HPE	21	16.10	15.29	19.34	18.72	10.77	12.14
W7-7V	22	17.81	17.21	23.56	23.07	12.69	11.78
W7-15HPE	23	23.46	22.77	38.31	37.77	8.60	6.94
W7-16HPA	24	23.34	22.57	37.77	37.20	7.89	6.73
W7-87V	25	2.38	1.42	5.89	5.18	93.19	34.85
W7-172HPA	26	3.09	1.99	5.09	4.28	59.51	38.74
W7-171HPE	27	2.79	1.68	4.53	3.74	69.54	45.58
263V	28	22.48	22.00	41.27	40.91	12.72	9.61
263HPA	29	46.85	46.32	59.87	59.50	5.30	6.33
263HPE	30	25.60	25.04	43.67	43.32	9.42	7.78
275V	31	9.24	8.29	48.12	47.75	16.16	11.27
275HPA	32	10.20	9.39	18.97	18.33	16.78	14.06
275HPE	33	17.33	16.62	17.68	17.13	11.10	7.07
285V	34	119.18	118.69	447.00	446.00	3.03	1.22
285HPA	35	65.84	65.36	53.52	53.23	4.50	10.17
285HPE	36	168.45	168.03	154.18	153.93	2.22	5.15
286V	37	47.24	46.61	69.91	69.49	5.10	5.91

286HPA	38	46.60	46.01	75.96	75.54	5.17	4.60
286HPE	39	29.56	29.00	40.86	40.48	8.15	9.16
297V	40	49.56	49.09	64.48	64.12	6.45	6.85
297HPA	41	35.57	35.07	49.53	49.20	7.62	8.61
297HPE	42	43.22	42.72	46.02	45.71	6.21	10.02
W9-201V	43	29.91	29.35	39.30	38.85	8.39	8.36
W9-136HPE	44	46.49	45.80	57.56	57.05	4.71	5.46
W9-2HPA	45	39.14	38.50	64.00	63.53	5.79	5.10
W9A-112V	46	33.51	32.95	44.18	43.75	7.54	7.76
W9A-22HPA	47	34.19	33.55	44.23	43.78	6.65	7.91
W9A-64HPE	48	35.57	35.06	64.61	64.07	5.87	4.60
W9A-114V	49	41.23	40.75	77.07	76.70	7.41	5.17
W9A-29HPA	50	39.04	38.48	102.24	101.90	7.01	4.29
W9A-67HPE	51	50.95	50.33	56.04	55.59	4.79	6.50
1206V	52	47.16	46.75	105.64	105.32	7.59	4.61
1206HPA	53	40.34	39.86	47.56	47.17	6.99	7.42
1206HPE	54	78.71	78.22	72.90	72.59	3.72	6.96
W7-89V	55	6.25	5.38	5.84	5.18	27.61	38.50
W7-174HPA	56	4.03	2.98	11.50	10.74	41.97	16.84
W7-173HPE	57	3.67	2.63	11.94	11.22	47.62	16.45
W9-294V	58	5.79	4.97	9.30	8.70	31.24	24.75
W9-177HPE	59	8.04	7.08	22.83	22.13	19.77	9.09
W9-104HPA	60	6.47	5.51	14.53	13.84	25.20	14.63

NOMENCLATURE

a_P^{dry} and a_S^{dry} represent P- and S-wave attenuation coefficients under dry conditions, respectively.

$a_{P,c}^{dry}$ and $a_{S,c}^{dry}$ represent P- and S-wave attenuation coefficients under dry conditions after correcting for diffraction effects due to the finite-size of the transducers, respectively.

$Q_{P,c}^{dry}$ and $Q_{S,c}^{dry}$ represent P- and S-wave quality factors under dry conditions after correcting for diffraction effects due to the finite-size of the transducers, respectively.

TABLE 5

P- and S-wave attenuation coefficients measured under water-saturated conditions

SAMPLE	No.	a_P^{sat} (dB / cm)	a_{Pc}^{sat} (dB / cm)	a_S^{sat} (dB / cm)	a_{Sc}^{sat} (dB / cm)	Q_P^{sat}	Q_S^{sat}
W7-13V	1	16.26	15.21	72.78	72.36	7.93	4.63
W7-25HPE	2	7.72	6.69	114.71	114.28	18.76	2.94
W7-26HPA	3	21.60	20.50	144.94	144.60	5.82	3.52
W7-4V	4	48.49	47.57	-	-	2.92	-
W7-9HPE	5	18.87	17.90	-	-	7.50	-
W7-8HPE	6	24.36	23.38	-	-	5.82	-
W7-63V	7	13.42	12.47	-	-	10.79	-
W7-125HPE	8	7.96	6.97	-	-	19.23	-
W7-124HPA	9	16.18	15.12	-	-	8.30	-
W7-91V	10	11.29	10.30	78.28	77.87	12.52	4.43
W7-178HPA	11	11.48	10.38	69.13	68.61	11.52	4.12
W7-179HPE	12	31.59	30.56	79.86	79.33	4.19	3.41
W7-68V	13	48.08	47.17	-	-	3.00	-
W7-134HPA	14	17.57	16.63	27.02	26.67	8.64	18.40
W7-135HPE	15	14.27	13.31	39.14	38.79	10.41	11.88
W7-22V	16	14.23	13.22	76.73	76.36	9.51	4.97
W7-51HPE	17	15.77	14.73	82.89	82.46	8.50	4.12
W7-50HPA	18	19.15	18.09	103.69	103.21	6.95	3.09
W7-28V	19	16.74	15.77	-	-	8.25	-
W7-62HPA	20	16.15	15.12	93.52	93.09	8.49	3.76
W7-63HPE	21	19.46	18.45	68.52	68.08	6.98	4.99
W7-7V	22	40.96	40.00	51.95	51.51	3.32	6.04
W7-15HPE	23	17.54	16.55	-	-	7.99	-
W7-16HPA	24	18.04	17.03	106.90	106.50	7.69	3.55
W7-87V	25	9.65	8.57	51.89	51.41	13.62	5.48
W7-172HPA	26	32.42	31.33	64.45	63.89	3.84	3.94
W7-171HPE	27	28.53	27.44	-	-	4.35	-
263V	28	11.08	10.19	-	-	13.94	-
263HPA	29	8.25	7.41	-	-	20.43	-
263HPE	30	8.87	7.99	-	-	18.06	-
275V	31	8.86	7.72	108.34	108.02	14.30	4.22
275HPA	32	21.80	20.76	-	-	5.78	-
275HPE	33	8.03	7.00	-	-	17.50	-
285V	34	17.93	16.99	-	-	8.57	-
285HPA	35	14.55	13.67	-	-	10.67	-
285HPE	36	17.49	16.59	-	-	8.79	-
286V	37	26.99	26.07	-	-	5.56	-

286HPA	38	17.99	17.11	-	-	8.53	-
286HPE	39	38.68	37.82	-	-	3.89	-
297V	40	22.42	21.51	-	-	6.67	-
297HPA	41	11.19	10.30	-	-	13.92	-
297HPE	42	13.38	12.49	-	-	11.40	-
W9-201V	43	20.55	19.62	-	-	7.12	-
W9-136HPE	44	29.25	28.28	-	-	5.05	-
W9-2HPA	45	28.94	27.97	-	-	4.50	-
W9A-112V	46	20.15	19.19	-	-	7.07	-
W9A-22HPA	47	26.24	25.27	-	-	5.50	-
W9A-64HPE	48	28.60	27.59	-	-	4.92	-
W9A-114V	49	23.33	22.40	-	-	6.31	-
W9A-29HPA	50	21.27	20.32	-	-	7.03	-
W9A-67HPE	51	26.26	25.29	-	-	5.54	-
1206V	52	12.48	11.58	-	-	12.45	-
1206HPA	53	27.11	26.22	-	-	5.42	-
1206HPE	54	19.36	18.43	-	-	7.56	-
W7-89V	55	26.56	25.51	127.55	127.04	4.72	2.09
W7-174HPA	56	11.96	10.79	47.01	46.41	10.34	5.09
W7-173HPE	57	11.20	10.06	46.79	46.21	11.14	5.24
W9-294V	58	17.00	16.88	104.70	104.30	9.02	3.73
W9-177HPE	59	16.59	15.61	82.44	81.99	8.78	4.20
W9-104HPA	60	50.17	49.16	89.90	89.43	2.65	3.65

NOMENCLATURE

a_P^{sat} and a_S^{sat} represent P- and S-wave attenuation coefficients under water-saturated conditions, respectively.

$a_{P,c}^{sat}$ and $a_{S,c}^{sat}$ represent P- and S-wave attenuation coefficients under water-saturated conditions after correcting for diffraction effects due to the finite-size of the transducers, respectively.

$Q_{P,c}^{sat}$ and $Q_{S,c}^{sat}$ represent P- and S-wave quality factors under water-saturated conditions after correcting for diffraction effects due to the finite-size of the transducers, respectively.

The missing values in the 4th, 6th and 8th columns are associated with those S waves which have been so strongly attenuated. As a result, the estimation of their attenuation coefficients and quality factors was impossible.

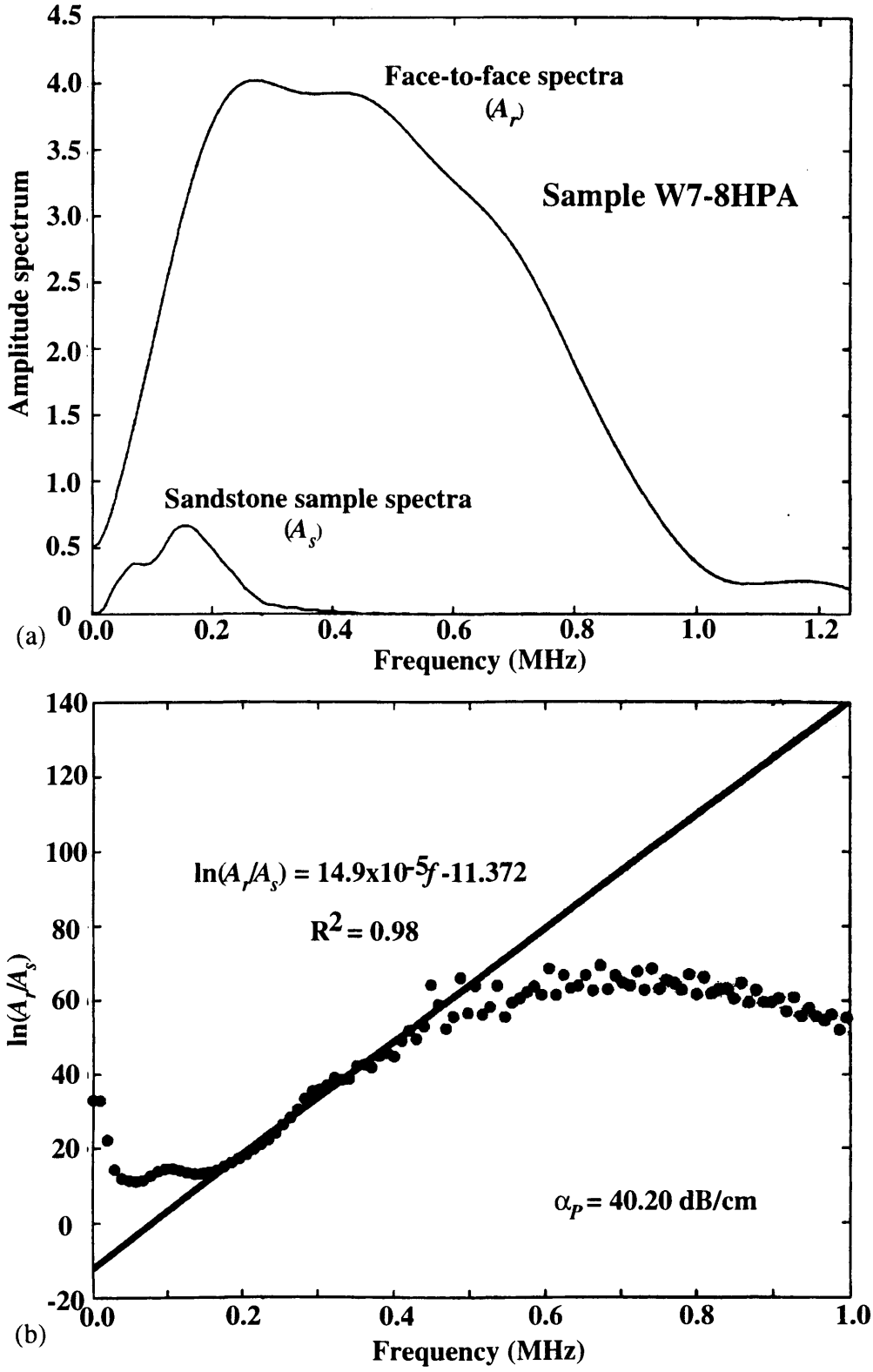

Fig. 4.11 (a) Face-to-face and sandstone sample spectra versus frquency. (b) Logarithmic amplitude ratio for reference and sandstone samples and linear fit using least-squares method for estimating the attenuation coefficient value of the sandstone sample.

decreases monotonously with the signal's duration. If the initial signal is distorted by interference of new signal arrivals, then the instantaneous phase of the compound signal will mark the times of the new energy arrivals by skips (Taner and Sheriff, 1977)". Figure 4.12 shows the application of the phase skip criterion on an idealized contaminated signal. The instantaneous phases of both P and S waves were calculated using the Hilbert transform (Claerbout, 1977; Taner *et. al.*, 1979). But, being interested in changes of phase with time the first derivative of the instantaneous phase was calculated. This quantity is known as the instantaneous frequency (Taner and Sheriff, 1977; Taner *et. al.*, 1979).

Figure 4.13 shows an example of the application of the phase skip criterion on a recorded trace after traveling through a sandstone sample from WOSPP. In both examples it is evident how the selection of skips in the instantaneous phase helps to identify the extremes of both P and S signals. Sometimes the instantaneous phase can exhibit multiple skips which makes the application of the phase criterion very difficult. An alternative way to apply this criterion is based on the use of the expected time window of arrivals and rule out of insignificant phase skips for obtaining reasonable skip choices.

4.3.5 Diffraction and finite-size transducer corrections for phase velocity and attenuation

Seki *et al.* (1956) and Papadakis (1966) simulated a piezoelectric radiator transducer as a circular radiator of radius a (Figure 4.14) and the piezoelectric receiver transducer was considered also as a circular receiver with the same radius. These authors found that the maximum pressure over the circular receiving area produced by a pulse generated by the circular radiator varies as a function of radial position x and axial position z as shown in Figure 4.15a (Seki *et al.*, 1956). Additionally, the wavefront which reaches the circular receiver is not strictly planar, i.e., positive and negative pressures occurring simultaneously in different parts of the receiver area can give interference. As result, the phase of the arriving pulse also varies as function of radial and axial positions (Figure 4.15b), contributing to an apparent attenuation due to interference (Seki *et al.*, 1955; Papadakis, 1966).

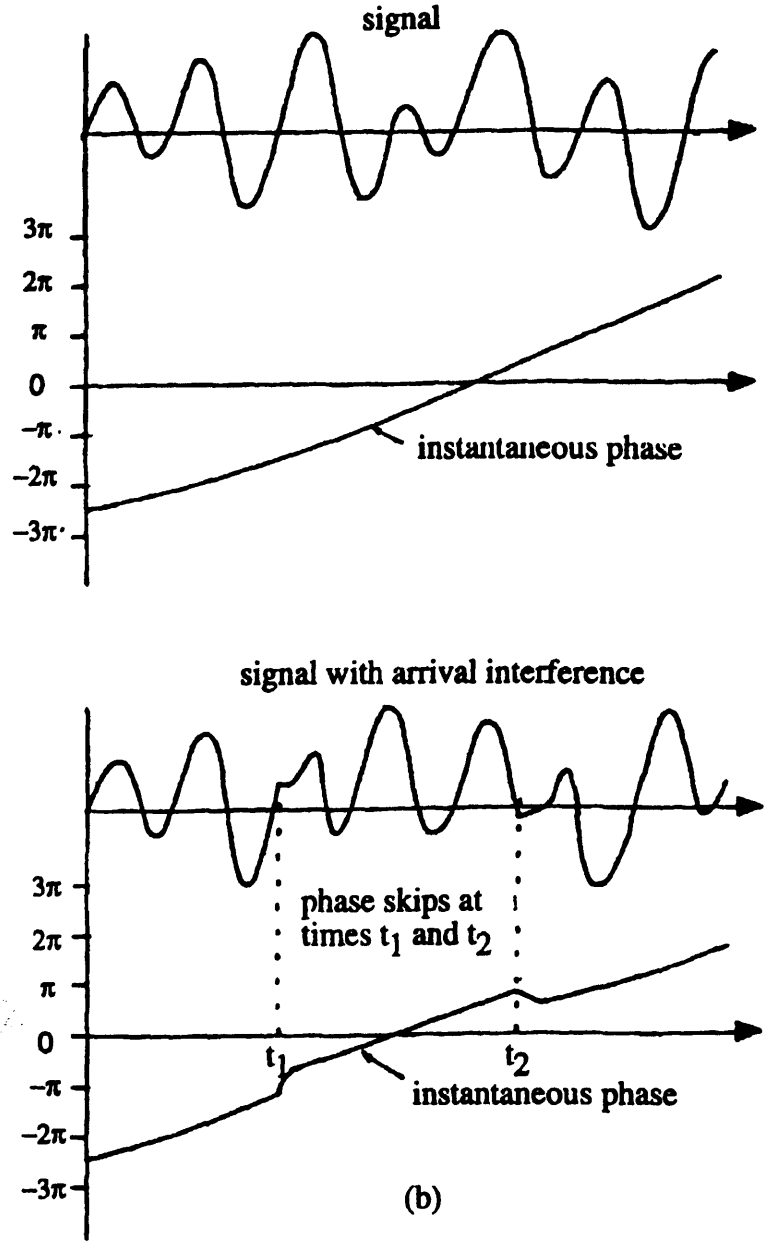

Fig. 4.12 Idealized comparison between a signal (a) without phase skip and (b) with phase skip. The positions of the phase skips at times t_1 and t_2 are indicated by the discontinuities in the instantaneous phase (after Taner and Sheriff, 1977).

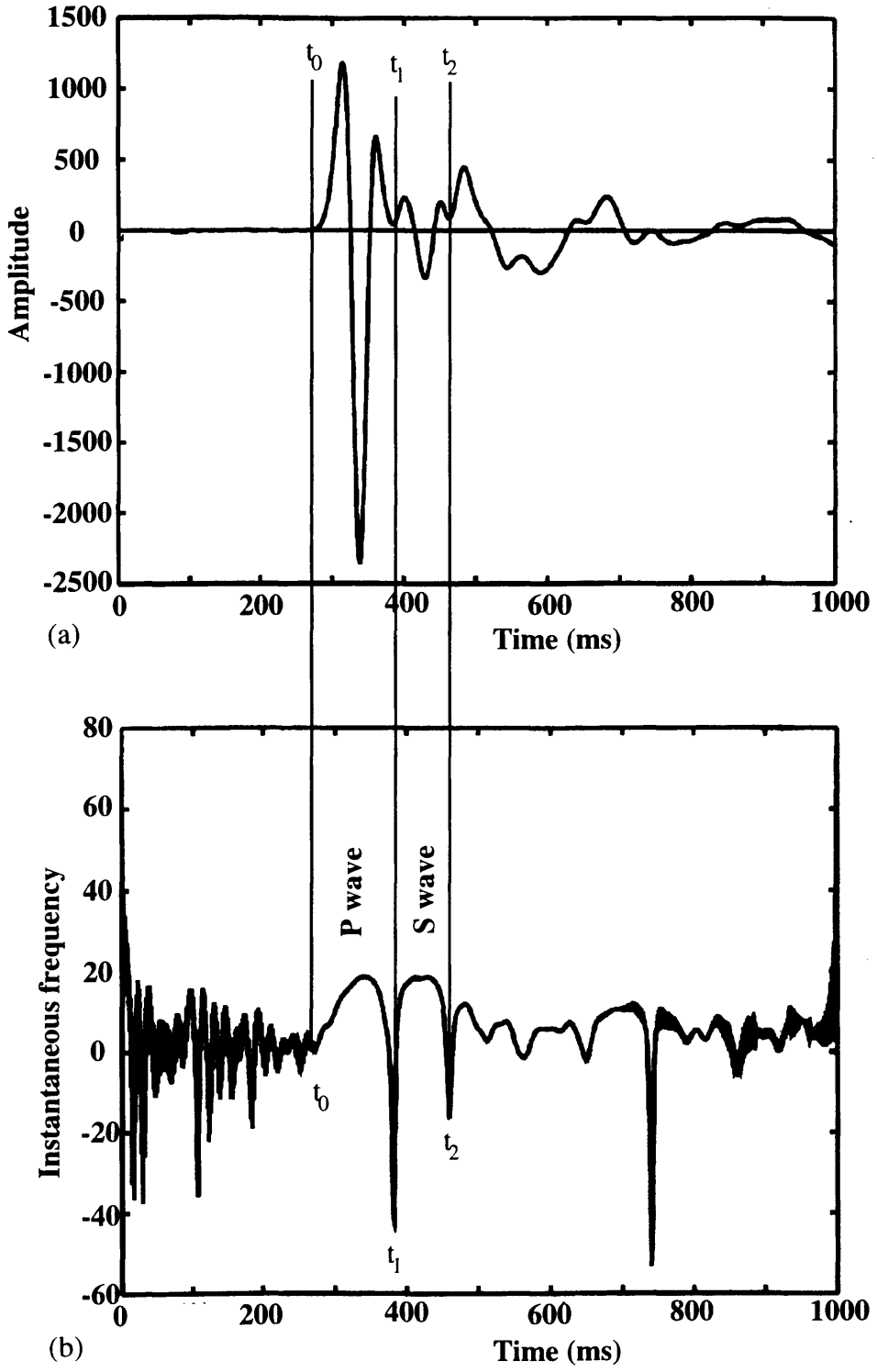

Fig. 4.13 (a) An example of recorded trace. (b) The corresponding Hilbert transform of the instantaneous frequency defining the magnitude of the skips. The times of the principal skips observed in (b) are associated with the start and end of two waves in (a).

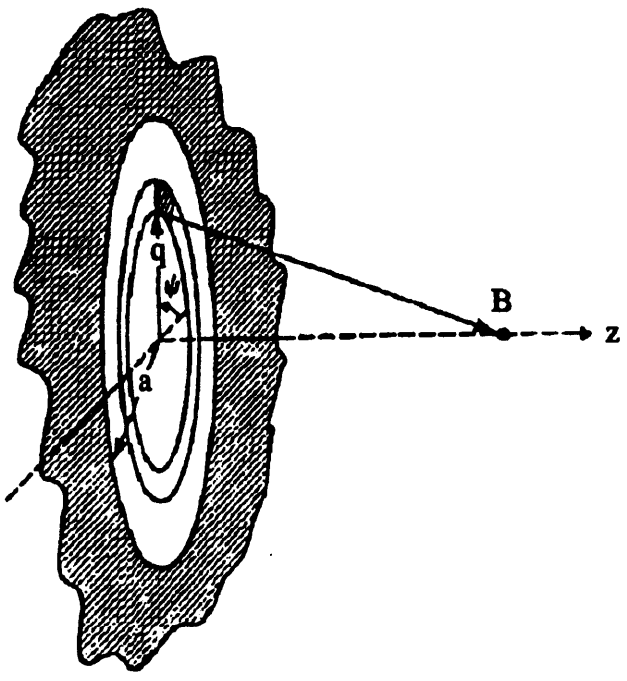

Fig. 4.14 Geometry for simulating a piezoelectric source and receiver transducers of radius *a*. The z-axis defines the axial position (after Ristic, 1987).

This phase increment represents an error in the travel time in velocity phase measurements. The expression for the time increment is given by Papadakis (1966) as:

$$\Delta t = \phi\left(S_c\right)\Big/2\pi f_c \tag{4.9}$$

where ϕ represents the phase delay and S_c the normalized distance at the central frequency f_c of the broad-band signal. Additionally, the normalized distance S_c is defined as:

$$S_c = \frac{lv}{r^2 f_c} \tag{4.10}$$

where l is the length of the sample, v is the velocity and r is the transducer radius (Papadakis, 1966). The time increment Δt is to be added to the measured value t' of the first arrival or first zero-crossing traveltimes to get the true travel time t, thus:

$$t = t' + \Delta t \tag{4.11}$$

Other things being equal, Δt decreases as f_c increases because f_c is in the denominator of Δt explicitly and in the denominator of S_c also (McSkimin, 1962; Barshauskas *et al.*, 1964; Papadakis, 1966).

Then, the phase velocity after applying the diffraction correction is lower than obtained without considering this correction because the traveltime is increased keeping the length of the sample constant. At high frequencies the effect of the diffraction correction on the traveltime is lower than the associated with low frequencies (Papadakis, 1966).

Additionally, the diffractions produced by the limited size of the transducers affect the phase of the arriving pulse creating an apparent attenuation as was established in the

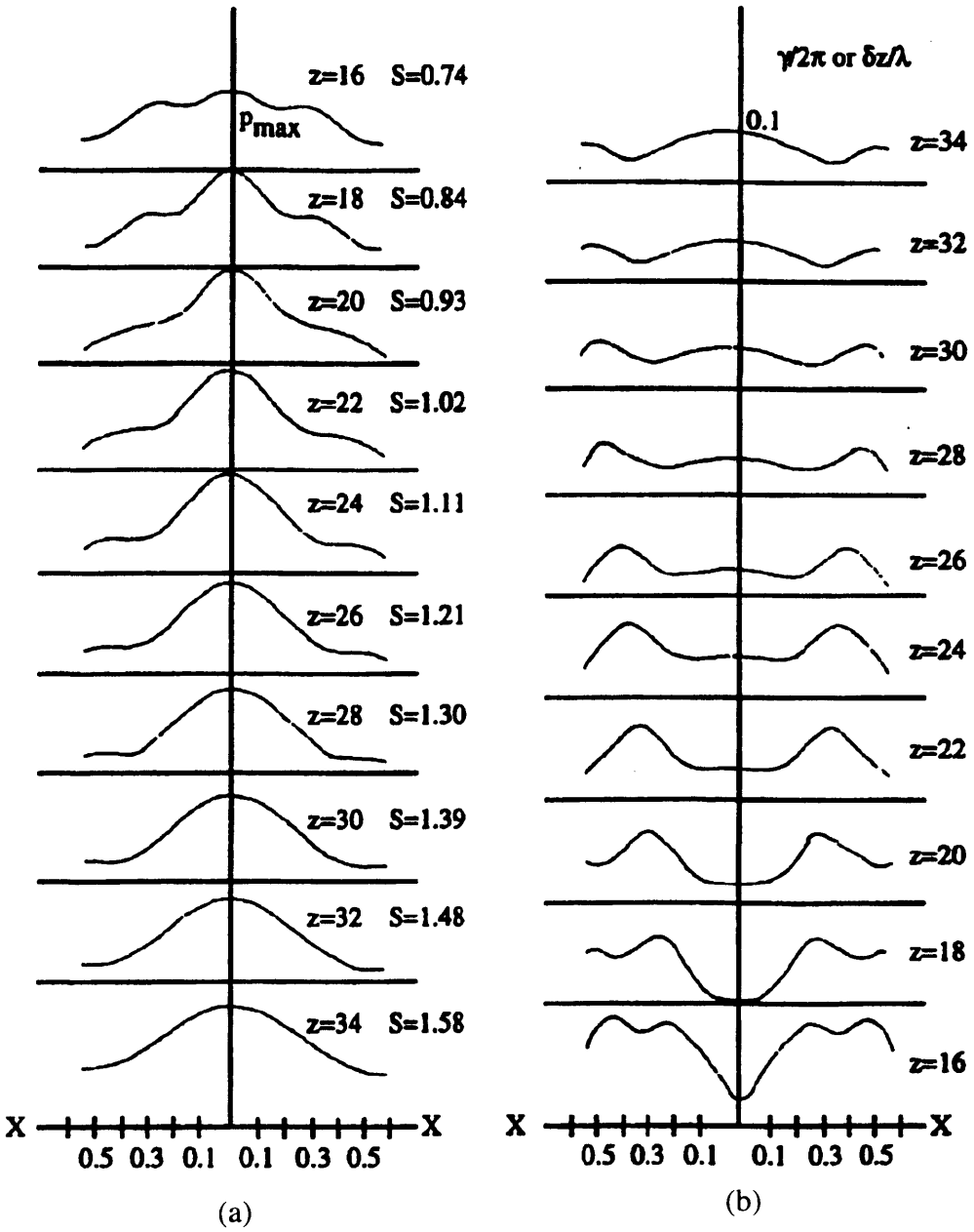

Fig. 4.15 (a) Maximum pressure profiles as a function of radial position x and axial position z. S is the same distance measured in units of a^2/λ. (b) Phase angle ($\gamma/2\pi$) variation across the receiver for successive axial positions. These profiles approximate very closely the shape of the wavefront (after Seki *et al.*, 1955).

section 4.4 (Seki *et al.*, 1955; Papadakis, 1966). The attenuation correction Δa is subtracted from the measured attenuation a' to get the true attenuation α:

$$a = a' - \Delta a \tag{4.12}$$

In general, for a given size of transducers, the attenuation correction is higher at low frequencies (Papadakis, 1966). Figure 4.16 shows the effect of applying the Papadakis attenuation correction to two rocks used by Klimentos (1991). The effect is enhanced at lower frequencies on the high Q (low attenuation) sample.

Bourbie *et al.* (1987) comment that the Papadakis corrections are computed for homogeneous liquid media, and their failure to fit the data of Tarif (1986) for solid material, implies that they must be used with caution, especially for high Q (low attenuation coefficient) samples. The experimental results about the attenuation measurements for the sandstone samples from WOSPP show that these samples have in general low Q (high attenuation coefficient) values (Tables 4 and 5). As a result, the Papadakis attenuation corrections were considered as valid for these sandstone samples.

The Papadakis corrections for phase velocity and attenuation have been tabulated by Benson and Kiyohara (1974). Their table is frequently used in the laboratory experiments (Best, 1994; Best *et al.*, 1994; Klimentos and McCann, 1990; Klimentos, 1991; Whinkler and Plona, 1982 among others) for correcting the velocity and attenuation measurements due to the finite-size transducer effect as function of the normalized distance, S_c.

Tables 2-5 show the effect of applying the diffraction corrections to the estimated P- and S-wave phase velocities and attenuations for the sixty sandstone samples from WOSPP under dry and water-saturated conditions using the tabulated corrections published by Benson and Kiyohara (1974).

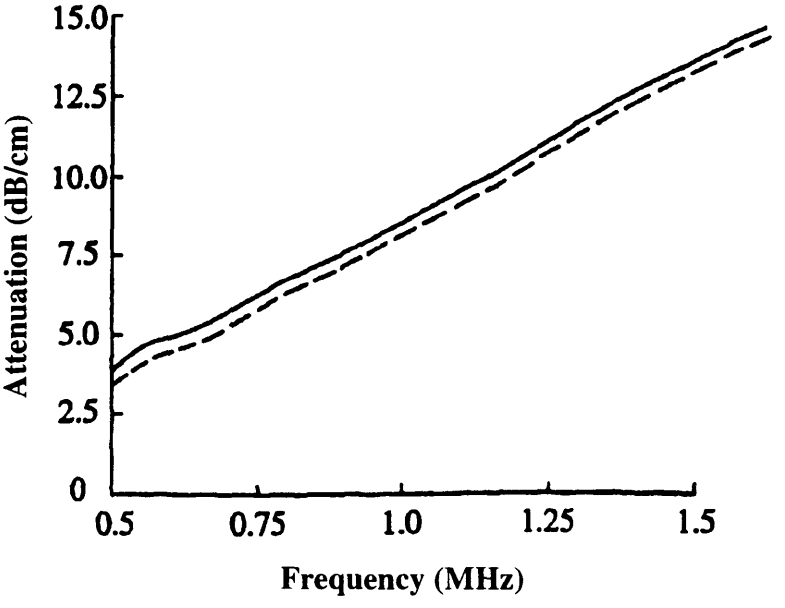

(a)

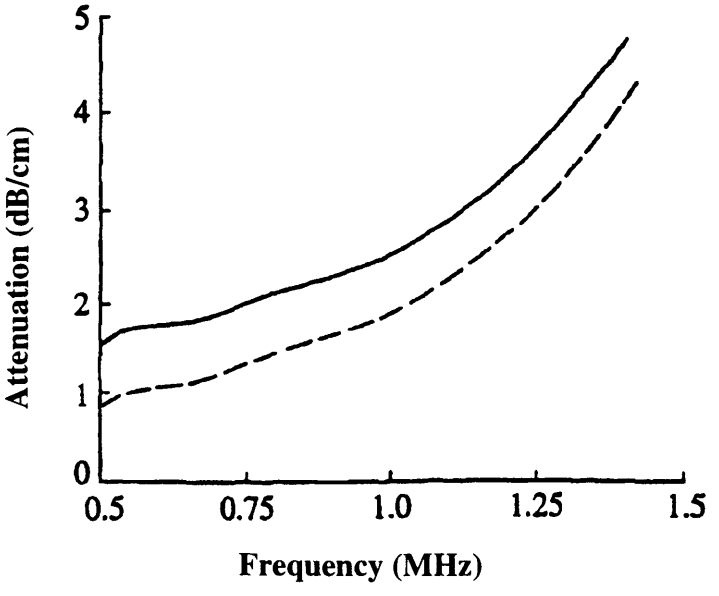

(b)

Fig. 4.16 (a) Comparison between spectra for rock 5VM1 uncorrected (solid curve) and corrected (dashed curve) for attenuation induced by the finite-size of the transducer. (b) Comparison between spectra for rock B3BP uncorrected (solid curve) and corrected (dashed curve) for attenuation induced by the finite-size of the transducer. All measurements at atmospheric pressure (after Klimentos, 1991).

4.4 Experimental relationships among P-wave velocity, S-wave velocity, clay content, porosity and permeability

4.4.1 Relationship between compressional-wave velocity and shear-wave velocity

Figure 4.17a shows the experimental relationship between compressional-wave velocity V_P and shear-wave velocity V_S measured along the Z direction under dry condition. The P-wave phase velocities under dry conditions are indicated in Table 2 for the sixty sandstone samples from WOSPP. The least-squares linear regression estimates this relationship as:

$$V_P = 1.30\ V_S + (69.8 \pm 0.7) \quad \text{(m/s)} \qquad (4.13a)$$

with a correlation factor of 0.95. The corresponding relationship between V_P and V_S along the X direction is given by:

$$V_P = 1.31\ V_S + (176.6 \pm 0.4) \quad \text{(m/s)} \qquad (4.13b)$$

with a correlation factor of 0.97 (Figure 4.17b). All the P- and S-wave phase velocities are expressed in m/s. These experimental results are in reasonable agreement with a general relationship between V_P and V_S for clastic silicate rocks published by Castagna *et al* (1985), given by:

$$V_P = 1.16 V_S + 136.0 \quad \text{(m/s)} \qquad (4.14)$$

4.4.2 P-wave velocity-clay content relationship

Figure 4.18 shows the measured relationship between P-wave phase velocity and clay content corresponding to the eight control sandstone samples from WOSPP under dry condition (section 4.1). The porosity values for LU sandstones are between 20.4% and

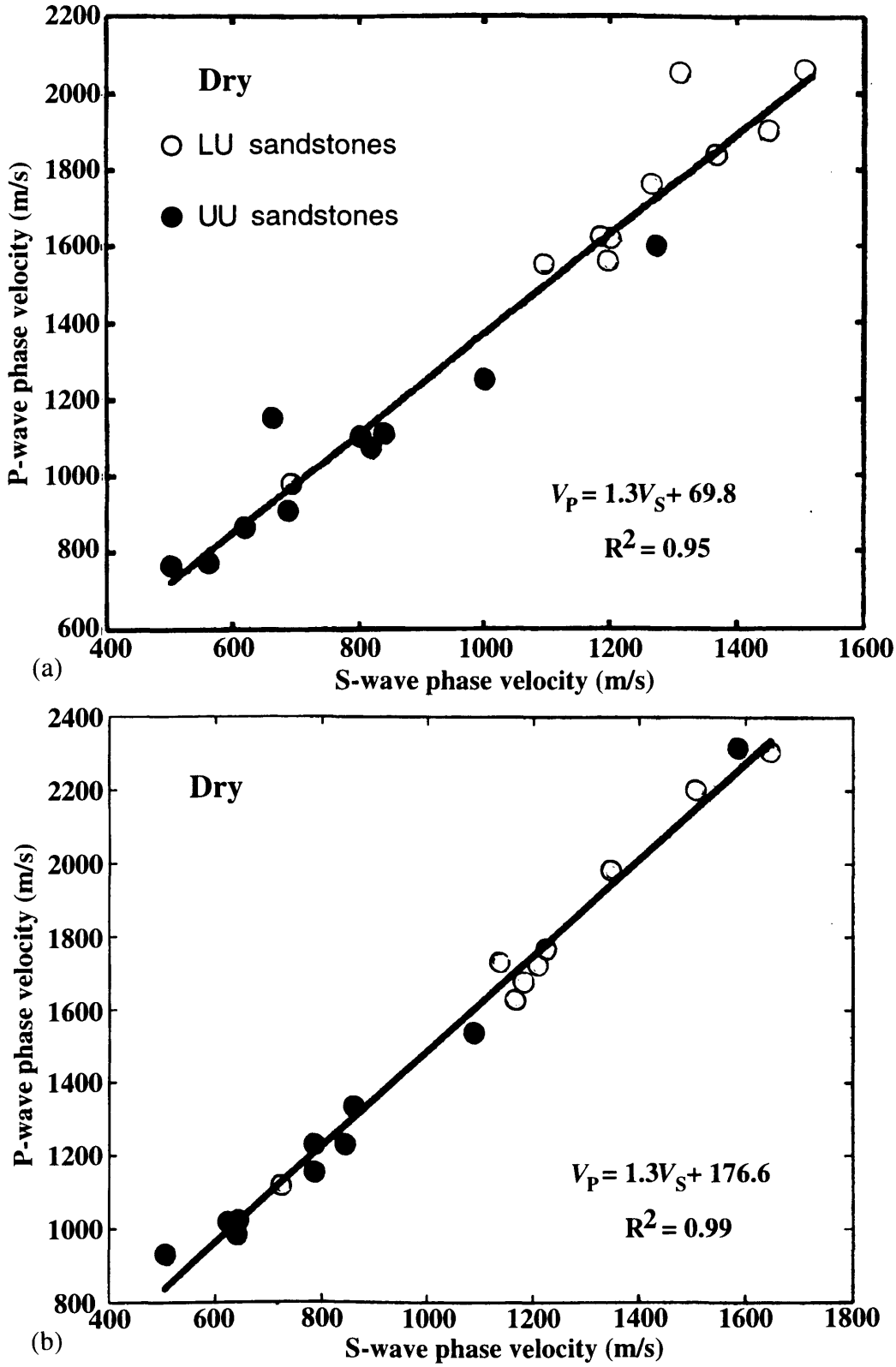

Fig. 4.17 Relationship between P- and S-wave phase velocities under dry conditions: (a) for propagation along Z direction; (b) for propagation along X direction. The linear fit using least-squares method is indicated for both cases.

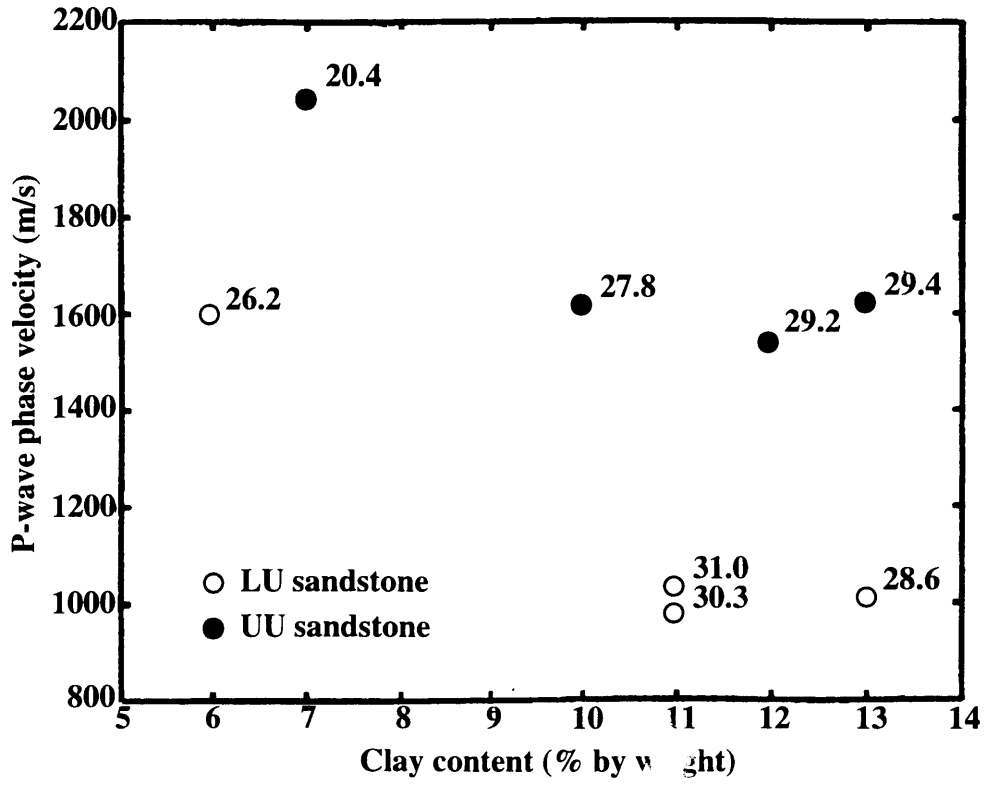

Fig. 4.18 P-wave phase velocity-clay content relationship for LU and UU control sandstone samples. The porosity values are indicated for each sample point.

29.4% and for UU sandstones between 26.2% and 31.0%. From this graph is observed that P-wave velocity for both sandstones decreases with increasing clay content. It follows the general behavior observed by other authors (Castagna *et al.*, 1985; Han *et al.*, 1986; Han, 1987; Klimentos and McCann, 1990; Akbar *et al.*, 1993; Best *et al.*, 1994) that the principal effect of clay contents is to reduce the velocity values for P and S waves.

4.4.3 P- and S-wave velocity-porosity relationships

Figure 4.19 shows the relationships among P- and S-wave phase velocities and porosity under water-saturated conditions along X, Y and Z directions. Although the level of scattering in these data is significant, a linear trend for velocity versus porosity is observed. This trend indicates that P- and S-wave phase velocities decrease with increasing porosity as reported by other authors (Castagna *et al.*, 1985; Han *et al.*, 1986; Han, 1987; Klimentos and McCann, 1990; Klimentos, 1991). The correlations between P- and S-wave velocities and porosity, as determined by least-squares fit, are:

$$V_P(m/s) = (3678.1 \pm 2.2) - (57.3 \pm 0.08)\phi \text{ (m/s)} \quad (4.15)$$

$$V_S(m/s) = (3498.5 \pm 4.7) - (96.3 \pm 0.2)\phi \text{ (m/s)} \quad (4.16)$$

with correlation factors of 0.59 and 0.54, respectively. The number of data points for S wave is very limited as was discussed in the sub-section 4.3.5.

4.4.4 Effect of the saturant fluid on the P-wave phase velocity anisotropy

The experimental relationships between the measured compressional-wave velocities along the X, Y and Z directions under dry conditions at atmospheric pressure and at a frequency of 1.0 MHz are shown in Figure 4.20. From the analysis of Figures 4.20a and 4.20b it is observed that P-wave phase velocity data points represent a linear trend which indicates that the majority of the LU and UU sandstones present an anisotropic behavior like transverse isotropy (TI). In fact, the data point distribution is

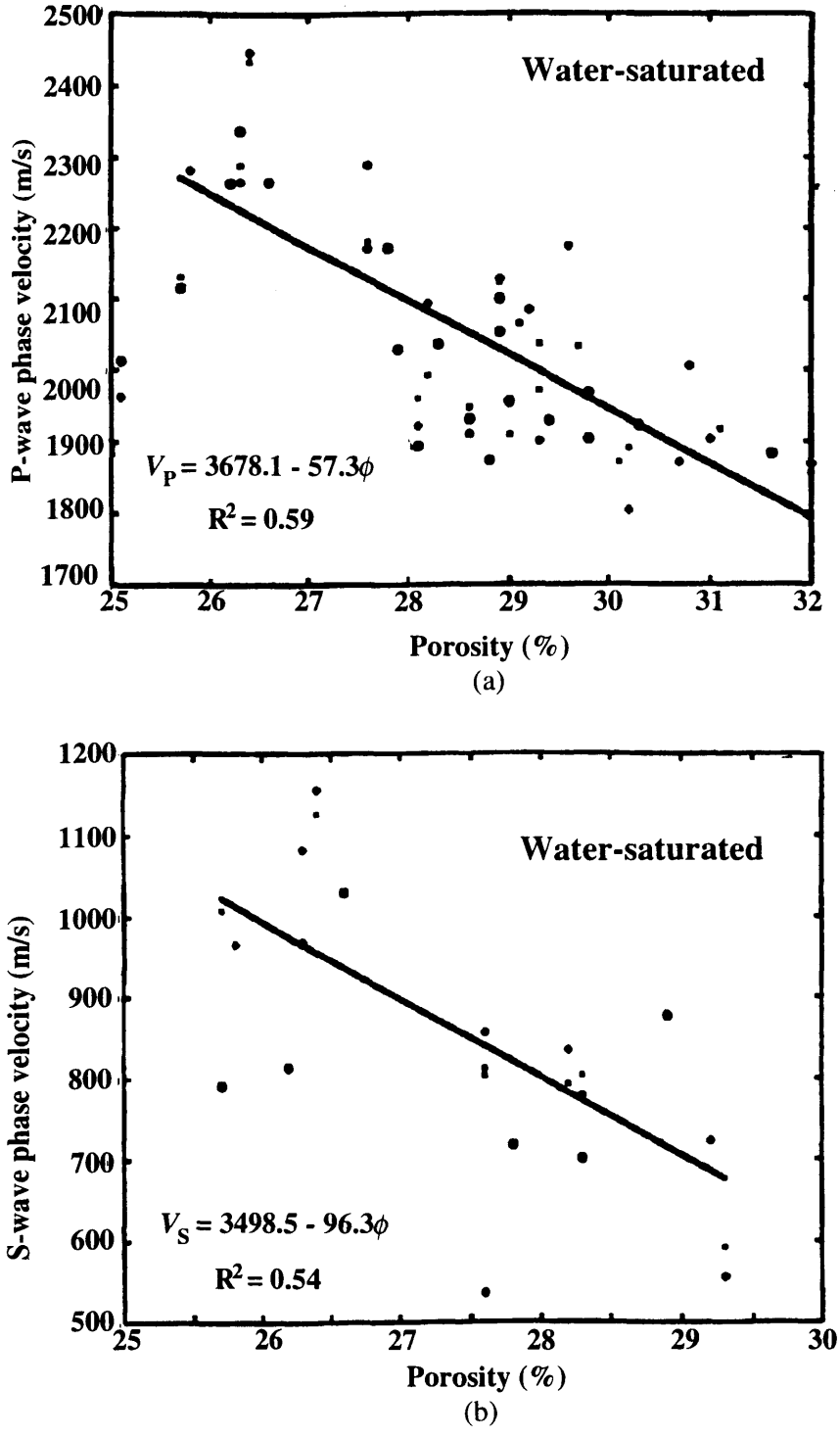

Fig. 4.19 Phase velocity-porosity relationships for: (a) P waves and (b) S waves. All measurements were made under water-saturated conditions. For P wave are considered all samples while for S wave only those samples with velocity information. The different symbols in both graphs represent the P and S-wave phase velocities measured along the three orthogonal directions X, Y and Z as indicated by the solid square, the solid rhomb and the solid circle, respectively. The predicted P and S-wave velocities as a function of the porosity are given by the solid line (linear least-squares fit).

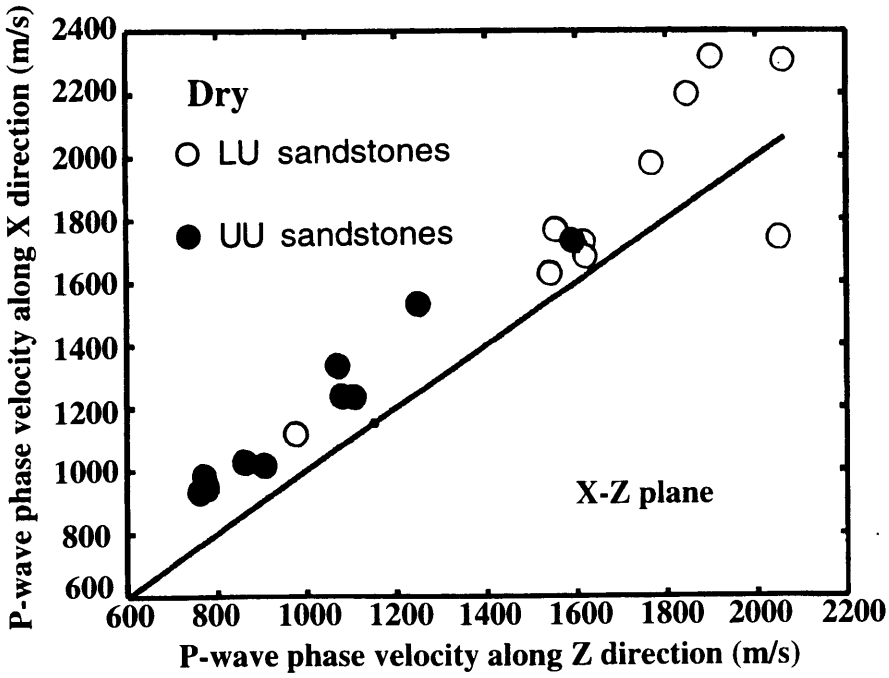

(a)

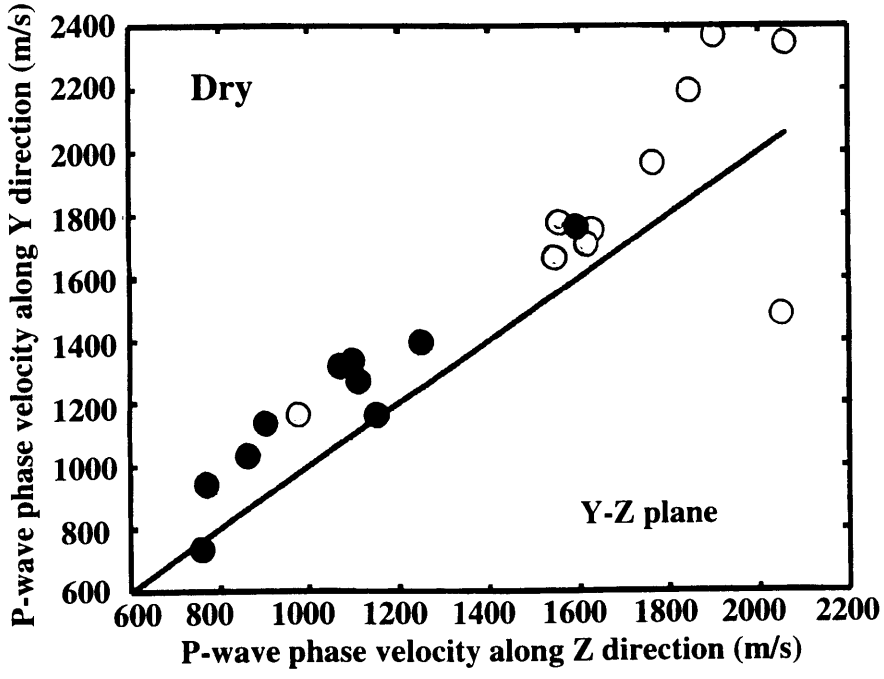

(b)

Fig. 4.20 Relationship between the measured P-wave velocities: (a) in X-Z plane; (b) along Y-Z plane. All measurements under dry conditions. The solid line indicates the case when both velocities are equal (velocity isotropy).

above the solid line, which indicates the isotropic case, due to the fact that the P-wave velocity values measured along X direction are higher than the corresponding P-wave velocity values measured along Z direction (Figure 4.20a). A similar conclusion is obtained from the analysis of the behaviors of P-wave velocities along Y and Z directions as indicated in Figure 4.20b. If the samples were all TI then these two plots should be identical because the measured P-wave velocity along X and Y directions are equal for a TI material (Figure 2.5), but they are similar.

The compressional-wave phase velocities for the sixty sandstone samples under water-saturated condition at atmospheric pressure and at a frequency of 1.0 MHz are indicated in Table 3. Figure 4.21 shows the effect of the saturant fluid on the P-wave phase velocities measured along the three orthogonal directions X, Y and Z. It is evident that for most of the samples the fluid almost causes the observed P-wave velocity anisotropy observed under dry condition to disappear, *i.e.* these samples are more nearly elastically isotropic under saturated conditions. However, some of these samples show an even stronger velocity anisotropy under water-saturated conditions than observed under dry conditions. This effect was reported by Mavko and Mukerji (1992) for anisotropic rocks with cracks (section 2.6). Both authors found that velocities and velocity anisotropy may or may not change between dry and saturated conditions. The fluid saturation sometimes increases anisotropy and sometimes decreases it, depending on the rock, the stress state, and the frequency used in the laboratory (Mavko and Mukerji, 1992). In the case of the sandstone samples of WOSPP the effect of the fluid saturation is to decrease the original velocity anisotropy observed in these samples under dry conditions.

4.4.5 P-wave phase-velocity permeability relationships

Figure 4.22a shows the experimental results obtained for P-wave phase velocity versus permeability for only the eight control sandstone samples. It is evident that there are two different velocity-permeability trends for the LU and UU sandstone samples: (i) a linear trend labeled PDV which indicates that P-wave velocity decreases with increasing permeability, and (ii) a linear trend labeled NPDV which shows that P-wave velocity has no dependence on permeability. Although the data displayed in Figure 4.22a are limited,

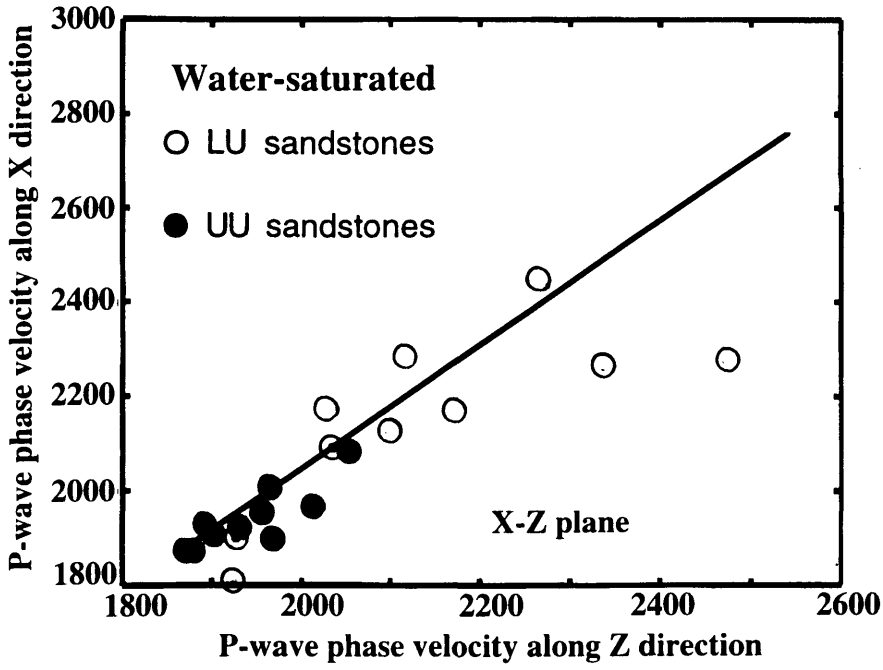

(a)

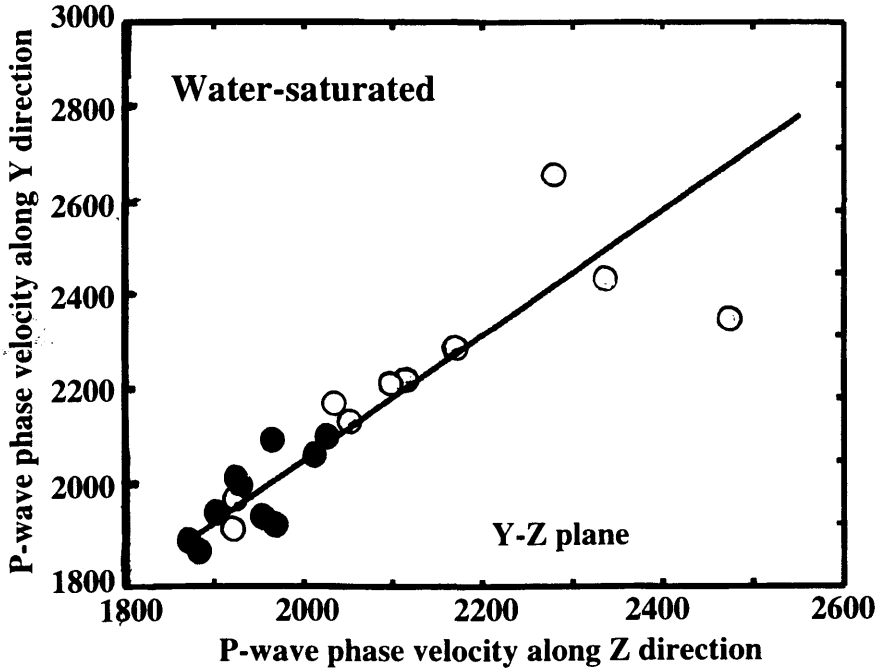

(b)

Fig. 4.21 Relationship between the measured P-wave velocities: (a) in X-Z plane; (b) along Y-Z plane. All measurements under water-saturated conditions. The solid line indicates the case when both velocities are equal (velocity isotropy).

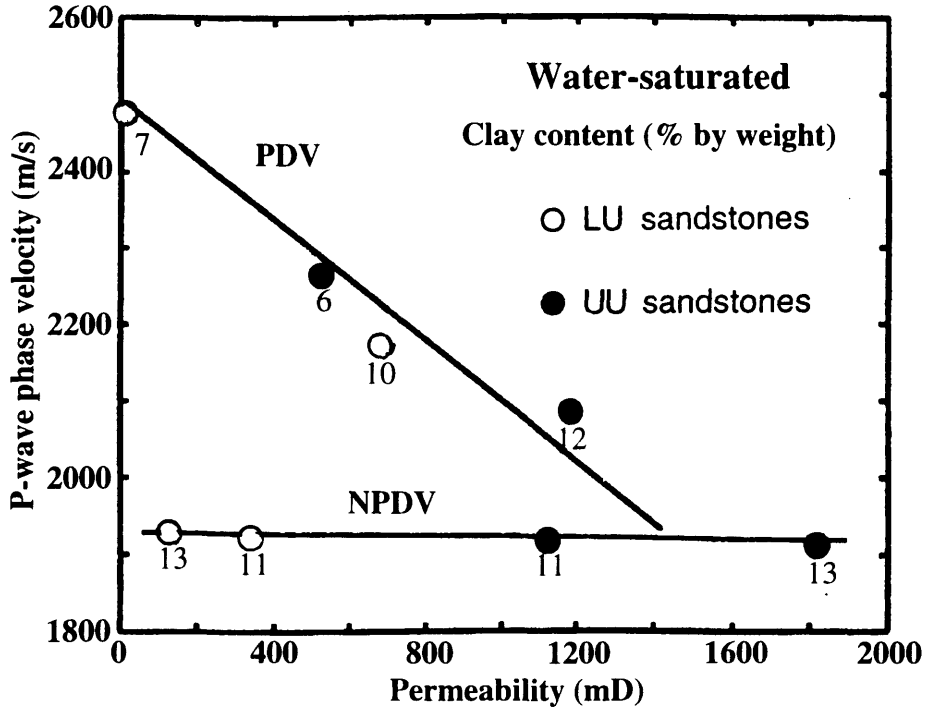

(a)

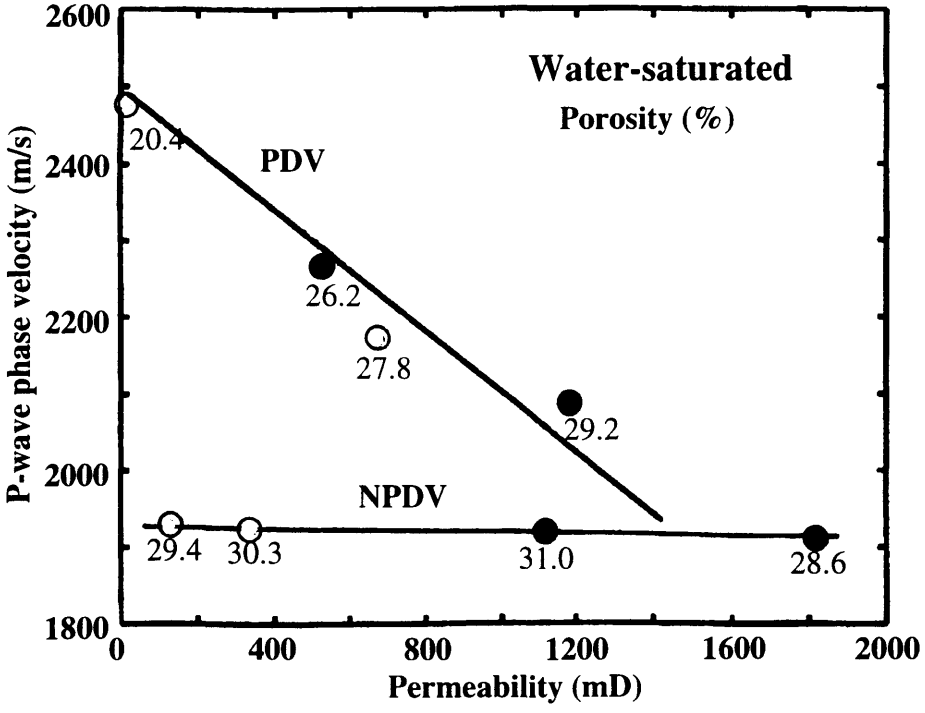

(b)

Fig. 4.22 P-wave phase velocity-permeability relationship: (a) with clay content values; (b) with porosity values. All the measurements under water-saturated conditions. The label PDV represents the permeability-dependent velocity trend, while the label NPDV represents the non permeability-dependent velocity curve. The data points represent the eight control sandstone samples.

they indicate that the PDV linear trend presents a relative wide clay content range between 6% and 12%, while the NPDV trend has associated clay content values between 11% and 13%. This last mentioned behavior of P-wave velocity versus permeability has been reported by many authors (*e.g.*. Best *et al.*, 1994 and Klimentos, 1994) as indicated in Figure 2.17. On the other hand, Figure 4.22b shows the porosity values associated with the data plotted in Figure 4.22a and indicates that, for porosity values higher than 29.0%, the P-wave velocity does not depend on permeability.

The fact that the PDV trend presents a range of porosity values between 20.4% and 29.2% and clay content values between 6% and 12%, suggests the possibility that observed effect of permeability on P-wave velocity, represented by the PDV trend, is due to the velocity-clay content and velocity-porosity relationships. Klimentos (1991) showed that the effect of permeability alone on P-wave velocity is negligible in sandstones with negligible (<1%) or identical clay content, identical porosity, lithology, and other petrophysical properties (*e.g.*, grain-size and sorting, pore-size and shape, etc.) and concluded that the observed P-wave velocity-permeability dependence on his sandstone samples arises mainly from the velocity-clay content and clay-content permeability interrelations.

The P-wave-velocity permeability observations for the sixty sandstone samples is presented in Figure 4.23. Here one may see both the PDV and NPDV trends referred to above, but the NPDV trend now shows a very fast decay of P-wave velocity versus permeability for permeability values less than about 250 mD (Figure 4.23). This indicates the existence of some critical permeability, above which P-wave velocity does not depend on permeability. From this it is possible to surmise that the PDV linear trend observed in Figure 4.23 has associated with it a critical permeability of about 1500 mD.

Although, S-wave velocity data is very limited due to the high attenuation of the S waves under water-saturated conditions for the sandstone samples from WOSPP, which makes it impossible to determine accurate first-zero-crossover traveltimes for these kind of waves, it is evident that S-wave velocity shows a more significant dependence on permeability than P-wave phase velocity, for permeability values above about 200 mD. In

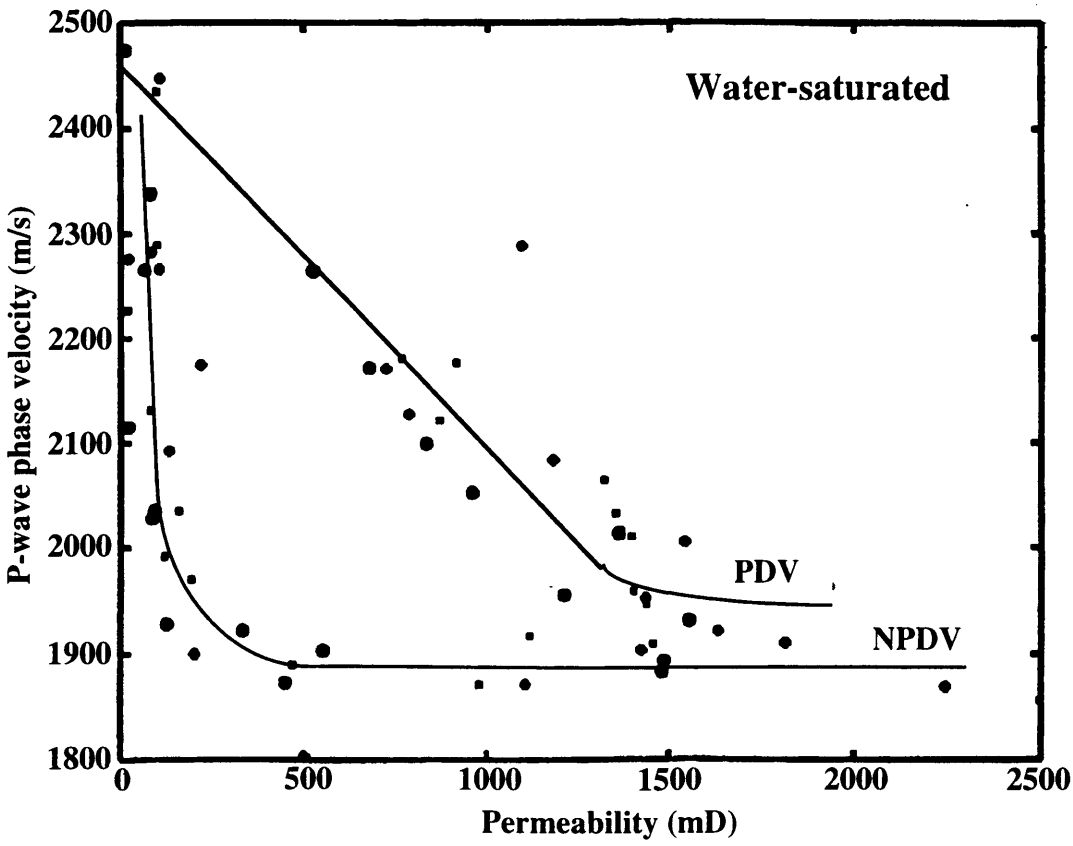

Fig. 4.23 P-wave phase velocity as a function of permeability for all the sandstone samples from WOSPP. The different symbols in this graph represent the P-wave velocities measured along three orthogonal directions X, Y and Z shown by the solid square, the solid rhomb and the solid circle, respectively. The curves PDV and NPDV were defined without any mathematical fit method. All the measurements were made under water-saturated conditions.

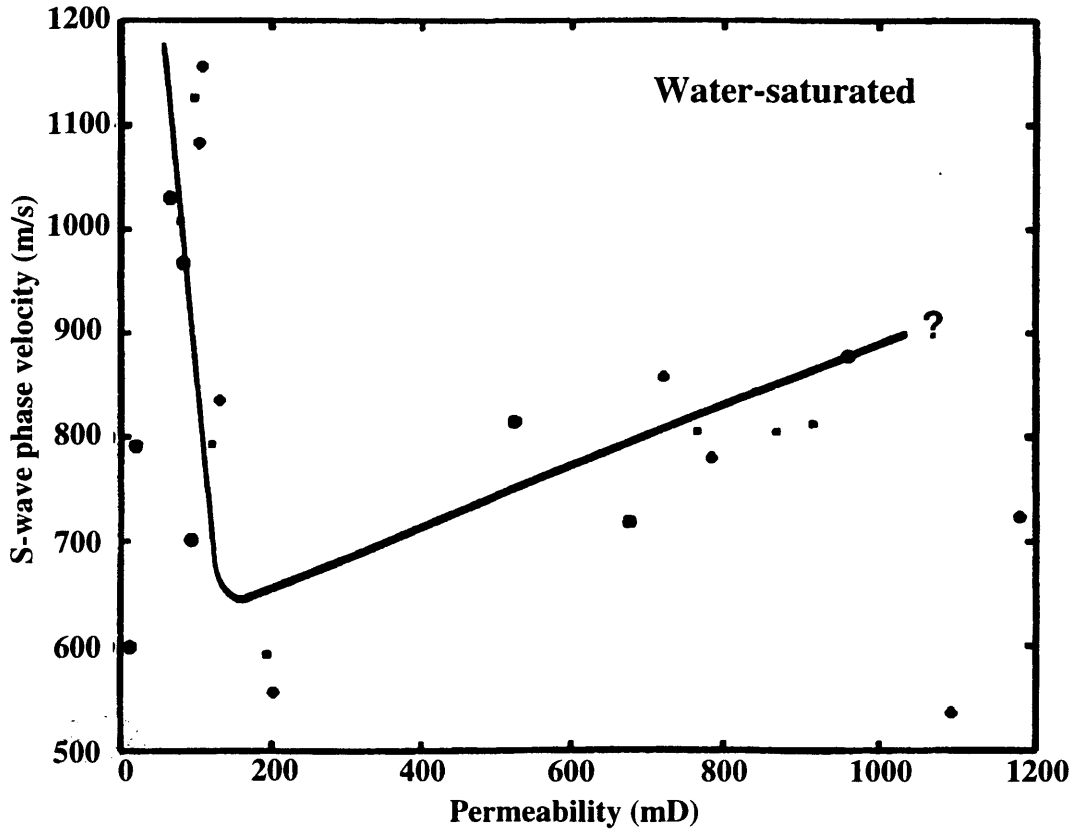

Fig. 4.24 S-wave phase velocity as a function of permeability for some sandstone samples from WOSPP. All the measurements were made under water-saturated conditions. The symbol code is the same than used in Figure 4.23. The curve was traced without any mathematical fit method. It is observed certain trend that indicates that S-wave phase velocity increases with permeability, as opposite to P-wave phase velocity.

fact, S-wave phase velocity apparently increases with increasing permeability for permeability values between 500 mD and 1000 mD (Figure 4.24). This effect is not observed for P-wave velocity data for the same permeability range, which shows a decaying and constant dependence on permeability (Figure 4.23).

4.5 Relationships among P- and S-wave attenuation, clay content, and porosity

Figure 4.25 shows the relationship between the measured values of compressional-wave attenuation coefficient a_P and shear-wave attenuation coefficient a_S under water-saturated conditions. The linear least-squares fit on this data gives a correlation factor of 0.10 which indicates no significant correlation between both parameters for the sandstone samples from WOSPP. On the other hand, it is evident that the S-wave attenuation coefficient is more than four times greater than P-wave attenuation coefficient, which strongly decreases the amplitude of the S waves after propagating across these water-saturated sandstone samples.

4.5.1 P- and S-wave attenuation-permeability relationships

Figure 4.26 shows the variation of P-wave attenuation coefficient with permeability for the eight control sandstone samples (section 4.1) with clay content of 12 ± 1% under water-saturated condition. The porosity range for LU sandstones is between 27.8% and 29.4% and between 29.0% and 31.0% for UU sandstones. It is evident that the P-wave attenuation coefficient increases with increasing permeability for these sandstones.

The measured attenuation coefficient for P waves versus permeability along the three orthogonal directions (X, Y and Z) for the sixty sandstone samples under water-saturated condition is shown in Figure 4.27. Although the level of scattering is significant, it is evident that there is a tendency for P-wave attenuation coefficient to increase when permeability is increased above about 300 mD. Based on limited data, Klimentos and McCann (1990) found that the attenuation of rocks with low permeability (<50 mD) due to clay filling the pores can be high, while the attenuation of rocks with medium permeability (50-250 mD) due to medium porosity and clean pores is very low (Figure 2.14). On the other hand, based on only one data point from one sandstone sample, they

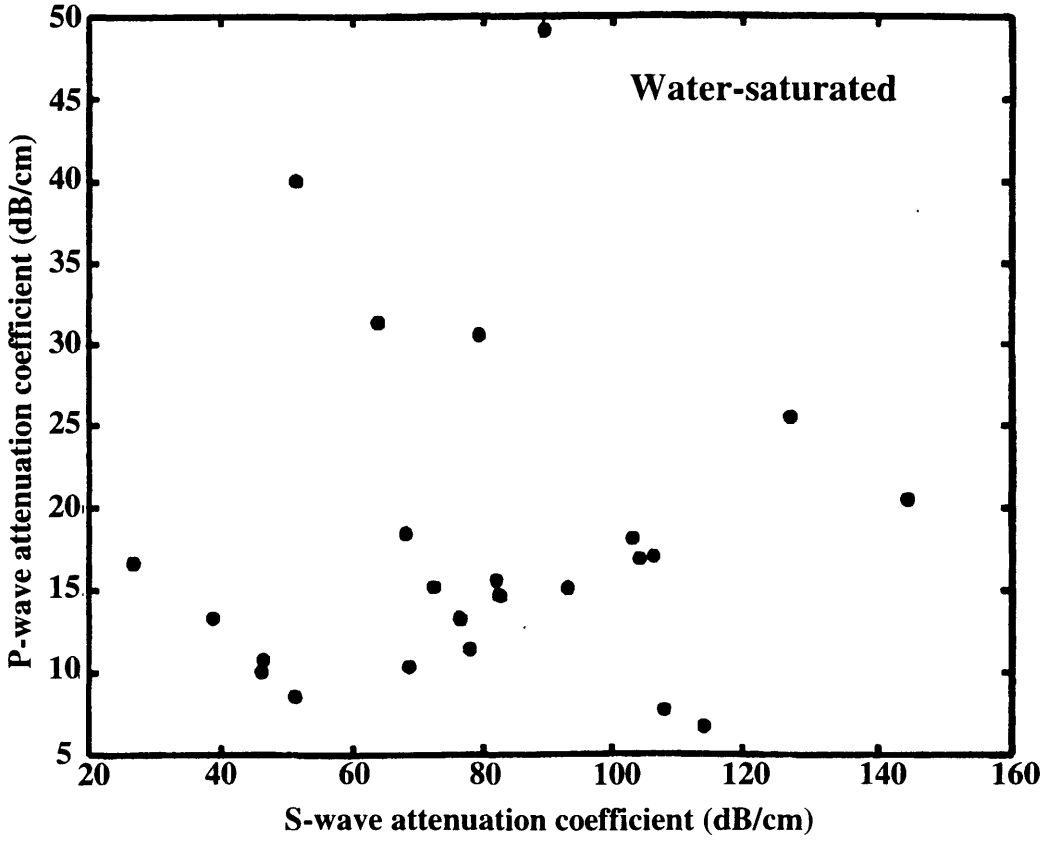

Fig. 4.25 Ultrasonic data obtained from 20 water-saturated sandstone samples from WOSPP. This data shows P-wave attenuation coefficient *versus* S-wave attenuation coefficient. All measurements were made along Z direction.

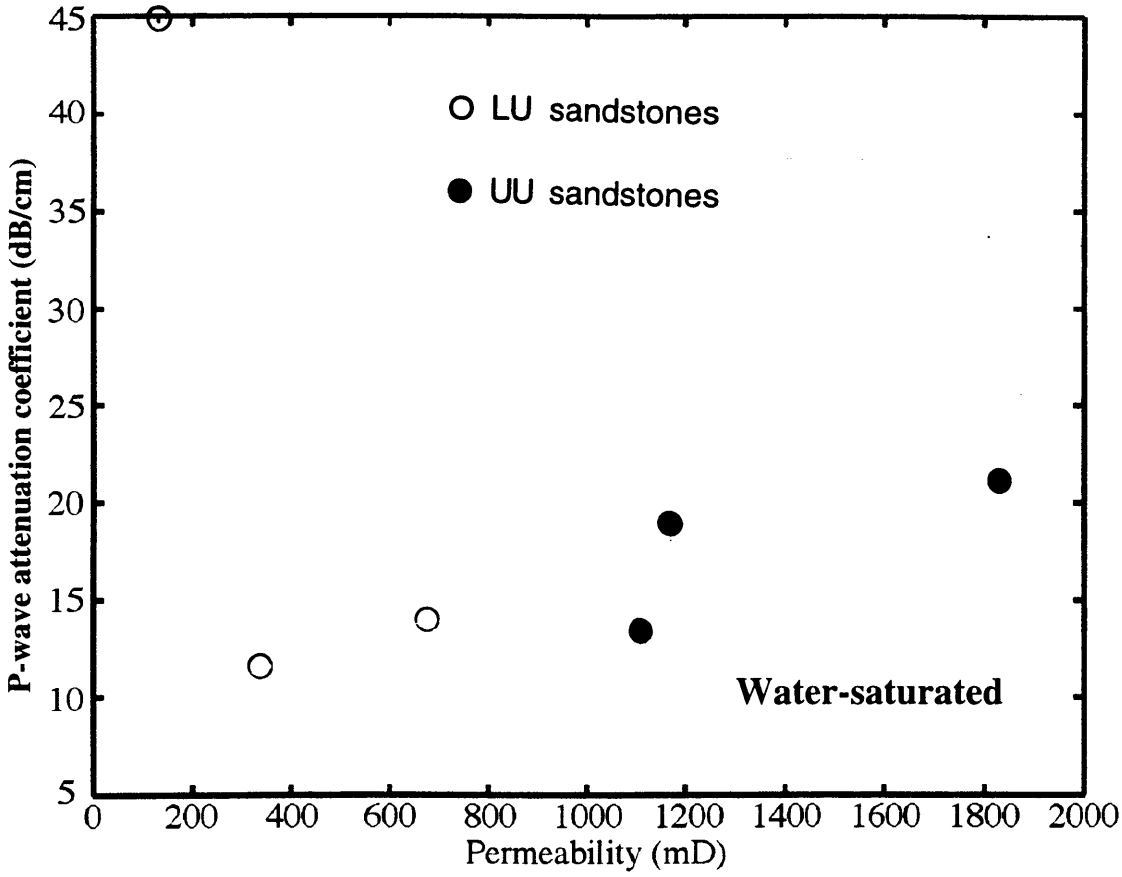

Fig. 4.26 Experimental observations of the attenuation-permeability relationship for LU and UU sandstones, considering a constant clay content value. All the measurements under water-saturated conditions.

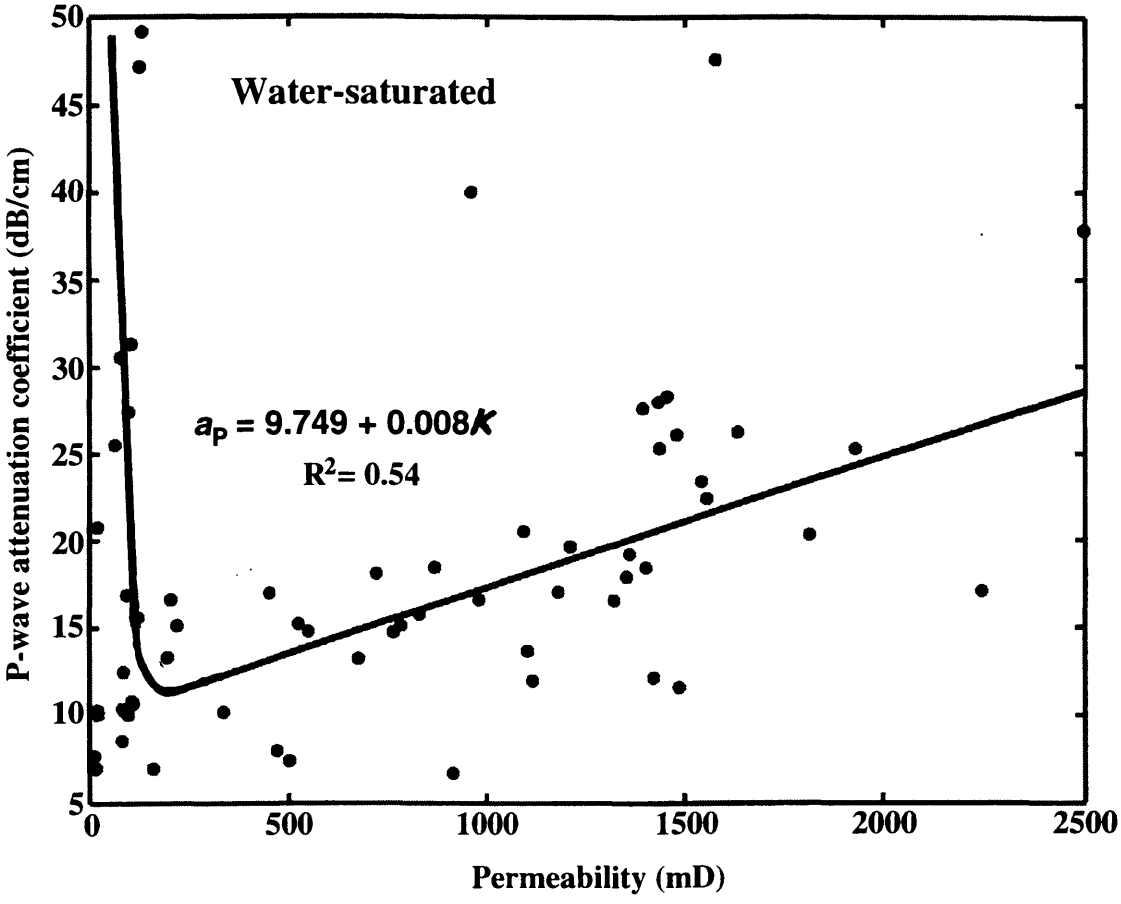

Fig. 4.27 P-wave attenuation coefficient *versus* permeability for all the sandstone samples from WOSPP. All the measurements were made under water-saturated conditions. The linear least-squares fit of the P-wave attenuation coefficients were calculated between 250 and 2500 mD. It is evident an increment in P-wave attenuation coefficient when the permeability is increased beyond 300 mD.

concluded that the attenuation of a high-permeability rock (>300 mD) may be quite high, as indicated in Figure 2.14.

The experimental data shown in Figure 4.27 are in agreement with the results obtained by Klimentos and McCann (1990). Additionally, from Figure 4.27, one can see that the P-wave attenuation coefficient roughly doubles for a permeability of 1500 mD as compared with 100 mD.

The S-wave attenuation coefficient *versus* permeability is shown in Figure 4.28. Although S-wave data is more limited than P-wave data, the above described behavior is also observed on S-wave data showing an increment in shear-wave attenuation coefficient when permeability is increased above 200 mD. The best linear least-squares fit are:

$$a_P = (7.54 \pm 0.22) \cdot 10^{-3} k + (9.75 \pm 0.24) \quad \text{(dB/cm)} \tag{4.17}$$

$$a_S = (78.1 \pm 0.99) \cdot 10^{-3} k + (21.98 \pm 0.78) \quad \text{(dB/cm)} \tag{4.18}$$

and correlation factors of 0.54 and 0.56, respectively.

4.5.2 P- and S-wave attenuation-porosity relationships

The effect of porosity on P-wave attenuation coefficient under dry condition along Z direction is shown in Figure 4.29a. It is evident that P-wave attenuation coefficients for both LU and UU sandstones shows a slightly increment with increasing porosity. Only one data point for UU sandstones with porosity of 31.0 percent shows an abnormal attenuation coefficient (Figure 4.29a). Same conclusion is obtained for the relationship between attenuation and porosity along X direction (Figure 4.29b). These experimental results are in general agreement with the results obtained by Klimentos and McCann (1990) as indicated in Figure 2.13a. For a fixed range of clay content values, attenuation increases with porosity.

When these sandsttone samples are saturated with water, the P-wave attenuation oefficient increment with porosity is greater along X direction than observed along Z direction (Figure 4.30). In fact, for a porosity range between 28-32%, P-wave attenuation coefficients measured along X direction for the LU sandstones under water-saturated conditions, show values twice greater than those measured along same direction, but

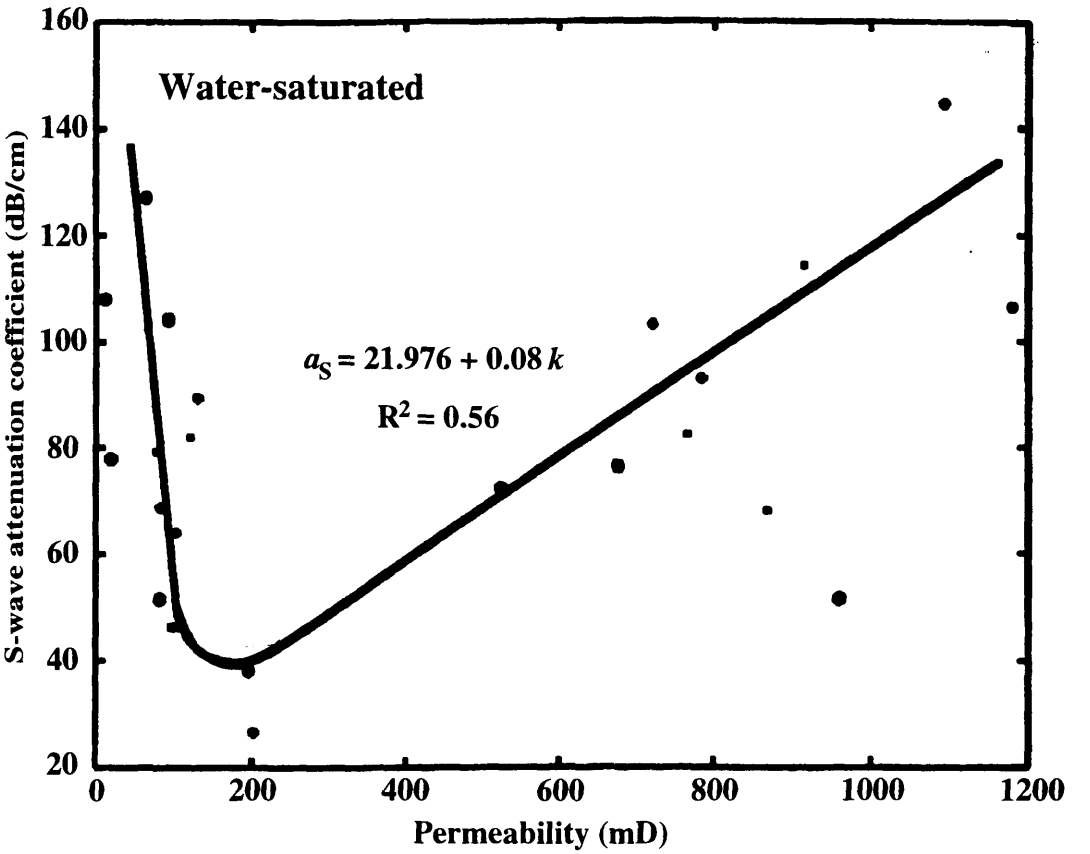

Fig. 4.28 S-wave attenuation coefficient-permeability relationship showing how the shear wave attenuation coefficient increases with permeability beyond about 300 mD. All the measurements under water-saturated conditions. The symbol code is the same than used in Figure 4.23.

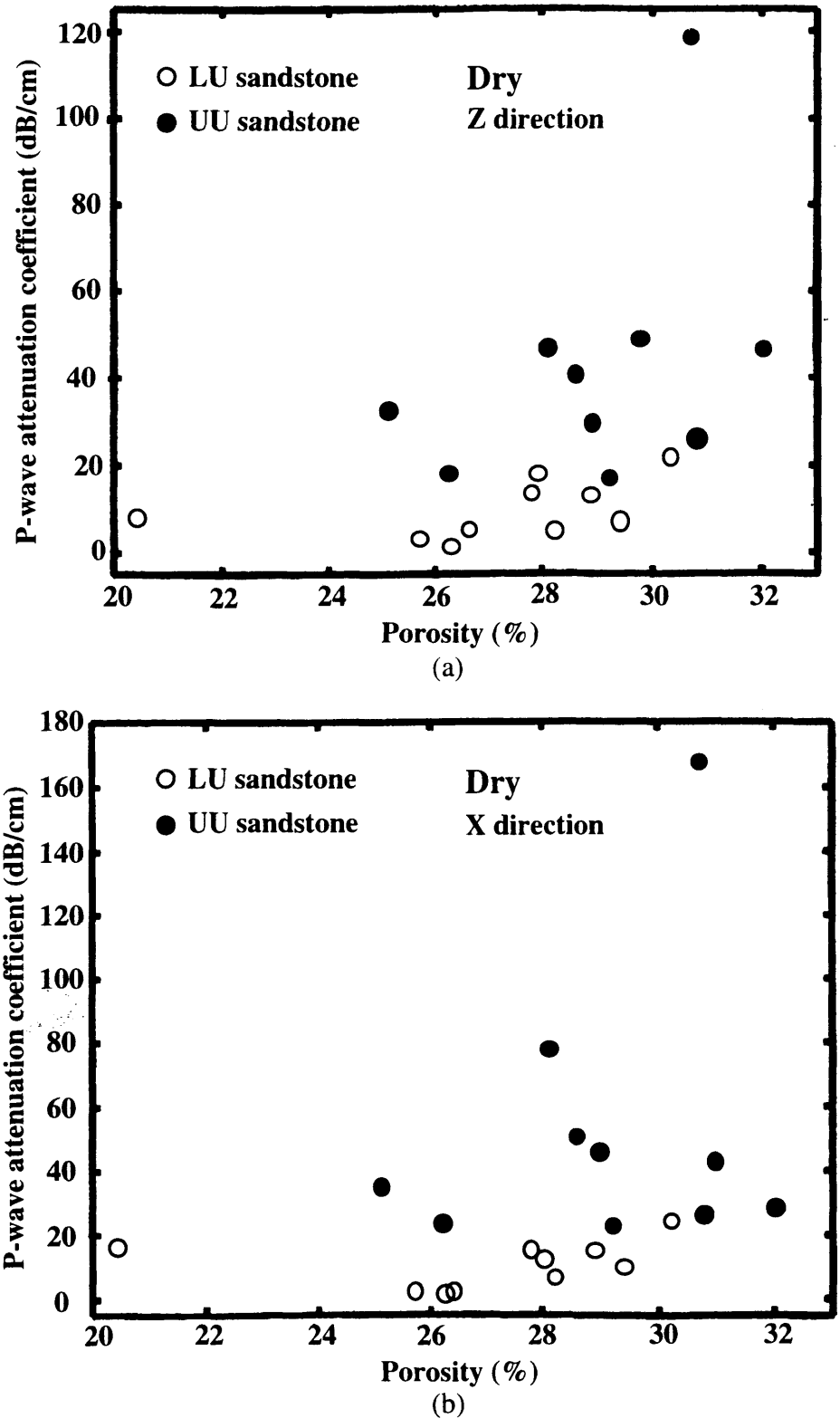

Fig. 4.29 P-wave attenuation coefficient versus porosity: (a) for propagation in Z direction; (b) for propagation in X direction. All the measurements under dry conditions for LU and UU sandstones.

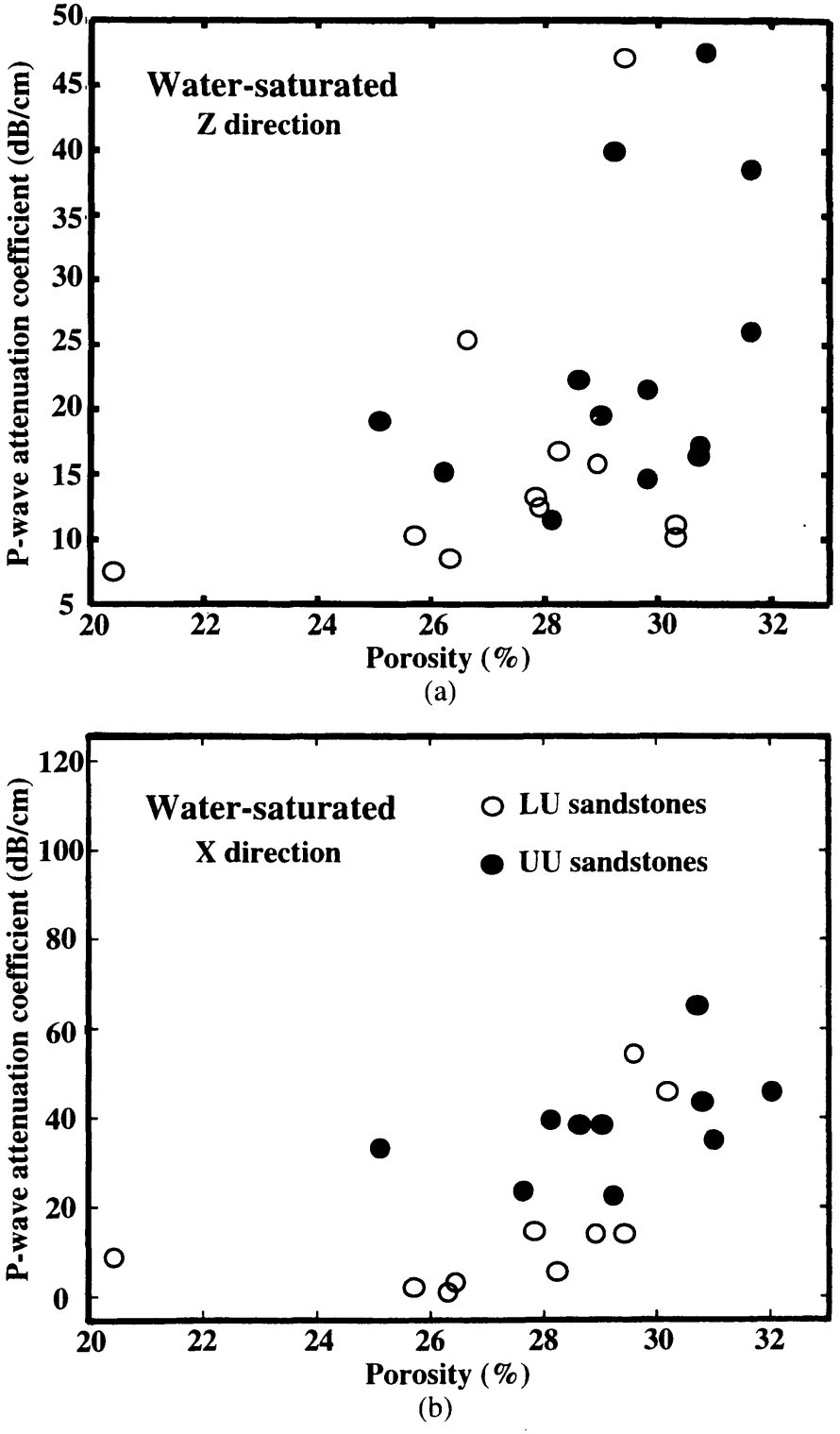

Fig. 4.30 P-wave attenuation coefficient versus porosity: (a) for propagation in Z direction; (b) for propagation in X direction. All he measurements under water-saturated conditions for LU and UU sandstones.

under dry conditions (Figures 4.29b and 4.30b). In contrast, the UU sandstones apparently not shows a significant increment in their P-wave attenuation values after saturating they with water (Figures 4.29a and 4.30a). In each case, this increment of P-wave attenuation with porosity is lower than associated with permeability.

4.5.3 Effect of saturant fluid on P- and S-wave attenuation coefficient anisotropy

The effect of the saturant fluid on the P-wave attenuation coefficient is shown in Figure 4.31b. Under dry conditions the P-wave attenuation coefficient values are close to the solid line which indicates that the measured attenuation along Z direction is equal to the measured attenuation along X direction (Figure 4.31a). In contrast, the P-wave attenuation coefficient shows a more anisotropic behavior under water-saturated condition as represented by the high scattering of the attenuation coefficient values around the solid line (Figure 4.31b). A similar result is obtained along Y direction after comparing Figures 4.32a and 4.32b under dry and water-saturated conditions, respectively.

Then, unlike the observed effect of the saturant fluid on P-wave, the P-wave attenuation coefficient presents more anisotropy after all the sandstone samples are saturated with water. This observation suggests the possibility that the attenuation introduced by the fluid saturant is bigger than corresponding attenuation caused by the matrix of the sandstone sample.

4.5.4 Relating velocity and attenuation anisotropy for P waves with permeability anisotropy

Gelinsky and Shapiro (1994a, b; 1995) expressed some theoretical relationships among velocity, attenuation coefficient and permeability for P, SV and SH waves for a homogeneous, isotropic, liquid-saturated porous media having permeability anisotropy at low frequency range (section 2.5). After analyzing the P-wave phase velocity values for LU and UU sandstones under water-saturated condition (Figure 4.21) it can be concluded that these sandstones are generally velocity isotropic when a fluid (water) fills its pores in

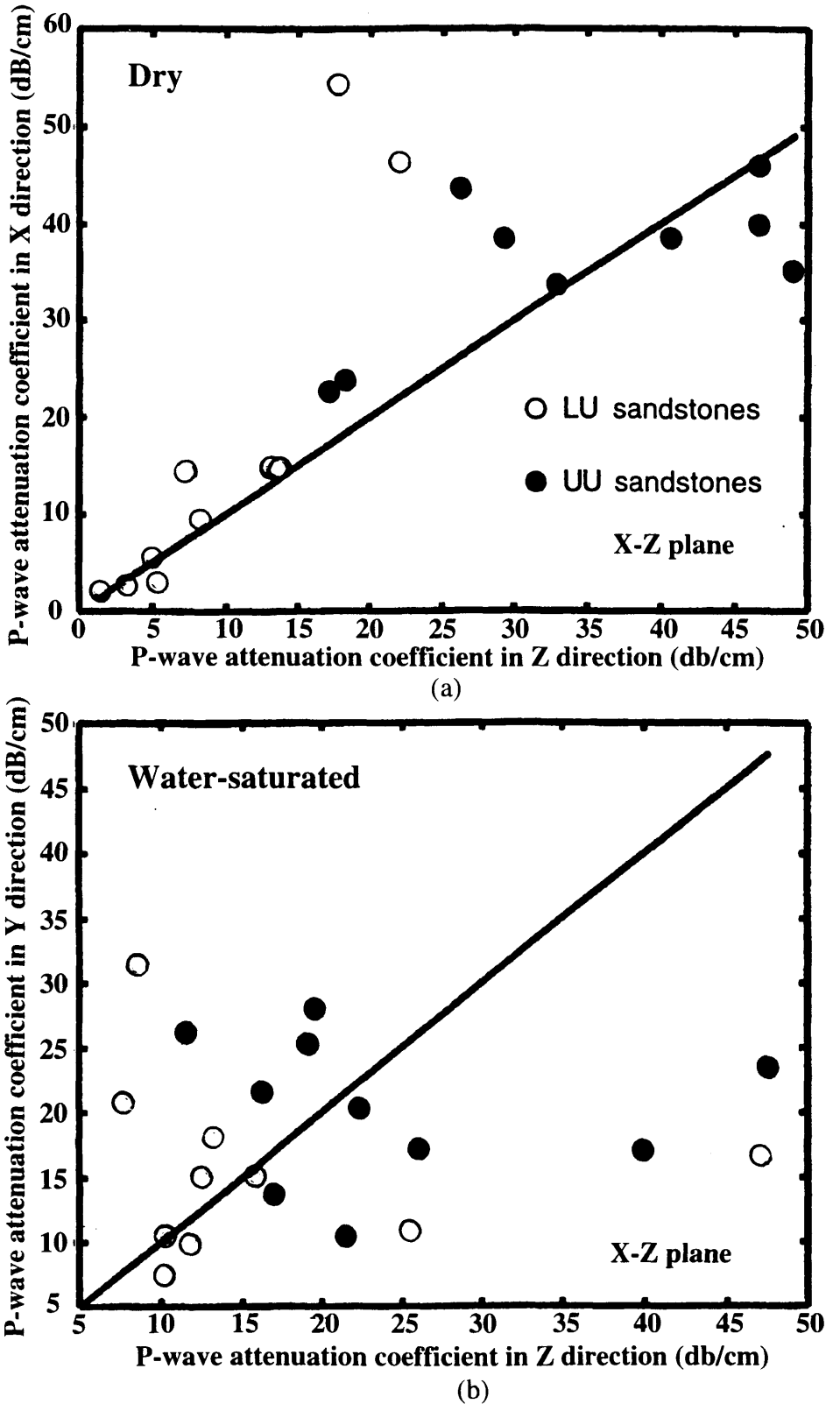

Fig. 4.31 Relationship between P-wave attenuations along X and Z directions: (a) dry; (b) water-saturated. In both cases the solid line indicates the case when the attenuations are equal for both directions of propagation (attenuation isotropy).

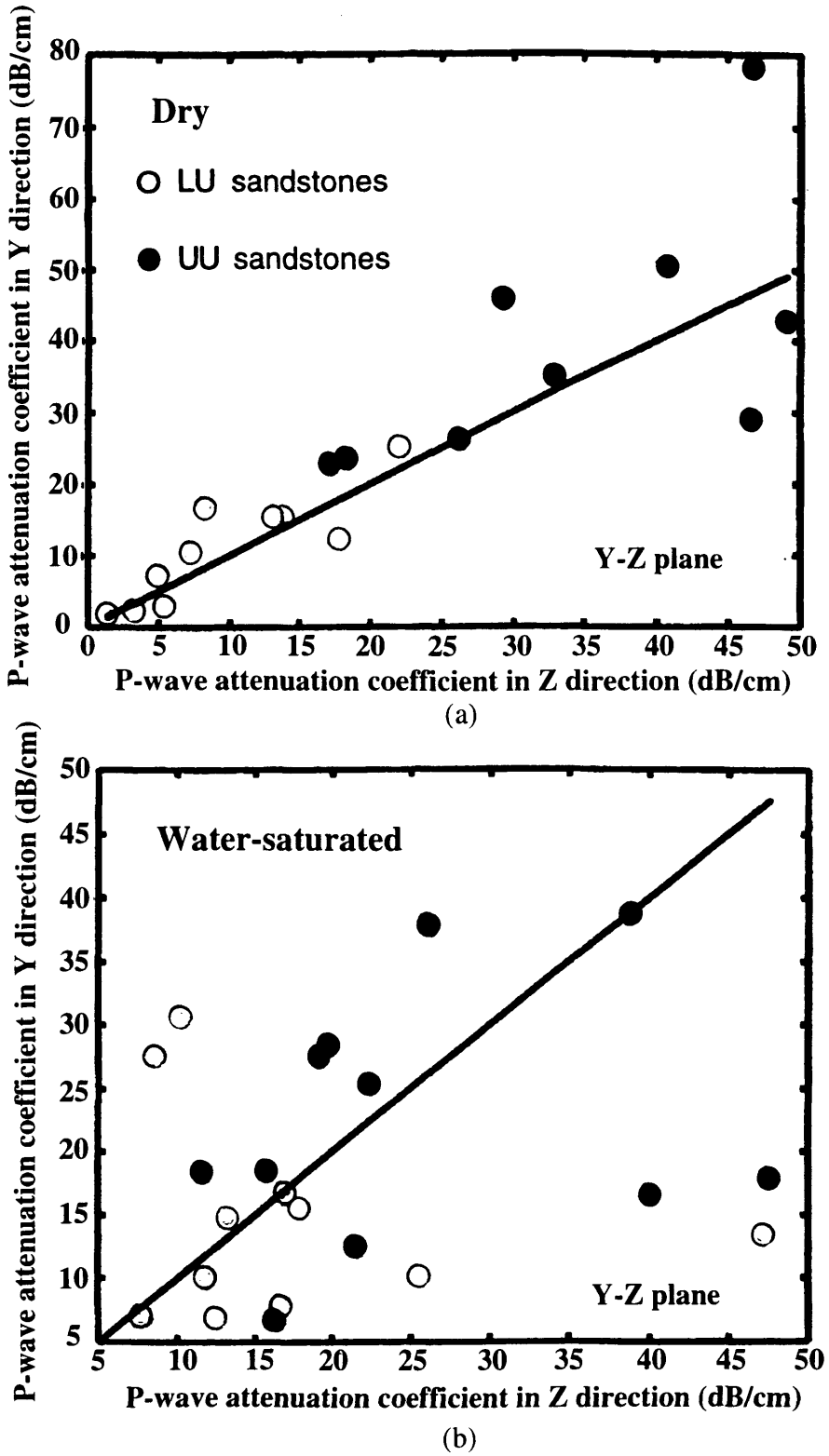

Fig. 4.32 Relationship between P-wave attenuations along X and Z directions: (a) dry; (b) water-saturated. In both cases the solid line indicates the case when the attenuations are equal for both directions of propagation.

the sense that they obey one of principles established in the theory presented by Gelinsky and Shapiro (1994a, b; 1995). Here it will be assumed that the frequency range used during velocity and attenuation measurements for P and S waves just presented is valid for applying those theoretical aspects. Then, from eq. (2.46), established by Gelinsky and Shapiro (1994a, b; 1995) for the attenuation coefficient of P waves as function of permeability anisotropy, it is expected that the ratio between the measured P-wave attenuation coefficient parallel to the vertical direction, divided by the P-wave attenuation coefficient measured perpendicular to this direction will be proportional to the ratio of the permeabilities measured along both directions:

$$\frac{a_P\left(\theta = 0^\circ\right)}{a_P\left(\theta = 90^\circ\right)} = C\frac{k_{\parallel}}{k_{\perp}} \tag{4.19}$$

where θ is the angle of propagation of the P wave with respect to the vertical axis (Z axis), C is a constant, a_P is the P-wave attenuation, and $k_{\parallel}$ and $k_{\perp}$ are the permeabilities measured parallel and perpendicular to the vertical axis, respectively.

In this way is possible to relate attenuation anisotropy with permeability anisotropy. Figures 4.33 and 4.34 shows the measured P-wave attenuation and permeability anisotropies along X, Y and Z directions under water-saturated conditions. Based on this limited data a very interesting result is obtained about the behavior of the P-wave attenuation anisotropy in Y-Z plane indicating the presence of two trends: (i) a trend labeled I which indicates that P-wave attenuation anisotropy linearly increases with permeability anisotropy values between 0.2 and 0.7 as indicated in eq. (4.18). Also, it shows that for permeability anisotropy values higher than 0.7, P-wave attenuation anisotropy apparently not depend s on permeability anisotropy, as supported by a data point at a permeability anisotropy value around of 1.15 (Figure 4.33), and (ii) a trend labeled II, characterized by low P-wave attenuation anisotropy values, permeability anisotropy values between 0.7 and 1.2, and no significant dependence between P-wave

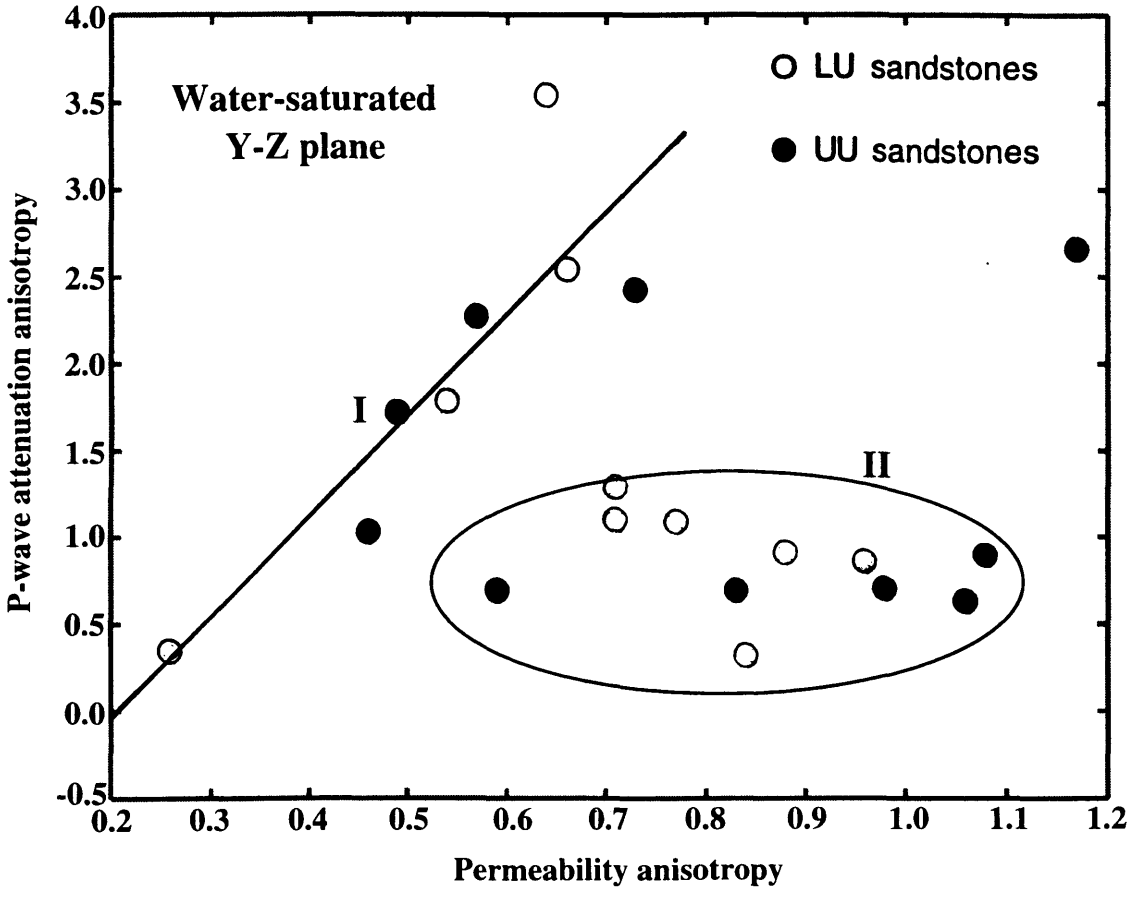

Fig. 4.33 P-wave attenuation anisotropy *versus* permeability anisotropy for sandstone samples from WOSPP. All the measurements were made in the Y-Z plane and under water-saturated conditions. The dependence predicted by Gelinsky and Shapiro (1995) is observed in the trend labeled I for permeability anisotropy values between 0.2 and 0.7. The cluster II indicates sandstone samples with low P-wave attenuation anisotropy and with not significant dependence on permeability anisotropy.

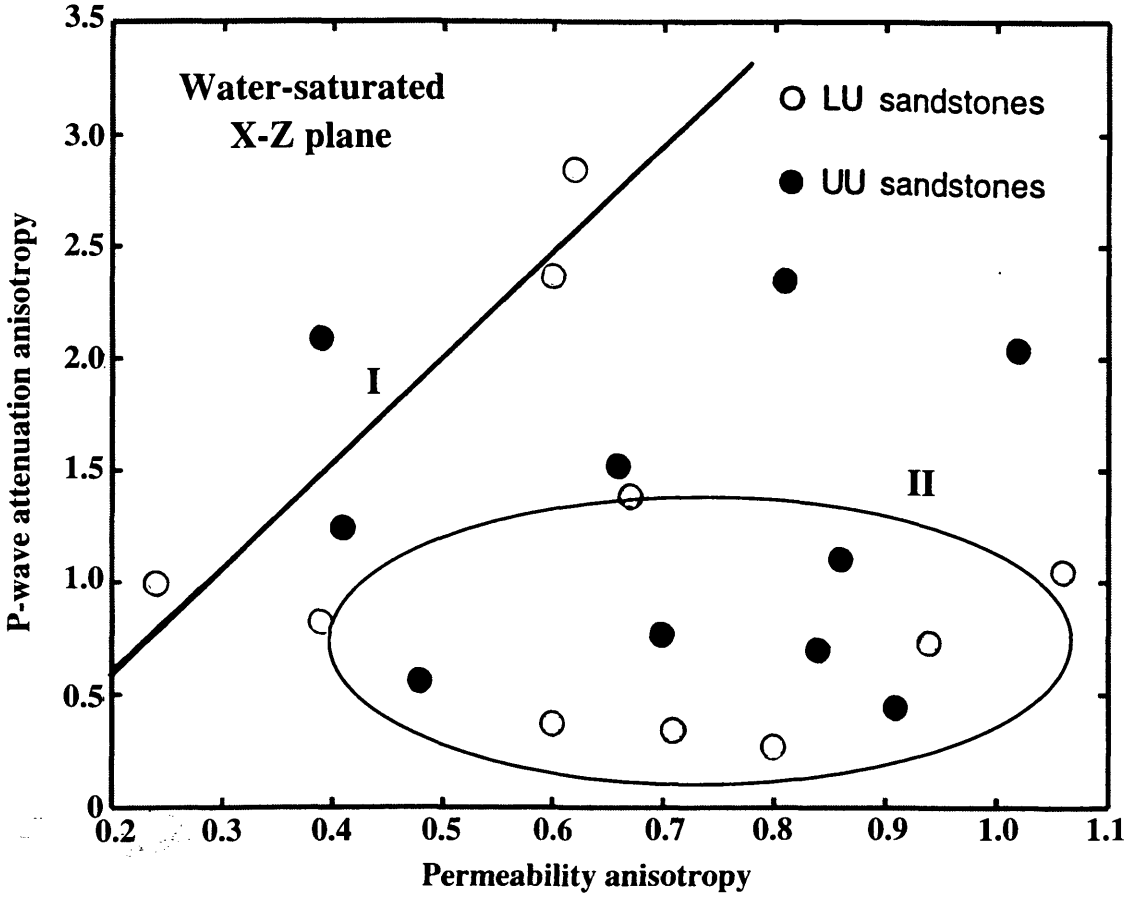

Fig. 4.34 P-wave attenuation anisotropy *versus* permeability anisotropy for sandstone samples from WOSPP. All the measurements were made in the X-Z plane and under water-saturated conditions. The dependence predicted by Gelinsky and Shapiro (1995) is observed in the trend labeled I for permeability anisotropy values between 0.2 and 0.7. The cluster II indicates sandstone samples with low P-wave attenuation anisotropy and with not significant dependence on permeability anisotropy.

anisotropy anisotropy and permeability anisotropy (Figure 4.33). These experimental relations suggests that there is a critical permeability-anisotropy value above which the P-wave attenuation anisotropy is independent on permeability anisotropy. As a result, only the sandstone samples showing strong permeability anisotropy (0.2-0.7), or $k_{\parallel} < k_{\perp}$, are linearly related to attenuation anisotropy. The least-squares fit for the data associated with trend I is:

$$\frac{a_P\left(\theta = 0^\circ\right)}{a_P\left(\theta = 90^\circ\right)} = (5.823 \pm 2.6)\frac{k_{\parallel}}{k_{\perp}} - (1.213 \pm 1.5) \qquad (4.20)$$

with a correlation factor of $R^2 = 0.75$. It reseambles the predicted behavior given by eq. (4.17)

Although the same analysis in the X-Z plane is more vague, due to the significant level of scattering in the data, it is even possible to observe both trends already described (Figure 4.34). For the trend I, with permeability anisotropy values between 0.2 and 0.6, it is again observed a tendency of increasing P-wave attenuation anisotropy with permeability anisotropy as indicated by the corresponding least-squares fit:

$$\frac{a_P\left(\theta = 0^\circ\right)}{a_P\left(\theta = 90^\circ\right)} = (4.725 \pm 3.1)\frac{k_{\parallel}}{k_{\perp}} - (0.364 \pm 1.4) \qquad (4.21)$$

with a correlation factor $R^2 = 0.69$. For permeability anisotropy values beyond 0.6, it is no significant the relationship between P-wave attenuation anisotropy and permeability anisotropy.

A very different picture is obtained from the P-wave velocity anisotropy *versus* permeability anisotropy along X, Y and Z directions (Figures 4.35 and 4.36). P-wave velocity anisotropy is defined by the parameter ε (Thomsen ,1986) which measures the degree of P-wave anisotropy for a TI media (eq. 2.29). From the analysis of both Figures

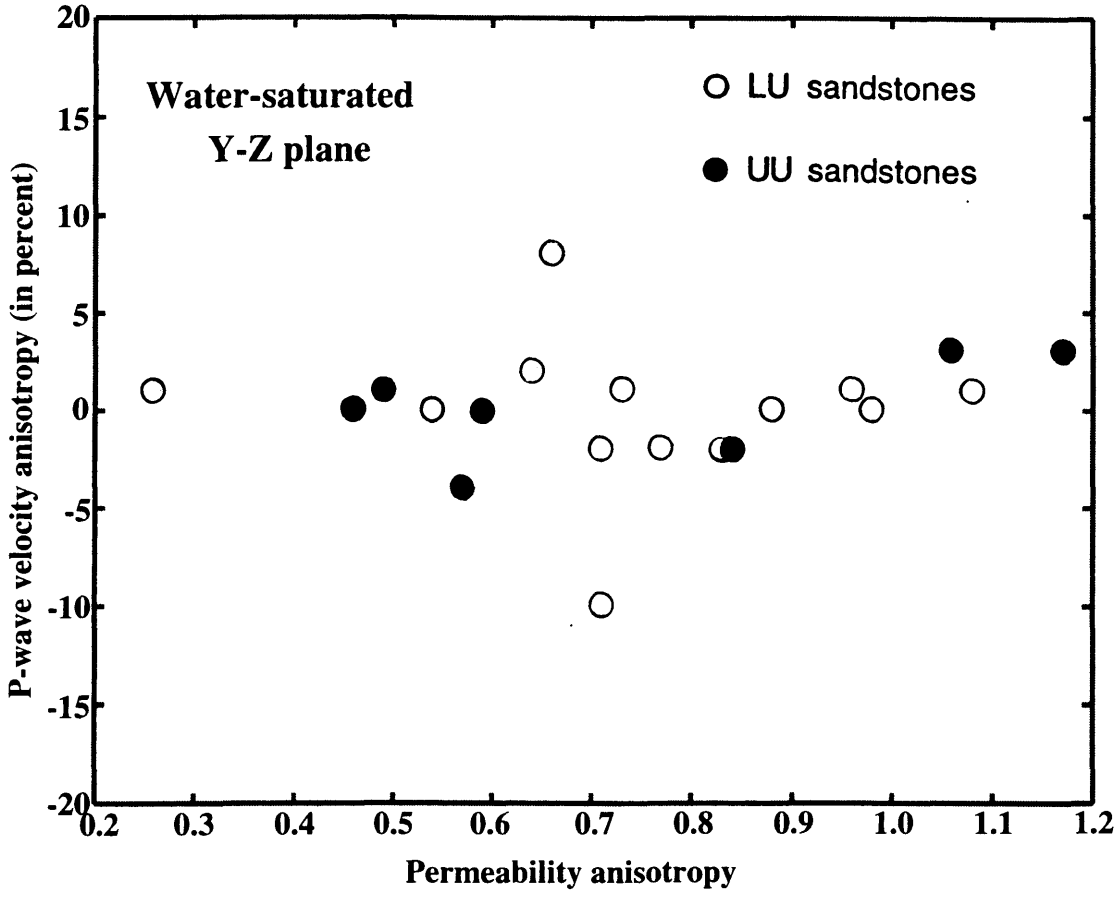

Fig. 4.35 P-wave velocity anisotropy versus permeability anisotropy for sandstone samples from WOSPP. All measurements were made in the Y-Z plane and under water-saturated conditions.

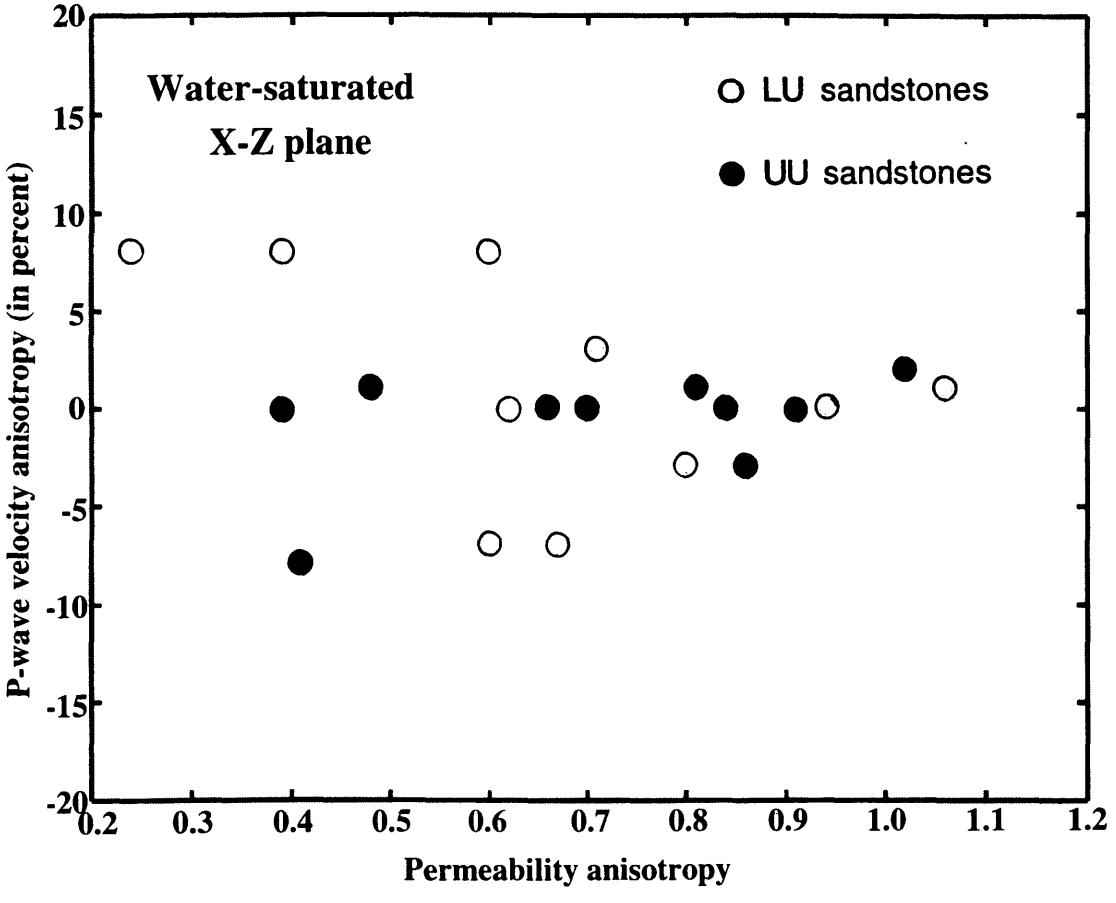

Fig. 4.36 P-wave velocity anisotropy versus permeability anisotropy for sandstone samples from WOSPP. All measurements were made in the X-Z plane and under water-saturated conditions.

4.35 and 4.36 it is evident that P-wave velocity anisotropy is not dependent on permeability anisotropy and keeps a constant value around of 0.0 for the entire permeability anisotropy range.

The scarce phase velocity and attenuation coefficient data for S waves, due to the high attenuation of these kind of waves under water-saturated conditions, made it practically impossible to obtain any significant relationship between S-wave velocity anisotropy and permeability anisotropy.

In conclusion, P-wave attenuation coefficient is more suitable for estimating information about the permeability values and the degree of permeability anisotropy than P-wave phase velocity, under water-saturated conditions.

4.6 Effect of the polarization direction on S-wave phase velocity and attenuation coefficient

Figure 4.37 shows the experimental results about the effect of the S-wave polarization direction on S-wave phase velocities under dry conditions for some sandstone samples from WOSPP. For the S-wave source transducer, two different polarization directions at 0^{o} and 45^{o} with respect to a polarization of reference were considered. The polarization of the S-wave receiver transducer was kept fixed during all the measurements and it was used as the polarization of reference (Figure 4.38). These experimental results show that S-wave phase velocity is no significantly dependent on S-wave polarization direction for these sandstone samples under dry conditions. The S-wave phase velocity differences measured between both polarization directions is less than 12% for some samples, which could be associated with experimental errors (Figure 4.37)

The effect of the S-wave polarization direction on the estimation of the attenuation coefficient under dry conditions is shown in Figure 4.39. Although, the general trend of the S-wave attenuation coefficient is kept for both polarization directions, the differences in the values of this parameter is significant for some sandstone samples, in particular the samples 38, 40, 44, 50 and 54 (Table 1). A common characteristic of these sandstone samples are that they show a 2D/3D cross-beding lithofacies, which indicates the

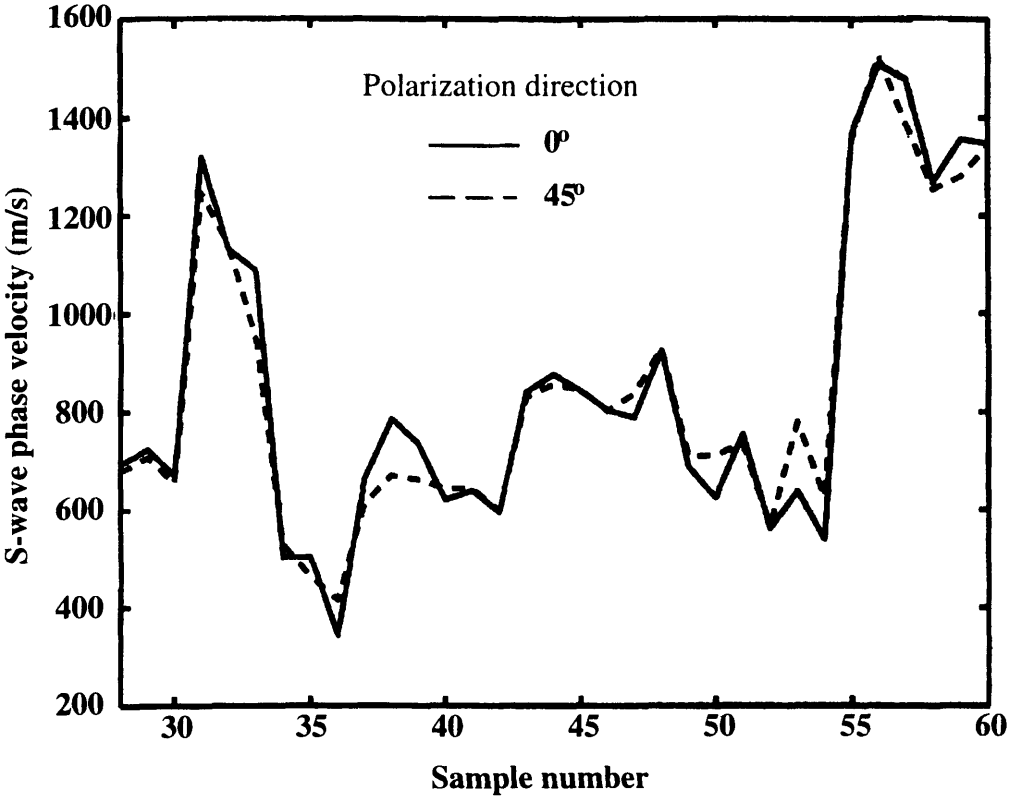

Fig. 4.37 Effect of polarization direction on S-wave phase velocity for sandstone samples from WOSPP under dry conditions. Two polarization directions at 0° and 45° are shown.

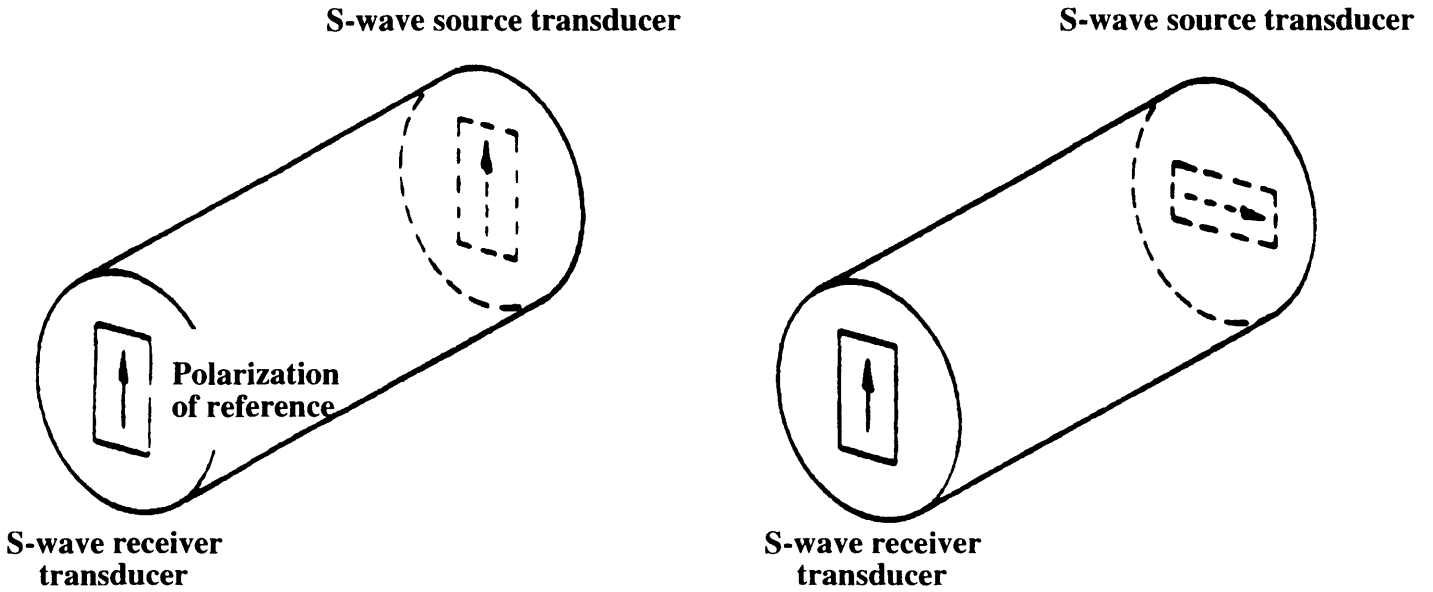

Fig. 4.38 Definition of the polarization of reference in order to study the effect of the S-wave polarization direction on the estimated S-wave phase velocities and S-wave attenuation coefficients under dry conditions at atmospheric confining pressure. The polarization of reference corresponds to the polarization of the S-wave receiver transducer which is kept fixed.

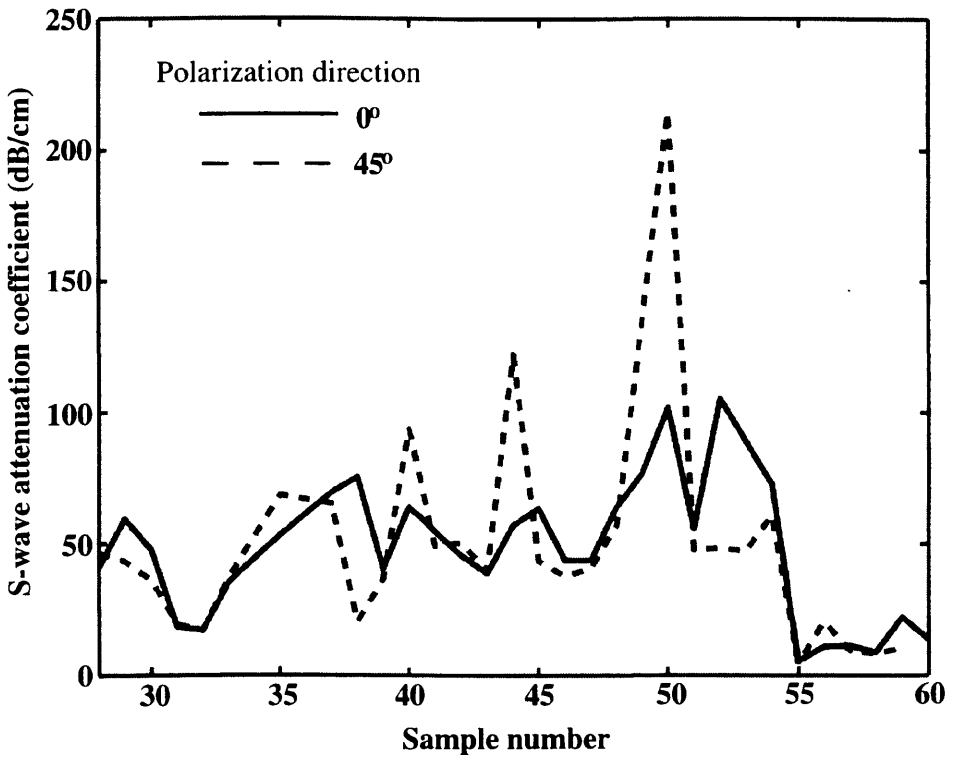

Fig. 4.39 Effect of polarization direction on S-wave attenuation coefficient under dry conditions for sandstone samples from WOSPP. The S-wave source transducer was rotated with respect to the S-wave receiver transducer (fixed), for defining the direction of polarization of the S-wave transmitted through the sandstone sample. The value of the polarization angle was measured by using a protractor placed at the base of the sample (Figure 4.10).

possibility that the observed S-wave attenuation could be affected by other factors different from the anelasticity due to the complex internal structure of these sandstones.

4.7 Pressure effect on P-wave phase velocity and attenuation

For estimating the effect of the effective pressure on the estimated P-wave phase velocities and attenuation coefficients a sandstone sample was analysed under a range of internal pressures between 0 to 2700 psi. This sample was jacketed into a internal pressure device which applies this pressure by a hydraulic pump. A pressure transducer, the pump, and a bleed valve are connected to the acquisition system which communicates to the computer. In this way, internal pressure can be automatically continuously adjusted.

Figure 4.40a shows the effect of the internal pressure on P-wave phase velocity for the sample #14 under water-saturated conditions. It is evident that the P-wave phase velocity increases when the internal pressure is increased. The same conclusion was obtained by Best (1994) and Nur *et al.* (1980) as indicated in Figures 2.19 and 2.24. Best (1994) explained this observation as the result of closing microcracks due to high pressures (section 2.6). In contrast, the P-wave attenuation coefficient is decreased with increasing internal pressure on the sandstone sample (Figure 4.40b). This result is on accordance with the experimental results shown by Winkler and Nur (1979) in Figure 2.25. Although it is necessary to include more P-wave phase velocity and attenuation measurements under pressure, the experimental result obtained from this unique sandstone sample suggests that the above relationships among phase velocity, attenuation and permeability could be valid at higher pressures with an increment in phase velocity and decrement in attenuation coefficient.

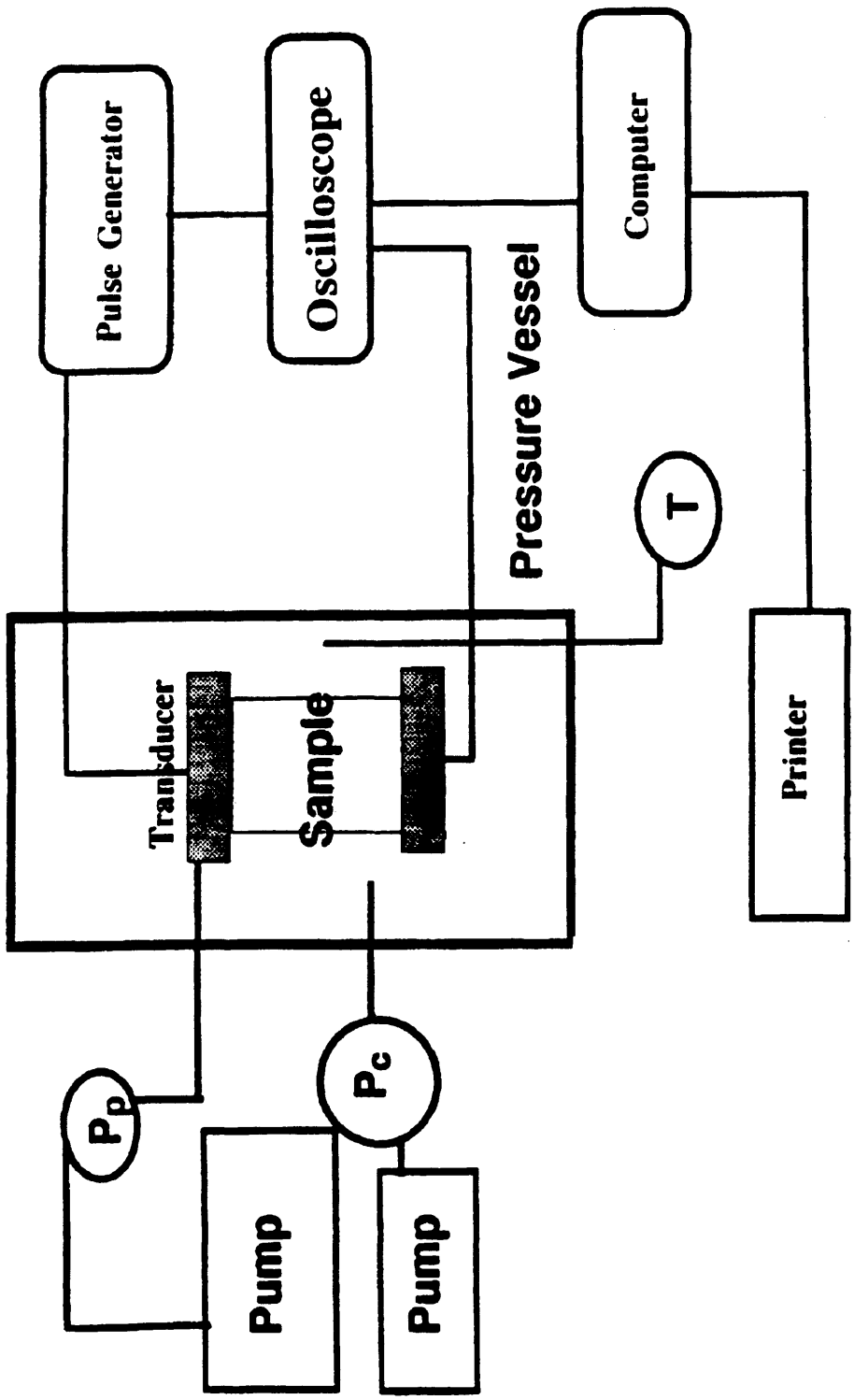

Fig. 4.40 Schematic diagram of apparatus used for P-wave phase and P-wave attenuation measurements under confining pressure conditions.

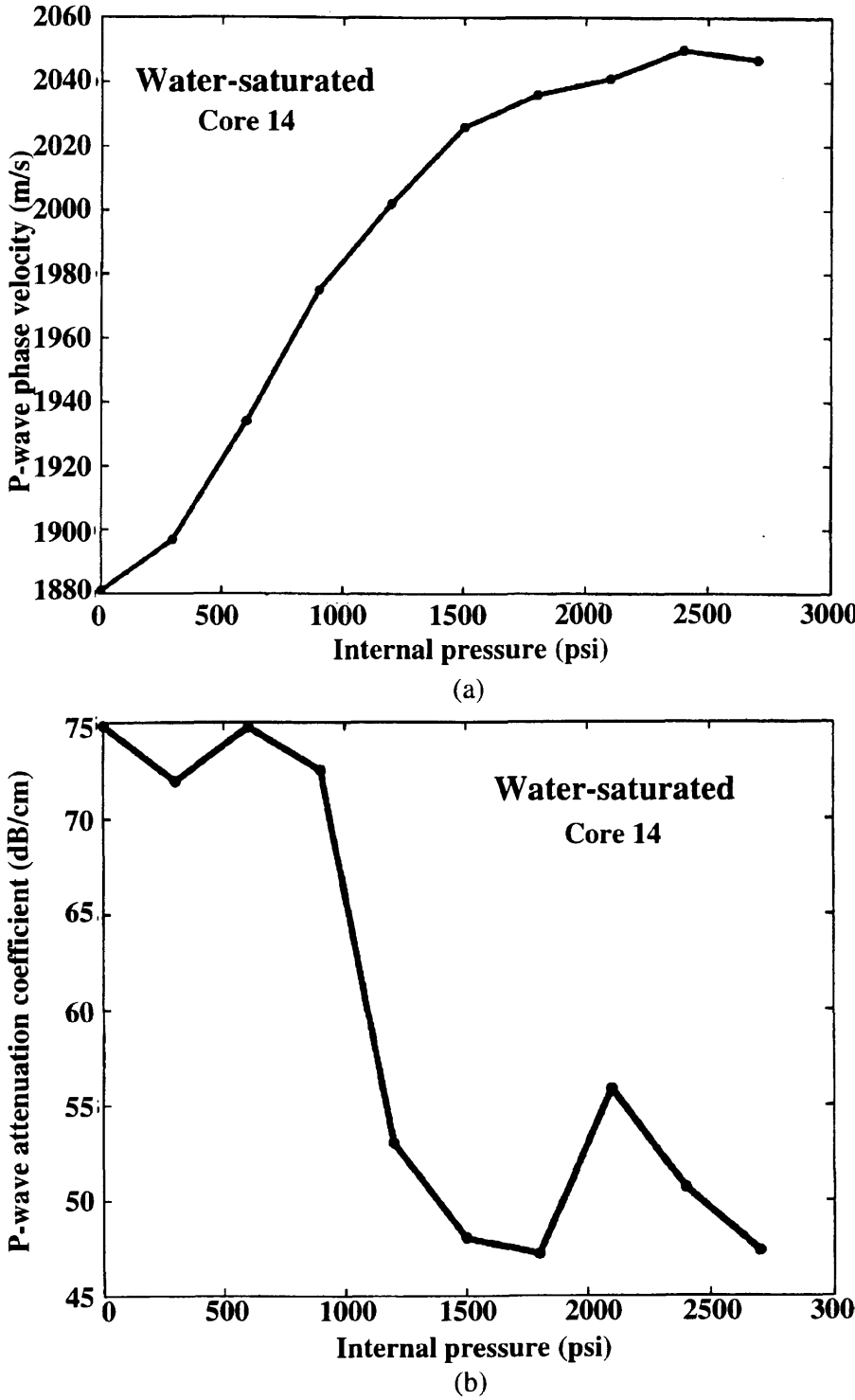

Fig. 4.41 Effect of the internal pressure on: (a) P-wave phase velocity and (b) P-wave attenuation coefficient. All measurements under water-saturated conditions.

CHAPTER 5

Conclusions

Important conclusions are obtained from the analysis of the petrophysical properties of the LU and UU sandstones of the Milk River Formation in Writing-on-Stone Provincial Park (WOSPP):

(i) The measured permeability-porosity relationships for these sandstones indicate that for LU sandstones, this relationship is linear on a semilog plot as expected from statistical analysis of well log information, but for UU sandstones permeability apparently does not show a significant dependence on porosity.

(ii) the porosity-clay content relationship for both LU and UU sandstones shows that porosity increases with clay content resembling the experimental results obtained by Yin and Nur (1994) for unconsolidated synthetic sediments.

(iii) The dependence of permeability on clay content for LU and UU sandstones indicates that no well-defined relation is observed between permeability and clay content, showing two different trends above a clay content value of 10 %. This result is not in accord with the permeability-clay content relationship obtained by Yin and Nur (1994), which shows that permeability logarithmically decreases with increasing clay content. In contrast, the permeability-dolomite content for the same sandstone samples are more closely related to the permeability-clay content behavior found by these authors.

Additionally, very interesting conclusions are obtained from the analysis of the behavior of P- and S-wave phase velocities and attenuation coefficients for the sandstone samples from WOSPP under dry and water-saturated conditions.

(iv) The effect of the saturant fluid (water) on P-wave phase velocity is to diminish the observed velocity anisotropy observed for these samples under dry conditions. This result is in agreement with the reported results from Mavko and Mukerji (1982) showing that velocities and velocity anisotropy may or may not change between dry and saturated conditions depending on the rock, the stress state, and the frequency used in the laboratory.

(v) The analysis of the experimental dependence of P-wave phase velocity with permeability for the sandstone samples from WOSPP, under water-saturated conditions, indicates the presence of two different tendencies: (1) a PDV linear trend where the P-wave velocity decreases with increasing permeability, and (2) a NPDV trend which does not shows correlation between P-wave velocity and permeability. The inclusion of porosity data suggests that the observed behavior of P-wave phase velocity *versus* permeability, for the PDV trend, is more closely associated with a porosity effect as found by other authors.

(vi) A critical permeability is observed in both PDV and NPDV trends, beyond this permeability value P-wave phase velocity not show permeability-dependence. For P-wave phase velocity behavior, indicated by PDV trend, the critical permeability is around of 1500 mD, while for the NPDV trend is around of 300 mD.

(v) Although S-wave phase velocity data is scarce due to the strong attenuation of these kind of waves under water-saturated conditions, S-wave velocity apparently increases monotonically with permeability above the critical permeability (200 mD).

(vi) The measured P-wave attenuation coefficient *versus* permeability along the three orthogonal directions X, Y and Z, for all the sandstone samples from WOSPP under water-saturated conditions, reveals that there is a tendency for P-wave attenuation coefficient to increase when permeability is increased above about 300 mD; a similar conclusion is obtained from the analysis of S-wave attenuation coefficient-permeability relationship, but for S waves the increment in attenuation is higher than is observed in P waves. P- and S-wave velocity-porosity relationships indicate that for both type of waves, the attenuation coefficient increases with porosity at a lower rate than with permeability.

(vii) P-wave attenuation anisotropy is more related to permeability anisotropy than P-wave velocity anisotropy, under water-saturated conditions for the sandstone samples from WOSPP at atmospheric pressure and at a frequency of 1.0 MHz. It was impossible to get any significant conclusion about the behavior of S-wave attenuation anisotropy *versus* permeability anisotropy due to the scarce S-wave data.

(viii) S-wave phase velocity measured under dry conditions does not show a significant dependence on polarization direction for the sandstone samples from WOSPP.

But, S-wave attenuation coefficient apparently is significantly influenced by polarization direction. The reason of this could be associated with the complex internal structure of these sandstones due to the cross-bedding layering. S-wave phase velocity differences between two polarization directions, 45° apart, are less than 12 %.

(ix) As expected the confining pressure affects the P-wave phase velocity increasing its value with increasing pressure, but it produces a decrement in the P-wave attenuation coefficient with increasing pressure.

CHAPTER 6

FUTURE WORK

(i) Extend this study to low frequencies in the laboratory, in order to estimate the frequency-dependence of the P- and S-wave phase velocity-permeability and P- and S-wave attenuation coefficient-permeability relationships.

(ii) Include other different lithologies, *e.g.*, shales and carbonates, in order to determinate the effect of the lithology on observed relationships among velocity, attenuation and permeability.

(iii) Apply the experimental relationships among P and S-wave phase velocities, P and S-wave attenuation coefficients and permeability on seismic data acquired in the field with well control, in order to characterize reservoirs through the estimation of permeability and permeability anisotropy. It implies to evaluate different methods for evaluating P- and S-wave seismic velocities and attenuation coefficients from seismic data, and obtaining accurate permeability data from well log for calibration.

(iv) Perform a geostatistical study on the estimated P- and S-wave velocities and attenuation coefficients as a function of permeability distribution, in order to obtain maps showing the principal permeability trends present in the acquisition area and determinate principal fluid mobility directions or oil-bearing fractures.

APPENDIX A

Finite-size transducer corrections (from Benson and Kiyohara, 1974)

S	ϕ (rad)		$(p/p_0)_{max}$		a (dB)	
	Coef.	Exp.	Coef.	Exp.	Coef.	Exp.
0.10	0.76017	-1	0.93166	0	0.61488	0
0.20	0.11011	0	0.90523	0	0.86482	0
0.30	0.14118	0	0.88529	0	0.10583	1
0.40	0.16049	0	0.87000	0	0.12096	1
0.50	0.18141	0	0.85655	0	0.13450	1
0.60	0.20561	0	0.83552	0	0.15608	1
0.70	0.22505	0	0.83744	0	0.15410	1
0.80	0.25341	0	0.81476	0	0.17794	1
0.90	0.25281	0	0.80236	0	0.19126	1
1.00	0.26593	0	0.80813	0	0.18504	1
1.10	0.29792	0	0.80742	0	0.18580	1
1.20	0.33002	0	0.79334	0	0.20108	1
1.30	0.35059	0	0.77276	0	0.22392	1
1.40	0.35848	0	0.75389	0	0.24539	1
1.50	0.35840	0	0.74134	0	0.25997	1
1.60	0.35635	0	0.73596	0	0.26630	1
1.70	0.35686	0	0.73636	0	0.26582	1
1.80	0.36220	0	0.74038	0	0.26109	1
1.90	0.37286	0	0.74601	0	0.25452	1
2.00	0.38830	0	0.75172	0	0.25451	1
3.00	0.62963	0	0.73275	0	0.24789	1
4.00	0.82826	0	0.64065	0	0.38677	1
5.00	0.96397	0	0.55120	0	0.51738	1
10.00	0.12593	1	0.30400	0	0.10343	2
15.00	0.13621	1	0.20640	0	0.13706	2
20.00	0.14140	1	0.15579	0	0.16149	2
25.00	0.14453	1	0.12500	0	0.18062	2
30.00	0.14662	1	0.10434	0	0.19631	2
35.00	0.14811	1	0.89519	-1	0.20962	2

The column "Exp" indicates the power of 10 by which the "Coef" is to be multiplied.

The phase angle, ϕ and relative amplitude, $\left\langle p/p_0 \right\rangle_{max}$ of the acoustic pressure, averaged over the surface of the receiver are estimated as a function of the dimensionless parameter S ($= z\lambda/a^2$). The attenuation (in decibels) is given by:

$$a = -20\log_{10}\left\langle p/p_0 \right\rangle_{max}$$

APPENDIX B

Glossary (from Sheriff, 1984)

Anisotropy: Variation of a physical property depending on the direction in which it is measured.

Attenuation: A reduction in amplitude or energy caused by the physical characteristics of the transmitting media or system. Usually includes geometric effects such as the decrease in amplitude of a wave with increasing distance from source.

Attenuation factor (or attenuation coefficient): If the amplitude of a plane wave is reduced by the factor $\exp(-\alpha x)$ in traveling a distance of x meters, the attenuation factor is α.

Darcy: A unit of permeability; the permeability which will allow a fluid flow of 1 milliliter per second of 1 centipoise viscosity through 1 square centimeter under a pressure gradient of 1 atmosphere per centimeter. The commonly used unit is the millidarcy expressed as mD (1 darcy = 1,000 mD).

Density: Mass per unit volume. Commonly measured in $g/cm^3 = 10^3 kg/m^3$, often without the units being expressed explicitly.

Grain: **1**. Alignment of features which define a direction. **2**. A small particle.

Isopach: A contour which denotes points of equal thickness of a rock type, formation, group of formations, etc.

Isotropic: Having the same physical properties regardless of the direction in which they are measured.

Microcracks: A theory to explain the effect of pressure on the velocity of nonporous rocks. Minute cracks develop upon cooling because of differences between thermal expansion characteristics among the minerals of which the rock is composed.

Pascal: A unit of pressure, a newton per square meter. Named for Blaise Pascal (1623-1662), French mathematician.

Permeability: A measure of the ease with which a fluid can pass through the pore spaces of a formation. Measured in millidarcy (1/1000 darcy) units.

Porosity: Pore volume per unit gross volume. Often indicated by the symbol ϕ. Porosity is determined from cores, from sonic logs, from density logs, from neutron logs, or from resistivity logs.

Seismic wave: An elastic disturbance which is propagated from point to point through a medium. For P waves, the displacement of the particles of the medium is along the same direction of propagation of this wave; but, for S waves, the particle of the medium are forced to oscillate in a plane forming an angle with respect to the direction of propagation of the wave.

Stiffness: The ratio of stress acting on an elastic medium to the strain, an elastic constant.

Strain: The change of dimensions or shape produced by a stress. Strain is usually expressed in dimensionless units such as change of length per unit of length, angle of twist, change of volume per unit of volume.

Stress: The intensity of force acting on a body, in terms of force per unit ares.

Tortuosity: The length of the path of a fluid passing through a unit length of rock.

Transducer: 1. A device which coverts one form of energy into another. Many types of transducers are reversible; for example, converting electrical energy into acoustical energy and vice versa. Other reversible transducers are electrostatic, variable reluctance, piezoelectric, etc.

Velocity: A vector quantity which indicates time rate of change of displacement. Usually refers to the propagation rate of a seismic wave without implying any direction. Velocity is a property of the medium.

Viscosity: Resistance of a fluid to flow.

APPENDIX C

Abbreviations and symbols

Im = Imaginary part of a complex number.

Re = Real part of a complex number.

R^2 = Correlation factor indicating the goodness of the least-squares fit.

MPa = A unit of pressure (=10^6 pascals, or 10^6 Pa).

*q*P, *q*SV = Nomenclature for denotating P and SV waves propagating through an anisotropic medium, respectively.

psi = Pounds per square inch, a unit of pressure.

Mhz = A unit of frequency (=10^6 Hz).

VSP = Vertical seismic profiling.

$\log(Q^{-1})$ or $\log(1/Q)$ = Logarithmic value of the reciprocal of quality factor, or logarithmic value of the attenuation factor.

$\log f$ = Logarithmic value of the frequency.

$\log k$ = Logarithmic value of the permeability.

δ' = P-wave propagation angle with respect to the z-axis that is directed along the main axis of the pore.

ρ = Bulk density (*i.e.* the total mass of the fluid saturated rock per unit volume), expressed as $\rho = \phi\rho_f + (1-\phi)\rho_s$.

ρ_f = Fluid density.

ρ_s = Solid matrix density.

σ = Stress.

dB/cm = A unit of attenuation per traveled distance.

Q = quality factor. The ratio of 2π times the peak energy to the energy dissipated in a cycle.

APPENDIX D

Data location in SUN

All the ultrasonic seismic data acquired in this M.Sc. thesis is storage under the following directory:

disk/kl34/eric/nicolas/

which is property of the CREWES Physical modelling laboratory at the University of Calgary, Alberta (Canada). This directory includes the following files:

...../NICNEW.PP and **NICNEW.SS:** P- and S-wave data acquired with P-wave source and P-wave receiver transducers (and S-wave source and S-wave receiver transducers) on samples #1 - #27 (Table 1) under dry conditions. Type of pulse: 10.127..

...../NICOWET.PP and **NICOWET.SS:** P- and S-wave data acquired with P-wave source and P-wave receiver transducers (and S-wave source and S-wave receiver transducers) on samples #1 - #42 (Table 1) under water-saturated conditions. Also contains Face-to-Face transducer data. Type of pulse: 10.127.

...../NICMAR2.PPD and **NICMAR2.SSD** Contains P- and S-wave data acquired with P-wave source and P-wave receiver transducers (and S-wave source and S-wave receiver transducers) on samples #28 - #60 (Table 1) under dry conditions. Also contains Face-to-Face transducer data. Type of pulse: 8.127.

...../NICMAR3.PPW and **NICMAR3.SSW** Contains P- and S-wave data acquired with P-wave source and P-wave receiver transducers (and S-wave source and S-wave receiver transducers) on samples #28 - #60 (Table 1) under water-saturated conditions. Also contains S-wave data at 0 and 45 degrees. Type of pulse: 8.127.

...../NIC57A.PPW Contains P-wave data under confining pressure (0-2700 psi).

REFERENCES

Akbar, N., Dvorkin, J. and Nur, A., 1993, Relating *P*-wave attenuation to permeability: *Geophysics*, **58**, 20-29.

Allen, J. R., 1979, Prediction of permeability from logs by multiple regression: *In 6th annual European logging symposium transactions: Society of Professional Well Log Analysis*, 14p.

Anderson, D. L., Minster, B. and Cole, N., 1974, The effect of oriented cracks on seismic velocities: *J. Geophys. Res.*, **79**, 4011-4015.

Ayan, C., Colley, N., Cowan, G., Ezekwe, E., Wannell, M., Goode, P., Halford, F., Joseph, J., Mongini, A., Obondoko, G. and Pop, J., 1994, Measuring Permeability Anisotropy: The Latest Approach: *Oilfield Review*, (October 1994), 24-35.

Beaumont, C., 1981, Foreland basins: *Geophysical Journal of the Royal Astronomical Society*, **55**, 291-329.

Benson, G.C. and Kiyohara, O., 1974, Tabulation of some integral functions describing diffraction effects on the ultrasonic field of a circular piston source: *J. Acoust. Soc. Am.*, **55**, 184-185.

Best, A., 1994, The effect of pressure on seismic velocity and attenuation in reservoir rocks: *56th Meeting and Technical Exhibition*, EAEG (Vienna, Austria), I042.

Best, A. I., McCann, C. and Sothcott, J., 1994, The relationships between the velocities, attenuations and petrophysical properties of reservoir sedimentary rocks: *Geophys. Prosp.*, **42**, 151-178.

Biot, M. A., 1956a, Theory of propagation of elastic waves in a fluid-saturated solid. I, Lower frequency range: *J. Acoust. Soc. Am.*, **28**, 168-178.

——— , 1956b, Theory of propagation of elastic waves in a fluid-saturated solid. II, Higher frequency range: *J. Acoust. Soc. Am.*, **28**, 179-191.

——— , 1962, Mechanics of deformation and acoustic propagation in porous media: *J. Appl. Phys.*, **23**, 1482-1498.

Borcherdt, R. D., 1973, Energy and plane waves in linear viscoelastic media: *J. Geoph. Res.*, **78**, 2442-2453.

Bourbiė, T. and Zinszner, B., 1985, Hydraulic and acoustic properties as a function of porosity in Fontainebleau sandstone: *J. Geoph. Res.*, **90**, 11524-11532.

Bourbiė, T., Coussy, O. and Zinszner, B., 1987, Acoustics of porous media: *Editions Technip*, Paris.

Bowen, C. F., 1915, The stratigraphy of the Montana Group, with special reference to the position and age of the Judith River Formation in north-central Montana: *United States Geological Survey*, Professional Paper 90-1, 1914, 95-153.

Brown, R.J., Lawton, D.C. and Cheadle, S.P., 1991, Scaled physical modelling of anisotropic wave propagation: multioffset profiles over an orthorhombic medium: *Geophysics Journal International*, **107**, 693-702.

Cant, D. J. and Stockmal, G. S., 1989, The Alberta foreland basin: relationship between stratigraphy and Cordilleran terrane-accretion events: *Canadian Journal of Earth Sciences*, **26**, 1964-1975.

Castagna, J. P., Batzle, M. L. and Eastwood, R. L., 1985, Relationships between compressional-wave and shear-wave velocities in clastic silicate rocks: *Geophysics*, **50**, 571-581.

Cerveny, V. and Frangie, A.B., 1982, Effects of causal absorption on seismic body waves: *Studia Geoph. et Geol.*, **26**, 238-253.

Cheadle, S.P., Brown, R.J. and Lawton, D.C., 1991, Orthorhombic anisotropy: A physical seismic modelling study: *Geophysics*, **56**, 1603-1613.

Cheel, R. J. and Leckie, D. A., 1990, A tidal-inlet complex in the Cretaceous epeiric sea of North America: Virgelle Member, Milk River Formation, southern Alberta, Canada: *Sedimentology*, **37**, 67-81.

Claerbout, J. F., 1976, Fundamentals of Geophysical Data Processing: McGraw-Hill International Series in Planetary Sciences, McGraw-Hill Book Co.

Crampin, S., 1978, Seismic-wave propagation through a cracked solid: Polarization as a possible dilatancy diagnostic: *Geophys. J. R. Astr. Soc.*, **53**, 467-496.

———, 1981, A review of wave motion in anisotropic and cracked elastic-media: *Wave Motion*, **3**, 343-391.

———, 1984a, Anisotropy in exploration geophysics: *FIRST BREAK*, **2**, No. 3, 19-21.

———, 1984b, An introduction to wave propagation in anisotropic media: *Geophys. J. R. Astr. Soc.*, **76**, 17-28

Crampin, S., Chesnokov, E. M. and Hipkin, R. A., 1984, Seismic anisotropy—the state of the art: *Geophys. J. R. Astr. Soc.*, **76**, 1-16.

Dellinger, J., 1991, Anisotropic seismic wave propagation: *Ph.D. thesis*, Stanford University.

Diederix, K.M., 1982, Anomalous relationships between resistivity index and water saturations in the Rotliegend Sandstone (The Netherlands), paper X *in* 23rd annual logging symposium transactions: *Society of Professional Well Log Analysis*, 16p.

Dowling, D. B., 1916, Water-supply, southeastern Alberta: *Geological Survey of Canada, Summary Report* 26, 1915, 102-110.

Dullien, F. A. L., 1979, Porous media: Fluid Transport and Pore Structure, 369pp, *Academic*, San Diego, Calif.

Ehlig-Economides, C., Ebbs, D., Fetkovich, M. and Meehan, D. N., 1990, Factoring Anisotropy into Well Design: *Oilfield Review 2*, No. 4 (October 1990), 24-33.

Eisbacher, G. H., Carrigy, M. A. and Campbell, R. B., 1974, Paleodrainage patterns and late orogenic basins of the Canadian Cordillera. *In* Dickinson, W. R. (Ed.): *Tectonics and sedimentation.* Society of Economic Paleontologists and Mineralogists, Special Publication 22, 143-166.

Elsey, R.K., Tittman, B.R., Nadler, H.R. and Ahlberg, L.A., 1977, Defect characterization by ultrasonic signal process techniques: *Proceedings of Ultrasonic Symposium*, IEEE, 48-52.

Energy Resources Conservation Board, 1992, Ultimate Potential and Supply of natural gas in Alberta: *Energy Resources Conservation Board*, Report 92-A.

Geerstma, J. and Smit, D. C., 1961, Some aspects of elastic wave propagation in fluid-saturated porous solids: *Geophys.*, **26**, 169-181.

Gelinsky, S. and Shapiro, S. A., 1994a, Poroelastic velocity and attenuation in media with anisotropic permeability: *64th Ann. Internat. Mtg., Soc. Expl. Geophys.*, Expanded Abstracts, 818-821.

——— , 1994b, *SH*-wave velocity and attenuation in poroelastic transverse isotropic media: *56th Meeting and Technical Exhibition,* EAEG (Vienna, Austria), P114.

——— , 1995, Anisotropic permeability: influence on seismic velocity and attenuation: *accepted for publication in*: *Proceedings of the 6IWSA,* (Trondheim, Norway).

Gibson, R. L. Jr. and Toksöz, M. N., 1990, Permeability estimation from velocity anisotropy in fracture rocks: *J. Geophys. Res.*, **95**, 15643-15655.

Greenkorn, R. A., Johnson, C. R. and Shallenberger, L. K., 1964, *Soc. Pet. Eng. J.*, **4**, 124.

Han, D., Nur, A. and Morgan, F. D., 1986, Effects of porosity and clay content on wave velocities in sandstones: *Geophysics*, **51**, 2093-2107.

Han, D., 1987, Effect of porosity and clay content on acoustic properties of sandstones and unconsolidated sediments: *Ph.D. thesis*, Stanford University.

Jannsen, D., Voss, J. and Theilen, F., 1985, Comparison of methods to determine Q in shallow marine sediments from vertical reflection seismograms: *Geophys. Prosp.*, **33**, 479-497.

Johnston, D. H. and Toksöz, M. N., 1980, Ultrasonic *P* and *S* wave attenuation in dry and saturated rocks under pressure: *J. Geoph. Res.*, **85**, 925-936.

Jones, T., 1983, Wave propagation in porous rocks and models for crystal structure: *Ph.D. thesis*, Standford University.

Kjartansson, E., 1979, Constant *Q*-wave propagation and attenuation: *J. Geophys. Res.*, **84**, 4737-4748.

Klimentos, T., 1991, The effects of porosity-permeability-clay content on the velocity of compressional waves: *Geophysics*, **56**, No. 12, 1930-1939.

Klimentos, T. and McCann, C., 1990, Relationships between compressional wave attenuation, porosity, clay content, and permeability of sandstone: *Geophysics*, **55**, 998-1014.

Knopoff, L., 1969, Q: *Review Geophysics 2*, **4**, 625-660.

Krebes, E.S. and Hron, F., 1980, Ray-synthetic seismograms for SH waves in anelastic media: *Bull. Seis. Soc. Am.*, **70**, 29-46.

Leckie, D. and Rosenthal, L., 1986, Cretaceous depositional facies in the western interior: the southern Alberta transect. Guide Book: *Canadian Society of Petroleum Geologists Summer Field Trip*, August, 1986, 70p.

Liu, H. P., Anderson, D. L. and Kanamori, H., 1976, Velocity dispersion due to anelasticity; Implications for seismology and mantle composition: *Geophys. J. Roy. Astron. Soc.*, **47**, 41-58.

Lomnitz, C., 1956, Creep measurements in igneous rocks: *J. Geol.*, **64**, 473-479.

——— , 1957, Linear dissipation in solids: *J. Appl. Phys.*, **28**, 201-205.

Mavko, G. and Mukerji, T., 1992, Pore fluid effects on seismic velocity anisotropy: 62*th Annual International Meeting and Exhibition*, SEG Expanded Abstracts (New Orleans-USA).

McCann, C., 1994, Estimating the permeability of reservoir rocks form *P*-wave velocity and quality factor: 56*th Meeting and Technical Exhibition*, EAEG (Vienna-Austria), P172.

Meijer-Drees, N. C. and Mhyr, D. W., 1981, The Upper Cretaceous Milk River and Lea Park Formations in southeastern Alberta: *Bull. Can. Petroleum Geology*, **29**, No. 1, 42-74.

Meyboorn, P., 1960, Geology and groundwater resources of the Milk River sandstone in southern Alberta: *Research Council of Alberta Memoir* 2, 89p.

Meyer, R., 1994, Shoreface to Coastal-Plain Estuarine Deposition in the Milk River Formation, southern Alberta, Canada. Guide Book: *Canadian Society of Petroleum Geologists Fall Field Trip*, September, 1994, 51p.

Mhyr, D. W. and Meijer-Drees, N. C., 1976, Geology of the southeastern Alberta Milk River Gas Pool, *In*: *The sedimentology of selected clastic oil and gas reservoirs in Alberta. Canadian Society of Petroleum Geologists*, Calgary, Alberta.

Monger, J. W. H. and Price, R. A., 1979, The geodynamic evolution of the Canadian Cordillera - progress and problems: *Canadian Journal of Earth Sciences*, **16**, 770-791.

Murphy, W. F., III, 1982, Effects of partial water saturation on attenuation in sandstones: *J. Acoust. Soc. Am.*, **71**, 1458-1468.

Murphy, W. M., 1983, Effects of partial water saturation on attenuation in Massillon sandstone and Vycor porous glass: *J. Acoust. Soc. Am.*, **71**, 1458-1468.

Musgrave, M.J.P., 1970, Crystal Acoustics: Holden-Day.

Nelson, R. A., 1985, Geologic Analysis of Naturally Fractured Reservoirs: *Contributions in Petroleum Geology & Engineering*, Gulf Publishing Company, Houston, Texas, 320p.

Nur, A. and Byerlee, J. N., 1971, An exact effective stress law for elastic deformation of rocks with fluid: *J. Geoph. Res.*, **76**, 6414-6418.

Nur, A., Walls, J. D., Winkler, K. and De Vilbiss, J., 1980, Effects of fluid saturation on waves in porous rock and relations to hydraulic permeability: *SPE journal*, 450-458.

Nye, J.F., (1957,1985), Physical Properties of Crystals: Oxford University Press.

Papadakis, E.P., 1966, Ultrasonic diffraction loss and phase change in anisotropic materials: *J. Acoust. Soc. Am.*, **40**, 863-876.

Postma, G.W., 1955, Wave propagation in a stratified medium: *Geophysics*, **20**, 780-806.

Price, R. A., 1973, Large-scale gravitational flow of supracrustal rocks, southern Canadian Rocky Mountains. *In* De Jong, K. A. and Scholten, R. A. (Eds.): *Gravity and Tectonics*, Wiley Interscience, New York, 491-502.

Rathore, J. S., Fjaer, E., Renlie, L. and Nysaeter, J., 1993, Estimation of phase velocities in cracked rocks: *55th EAEG meeting*, Stavanger, Norway, Expanded Abstracts, 124.

Rathore, J. S., Fjaer, E., Holt, R. M. and Renlie, L., 1994, *P*- and *S*-wave anisotropy of a synthetic sandstone with controlled crack geometry: *Geophys. Prosp.*, **43**, 711-728.

Rice, D. D., 1980, Coastal and deltaic sedimentation of Upper Cretaceous Eagle sandstone: relation to shallow gas accumulations, north-central Montana: *American Association of Petroleum Geologists Bulletin*, **64**, No. 3, 316-338.

Ristic, V.M., 1987, Principles of Acoustic Devices: *A Wiley-Interscience Publication*, John Wiley & Sons.

Scheidegger, A. E., 1954, *Geofis. Pura Appl.*, **28**, 75.

Sears, E.M. and Bonner, B.P., 1981, Ultrasonic attenuation measurement by spectral ratio utilizing signal processing techniques: IEEE *Transactions on Geoscience and Remote Sensing GE-19*, **2**, 95-99.

Seki, H., Granato, A. and Truell, R., 1956, Diffraction effects in the ultrasonic field of a piston source and their importance in the accurate measurement of attenuation: *J. Acoust. Soc. Am.*, **28**, 230-238.

Sheriff, R. E., 1984, Encyclopedic Dictionary of Exploration Geophysics: Society of Exploration Geophysicists (SEG), Seccond Edition.

Spencer, J. W., 1981, Stress, relaxations at low frequencies in fluid-saturated rocks: Attenuation and modulus dispersion: *J. Geophys. Res.*, **86**, 1803-1812.

Stainsby, S.D. and Worthington, M.H., 1985, Q estimation from vertical seismic profile data and anomalous variation in the North Sea: *Geophysics*, **50**, 615-626.

Sun, Z., 1994, Seismic Anisotropy in Salt from Theoretical Study, Modelling, and Field Experiments: *M.Sc. thesis*, The University of Calgary.

Taner, M.T. and Sheriff, R.E., 1977, Application of Amplitude, Frequency and Other Attributes to Stratigraphic and Hydrocarbon Determination: published *in Seismic Stratigraphy-applications to hydrocarbon exploration*, The American Association of Petroleum Geologists, Tulsa, Oklahoma, U.S.A., 301-327.

Taner, M.T., Koehler, F. and Sheriff, R.E. 1979, Complex trace analysis: *Geophys.*, **44**, 1041-1063.

Tang, X., Toksöz, M. N., Tarif, P. and Wilkens, R. H., 1994, A method of Measuring Acoustic Wave Attenuation in the Laboratory: *64th Annual International Meeting and Exhibition*, SEG Expanded Abstracts (New Orleans-USA), 668-669.

Tarif, P., 1986, Mesure de l'atte'nuation par propagation d'ultrasons: application `a l'e'tude de l'anisotropie: *Thesis*, Universite' Paris VII.

Tatham, R. H. and McCormack, M. D., 1993, Multicomponent Seismology in Petroleum Exploration, *Society of Exploration Geophysicist*, 248p.

Thomsen, L., 1986, Weak elastic anisotropy: *Geophysics*, **51**, 1954-1966.

Tittmann, B. R., Bulua, J. R. and Addel-Gawad, M., 1983, Dissipation of elastic waves in fluid saturated rocks: *Am. Inst. Phys. conference on physics and chemistry of porous media*, Schlumberger-Doll Research, Johnson, D. L. and Sen, P. N. (Eds.): *Am. Inst. Phys.*, 131-143.

Toksöz, M. N., Johnston, D. H. and Timur, A., 1979, Attenuation of seismic waves in dry and saturated rocks: I. Laboratory measurements: *Geophysics*, **44**, 681-690.

Tonn, R., 1991, The determination of the seismic quality factor Q from VSP data: A comparison of different computational methods: *Geophys. Prosp.*, **39**, 1-27.

Tosaya, C., 1982, Acoustical properties of clay-bearing rocks: *Ph.D. thesis*, Stanford University.

Tovell, W. M., 1956, Some aspects of the geology of the Milk River and Pakowki Formations (southern Alberta): *Ph.D. thesis*, University of Toronto, 129p.

Vestum, R.W., 1994, Group- and Phase-Velocity Inversions for the General Anisotropic Stiffness Tensor: *M.Sc. thesis*, The University of Calgary.

Ward, R.W. and Toksöz, M.N., 1971, Causes of regional variation of magnitude: *Bull. Seism. Soc. Am.*, **61**, 649-670.

Wendt, W. A., Sakurai, S. and Nelson, P. H., 1986, Permeability prediction from well logs using multiple regression. *In* Lake, L. W. and Carroll, H. B., Jr., (Eds.): *Reservoir Characterization: Academic Press, Inc.*, 181-222.

Williams, G. D. and Stelck, C. R., 1975, Speculations on the Cretaceous palaeogeography of North America. *In* Caldwell, W.G.E. (Ed.): *The Cretaceous System in the western interior of North America*: *The Geological Association of Canada*, Paper No. 13, 1-20.

Winkler, K. W. and Nur, A., 1979, Pore fluids and seismic attenuation in rocks: *Geoph. Res. Lett.*, **6**, 1-4.

Winkler, K. W. and Nur, A., 1982, Seismic attenuation: Effects of pore fluids and frictional sliding: *Geophysics*, **47**, 1-15.

Winkler, K. and Plona, T. J., 1982, Techniques for measuring ultrasonic velocity and attenuation spectra in rocks under pressure: *J. Geophys. Res.*, **87**, 10776-10780.

Yin, H. and Nur, A., 1993, Porosity, Permeability, and Acoustic Velocity in Granular Materials: *63th Annual International Meeting and Exposition*, SEG Expanded Abstracts (Washington-USA), SL3.6, 775-778.